Coulomb Crystal Studies, Sympathetic Cooling, and Mass Spectrometry Using Laser-Cooled Be^+ Ions

Inaugural-Dissertation

zur Erlangung des Doktorgrades
der Mathematisch-Naturwissenschaftlichen Fakultät
der Heinrich-Heine-Universität Düsseldorf

vorgelegt von

Ulf Fröhlich

aus München

Düsseldorf, April 2008

Aus dem Institut für Experimentalphysik
der Heinrich-Heine-Universität Düsseldorf

Gedruckt mit der Genehmigung der
Mathematisch-Naturwissenschaftlichen Fakultät der
Heinrich-Heine-Universität Düsseldorf

Referent: Prof. S. Schiller, Ph.D.
Koreferent: Prof. Dr. A. Görlitz

Tag der mündlichen Prüfung: 24.06.2008

Contents

Chapter 1

Introduction

1.1 Overview of the Project

The work described in this thesis is part of a project which may be entitled as *High-Precision Laser Spectroscopy of Ultracold Molecular Hydrogen Ions*. Starting in the year 1999 at the University of Konstanz [1–4] and now being conducted in the group of Prof. S. Schiller at the University of Düsseldorf, progress achieved so far may be divided into three stages.

I. In a first stage, described in Refs. [1–4], conceptual work was done on the trapping and cooling of molecular hydrogen ions, leading to the choice of a linear rf (Paul) trap together with sympathetic cooling, using laser-cooled $^9Be^+$ ions. A two-photon, ro-vibrational transition in the electronic ground state of the HD^+ molecular ion was selected, suitable for high precision laser spectroscopy. Furthermore, a detection scheme was worked out, employing selective photodissociation of the HD^+ molecular ions in the excited state. In addition to conceptual work, an ultra-high vacuum (UHV) chamber for the linear rf trap was set up together with a first version of the 313 nm cooling laser system, required for Doppler laser cooling of the $^9Be^+$ ions.

II. In a second stage, described in this thesis as well as Refs. [4–8], the experimental setup was completed and first results were obtained. In particular, laser cooling and crystallization of $^9Be^+$ ions was demonstrated, the $^9Be^+$ ion crystals being characterized with respect to their crystal structure, outer shape, and temperature. Furthermore, sympathetic cooling of $^{14}N^+$, BeD^+, BeH^+, $^4He^+$, HD^+, and D^+ ions was demonstrated with both the sympathetically cooled (SC) and the laser-cooled (LC) ions in a cloud-like state. Accordingly, sympathetic cooling down to a mass ratio of $m_{SC}/m_{LC} = 0.22$ was shown to be possible as was later confirmed for the crystalline state [9]. Finally, sympathetic crystallization of $^4He^+$ ions was demonstrated by preparing two-species $^9Be^+$-$^4He^+$ ion crystals of different size, each with a core of crystallized non-fluorescent $^4He^+$ ions.

III. Subsequent experimental work performed in the group of Prof. S. Schiller up to the present time is described in Refs. [9–15], a short summary of which is found at the end of this thesis. In particular, sympathetic crystallization of H_2^+ , HD^+ , and D_2^+ as well as many other atomic and molecular ion species was demonstrated, culminating in the first laser spectroscopic measurements of ro-vibrational transitions in *ultracold* HD^+ ions, embedded into a $^9Be^+$ ion crystal.

1.2 High-Precision Laser Spectroscopy of Ultracold HD^+ Ions and Related Topics

In the following, various topics will be described, all related in some respect to the ultimate goal of high-precision laser spectroscopy of ultracold HD^+ molecular ions.

Laser Spectroscopy of the Molecular Hydrogen Ion

Among numerous motivations [1,2,6,14,16] for high-precision laser spectroscopy of the molecular hydrogen ion, i.e. H_2^+ and its isotopomers HD^+ and D_2^+, a measurement of the fundamental mass ratios m_e/m_p and m_p/m_d is regarded as the main motivation for the project described in Sect. 1.1. So far, the most accurate values of m_e/m_p and m_p/m_d are specified with relative uncertainties of $4.6 \cdot 10^{-10}$ [17,18] and $2.0 \cdot 10^{-10}$ [17], respectively, obtained by Penning trap mass spectrometry and electron spin resonance of hydrogen-like ions in a Penning trap. Alternatively, a measurement of m_e/m_p and m_p/m_d by laser spectroscopy of ro-vibrational transitions in HD^+ should be feasible as well. This is due to the dependencies of the vibrational and rotational level energies on the mass ratio m_e/μ, which in a first approximation are given by $E_{\mathrm{vib}} \sim R_\infty (m_e/\mu)^{1/2}$ and $E_{\mathrm{rot}} \sim R_\infty (m_e/\mu)$ [14]. Here, $\mu = m_p\, m_d/(m_p + m_d)$ is the reduced mass of the two nuclei. Expectations with regards to accuracy, surpassing those achieved by Penning trap mass spectrometry, are based on two facts: (i) by taking appropriate measures against line-shifting and broadening effects such as collision, Doppler, and transit time broadening, a spectroscopic resolution at the level of the relative linewidth due to spontaneous decay $\delta\nu/\nu \leq 10^{-13}$ should be possible. In particular, spatial confinement of the HD^+ molecular ions, cooling to the milli-Kelvin range and/or use of two-photon spectroscopy [1,19] will be required. (ii) the molecular hydrogen ions H_2^+, HD^+, and D_2^+ are the simplest molecules of all, each representing a fundamental three-body system. Accordingly, high-precision *ab initio* molecular calculations of the ro-vibrational level energies and transition rates are possible [16,20–22]. Thus, by comparing the measured ro-vibrational transition frequencies in HD^+ with the corresponding molecular calculations, determination of the fundamental mass ratios m_e/m_p and m_p/m_d should be possible with an accuracy similar to those of the ex-

perimental and theoretical data. Up to the present time, laser spectroscopy of the ro-vibrational transition in HD^+ usually was performed on molecular ion beams, yielding relative accuracies of $\delta\nu/\nu \leq 10^{-6}$ [23,24] which is far from the accuracy aimed at. On the other hand, nonrelativistic calculations of the ro-vibrational level energies in HD^+ for orbital momenta $L \leq 4$ and vibrational quantum numbers $\nu \leq 4$ have been performed with a precision of approximately 10 Hz [16]. Together with calculations of the leading order relativistic [20] and radiative corrections [21] as well as a complete *ab initio* calculation of the contribution due to hyperfine energy [22], a final precision of approximately 50 kHz was obtained. Thus, regarding theory, sufficient accuracy has been reached to allow for a determination of the electron-to-proton mass ratio m_e/m_p with a relative uncertainty of $1{\cdot}10^{-9}$ [22] once experimental data with a similar accuracy is available. Finally, a test of the time-invariance of m_e/m_p at a level of 10^{-15}/yr [16] should be feasible as an ultimate goal, if increasing both the experimental and theoretical accuracies up to their respective limits.

Sympathetic Cooling

Cooling of the HD^+ molecular ions using laser-cooled $^9Be^+$ ions, i.e. indirect cooling of one ion species by Coulomb interaction with another, directly laser-cooled ion species, usually is referred to as sympathetic cooling. In the ultimate case of sympathetic cooling where temperatures of a few milli-Kelvin are reached, sympathetic crystallization of the sympathetically cooled ions takes place and a multi-species ion crystal forms. Historically, a first experiment on sympathetic cooling was performed in a Penning trap between different types of Mg^+ isotopes, including laser spectroscopy of the sympathetically cooled species in order to determine isotope shifts [25]. In rf (Paul) traps, sympathetic cooling was observed with the first experiments on ion Coulomb crystals (see below), where the appearance of dark, non-fluorescent spots in the crystals was recognized as sympathetic cooling of additionally trapped impurity ions. In more recent experiments using linear rf traps, sympathetic cooling was applied to various ion species in different applications, two of which shall be mentioned here: (i) sympathetic cooling of a single $^{24}Mg^+$ ion by a single $^9Be^+$ ion and vice versa was demonstrated in Ref. [26] for the purpose of quantum information processing. In particular, cooling of the axial oscillation modes of a two-ion $^9Be^+$-$^{24}Mg^+$ crystal down to the ground state was shown to be possible, choosing $^9Be^+$ as the coolant ion. (ii) sympathetic cooling of large molecules was demonstrated in Refs. [27,28]. In particular, singly protonated organic molecules ($m = 410$ u) [27] and singly charged fullerene ions ($m = 720$ u) [28] were sympathetically cooled, using laser-cooled $^{138}Ba^+$ and $^{24}Mg^+$ ions, respectively. Finally, it should be noted that a minimum mass ratio of $m_{\mathrm{SC}}/m_{\mathrm{LC}} = 8/15 \approx 0.53$ was predicted in Ref. [29] as a lower limit for sympathetic cooling, where m_{SC} and m_{LC} denote the masses of the sympathetically cooled (SC) and laser-cooled (LC) ions, respectively. In this theoretical work, both the sympathetically and laser-cooled ions were assumed to be in a cloud-like state and confined in a linear rf trap. Thus, if valid as a general limit, sympathetic cooling of the HD^+ molecular ions using laser-cooled $^9Be^+$ ions would be impossible since $m_{\mathrm{Be}}/m_{\mathrm{HD}} = 0.3$.

Single-Species Ion Crystals

Single-species $^{9}Be^{+}$ ion crystals are not only a prerequisite for the sympathetic crystallization of HD^{+} molecular ions, but also represent physical systems of significant interest by their own, usually referred to as Coulomb crystals. Besides from their possible occurrence in the interior of brown and white dwarfs [30], ion Coulomb crystals are prepared routinely in the laboratory by laser cooling of, e.g., $^{9}Be^{+}$, $^{24}Mg^{+}$, $^{40}Ca^{+}$, or $^{138}Ba^{+}$ ions in rf (Paul) as well as Penning traps. Typical ion densities in trapped ion crystals are $10^{7}-10^{9}\,\mathrm{cm}^{-3}$, depending on the particular strength of the confining potential, thus decreased by more than ten orders of magnitude with respect to those in the conventional solid state. As a consequence, very low temperatures of a few milli-Kelvin have to be reached in order to achieve crystallization of the trapped ion cloud. Due to their finite size, trapped ion Coulomb crystals generally exhibit a lattice structure which strongly depends on the total number of ions as well as the particular confining forces. As an example, ion crystals in an infinitely long, cylindrically symmetric 2-D harmonic confining potential, approximately realized by a highly prolate linear rf trap or a quadrupole rf storage ring, are expected to arrange as (in order of increasing ion number): 1-D strings, zigzag-structures, helices, and multishell structures [31]. Ion Coulomb crystals for the first time were observed in hyperbolic rf (Paul) traps [32,33], followed by quadrupole rf storage rings [34,35] and Penning traps [36,37]. Numerous applications have been demonstrated up to the present time, among which frequency standards [38] and memories for quantum computing [39] shall be mentioned here. Implementation of a quantum computer by a string of trapped ions has been suggested in Refs. [40,41]. Detailed studies of the formation process as well as the shell structure of large $^{24}Mg^{+}$ ion crystals in a linear rf trap is found in Refs. [42], including comparisons with molecular dynamics (MD) simulations.

Multi-Species Ion Crystals

In the ultimate case of sympathetic cooling down to temperatures in the milli-Kelvin range, sympathetic crystallization occurs. Thus, a multi-species ion crystals forms, consisting of the laser-cooled as well as sympathetically cooled ions. While an exact theoretical description of the spatial arrangement of the different ion species is only possible using molecular dynamics (MD) simulations, a few general rules can be stated here: in rf (Paul) as well as Penning traps, a *radial separation* of the different ion species is expected to occur due to the decrease in strength of the confining potential with increasing ion mass. In particular, ions with a mass-to-charge ratio lower than that of the laser-cooled ions are expected to arrange on the trap axis, while ions with a mass-to-charge ratio higher than that of the laser-cooled ions are expected to arrange at the outer crystal regions. Radial separation was confirmed experimentally in both rf (Paul) [43] as well as Penning traps [44]. Furthermore, with the cooling laser beam directed along the trap axis, a partial *axial separation* is observed [45–47] between the sympathetically and the laser-cooled ions. This is caused by radiation pressure which solely acts on the laser-cooled species. In order to determine the (translational) temperature of the sympathetically cooled ions,

optical spectroscopy may be employed in case of atomic [25] as well as molecular ions [12]. However, in general this is limited by the accessibility of optical transitions in the sympathetically cooled ion species. Sympathetic crystallization of HD^+ as well as large molecular ions ($m = 20\,000\,\mathrm{u}, Q = 20\,\mathrm{e}$) in a linear rf trap using laser-cooled $^9Be^+$ and $^{138}Ba^+$ ions, respectively, was studied theoretically in Ref. [48]. This was done by use of molecular dynamics (MD) simulations which included the full time-dependence of the rf trapping fields in order to accurately account for rf heating. A temperature almost equal to that of the laser-cooled ions was reached by the sympathetically cooled ions. Accordingly, sympathetic crystallization was predicted to be possible down to a mass ratio of $m_{\mathrm{SC}}/m_{\mathrm{LC}} = 0.3$ as was later confirmed experimentally [9]. Finally, two possible applications of multi-species ion crystals shall be noted here, the second of which was pursued in this work: (i) the use of (small) two-species ion strings for quantum computing as suggested in Ref. [49], and (ii) the use of (large) two-species ion crystals as a source of ultracold atomic (e.g., $^4He^+$) or molecular (e.g., HD^+) ions.

Laser-Cooled Fluorescence Mass Spectrometry (LCF-MS)

Identification of non-fluorescent ions, sympathetically cooled by the laser-cooled ions, may be achieved using a technique for which the term *laser-cooled fluorescence mass spectrometry* (LCF-MS) was introduced in Ref. [50]. LCF-MS is based on the resonant excitation of secular ion motion in the time-averaged trap potential of a rf (Paul) trap, which for the first time was demonstrated in Ref. [51] in order to selectively remove ions from a hyperbolic rf trap. By scanning the frequency of an electric excitation field superimposed to the trapping field, while monitoring the fluorescence of the laser-cooled ions, a mass spectrum is obtained: resonant excitation of a particular sympathetically cooled ion species with a given mass-to-charge ratio m/Q causes a temporary sympathetic heating of the laser-cooled ions which in turn is reflected by a corresponding change in fluorescence signal. Thus, LCF-MS is non-destructive and easy to implement as compared to time-of-flight [52] as well as other techniques [53]. Usually, both the sympathetically and the laser-cooled ions are prepared in a cloud-like state in order to reduce Coulomb interactions between the ions. Accordingly, simple mass spectra are obtained since resonant excitation approximately occurs at the respective single particle frequencies $\omega_r \sim Q/m$. In general, a characteristic asymmetric shape is observed for the dips in the fluorescence signal constituting the mass spectrum. This could be explained by a simplified model, formulated in Ref. [54], which is based on the time-averaged trap potential description and accounts for laser cooling, sympathetic cooling, rf heating, and space charge. Recently, LCF-MS was studied in detail for the case of ion plasmas in a crystalline state [13]. In particular, LCF-MS was performed on multi-species ion crystal containing different species of sympathetically cooled as well as the laser-cooled ions. Large frequency shifts with respect to the single particle frequencies $\omega_r \sim Q/m$ as well as peak coalescence were observed. This could be explained by the strong mutual Coulomb interactions between the ions of different species.

1.3 Structure of the Present Thesis

Chapter 2: A brief introduction will be provided to the theoretical concepts and terminology as required for the interpretation of experimental results in chapters 5–7. In particular, the time-averaged potential description of the linear rf trap, the thermal equilibrium states of a confined single-species plasma, and a simplified model of laser-cooled fluorescence mass spectrometry (LCF-MS) will be reviewed.

Chapters 3 and **4:** These two chapters cover the experimental setup. In chapter 3, the ultra-high vacuum (UHV) and fluorescence detection setup will be described, including new components such as a new linear rf trap, a new trap supply electronics, and the detection optics. In chapter 4, the cooling laser system will be described. In particular, the final setup for doubly resonant sum-frequency generation (DR-SFG) of 313 nm laser light will be characterized with respect to output power, tunability, and spectral purity. Furthermore, a brief description will be given of an absolute frequency stabilization and a frequency shifter which both were added to the DR-SFG setup.

Chapter 5: Mass spectra obtained by laser-cooled fluorescence mass spectrometry (LCF-MS) will be presented, where LCF-MS was performed on plasmas in a cloud-like state. Various sympathetically cooled ion species could be identified. However, the focus in this chapter will be on the interpretation of the obtained fluorescence signal shape.

Chapter 6: Single-species $^9Be^+$ ion crystals will be investigated in detail. As a starting point, a general description will be given of the continuous transition to the crystalline state, characteristic of confined plasmas of finite size. Temperature estimates will be given, obtained from fits of Voigt profiles to the measured fluorescence signal of the $^9Be^+$ ions. Finally, a detailed study of ellipsoidal shaped $^9Be^+$ ion crystals in a fully anisotropic time-averaged trap potential will be presented.

Chapter 7: Sympathetic crystallization of atomic $^4He^+$ ions will be demonstrated. In particular, different sized two-species $^9Be^+$-$^4He^+$ ion crystals will be presented which may serve as a source of ultracold $^4He^+$ ions, suitable for high-precision laser spectroscopy.

Chapter 8: A summary will be given of the experimental results achieved in this work. This chapter also includes a short outlook on subsequent experimental results, achieved in the group of Prof. S. Schiller and leading to the first laser spectroscopic measurements of ro-vibrational transitions in ultracold HD^+.

Chapter 2

Theoretical Introduction

In this chapter, the terminology and theoretical concepts will be provided as far as relevant to the interpretation of the experimental results presented in chapters 5–7. As a starting point, a brief review will be given in **Sect. 2.1** of the time-averaged trap potential of the linear rf trap. After that, different aspects of the thermal equilibrium state of a confined single-species plasma will be considered in **Sect. 2.2**. In particular, a brief introduction will be given in **Sect. 2.2.1** to the single species plasma, including theoretical concepts such as the Debye length and the plasma coupling parameter. Furthermore, a charged fluid description will be used in **Sect. 2.2.2** to predict the outer shape of a single species plasma in the crystalline state. A theoretical description of the continuous transition to the crystalline state, characteristic of confined single-species plasmas of finite size, will be deferred to chapter 6. Finally, a simplified model of laser-cooled fluorescence mass spectrometry (LCF-MS) will be reviewed in **Sect. 2.3**.

2.1 Time-Averaged Trap Potential

The transverse dimensions of the linear rf trap are determined by the radius r' of the electrode rods and the minimum distance r_0 from the trap axis to the electrode surfaces as indicated in Fig. 2.1. The motion of a trapped particle is preferably described in Cartesian coordinates, where the orientation of the coordinate axes is chosen as shown in Fig. 2.1. Throughout this work, the z-axis shall be referred to as the trap axis.

At first, the case of a pure rf voltage $U_{\mathrm{RF}} \sin(\Omega\, t)$ shall be considered, applied to the electrode rods as shown in Fig. 2.1. The resulting electric potential in the region of the trap axis is a time-varying quadrupole potential plus additional higher order terms, since the round shape of the electrode cross sections deviates from the ideal

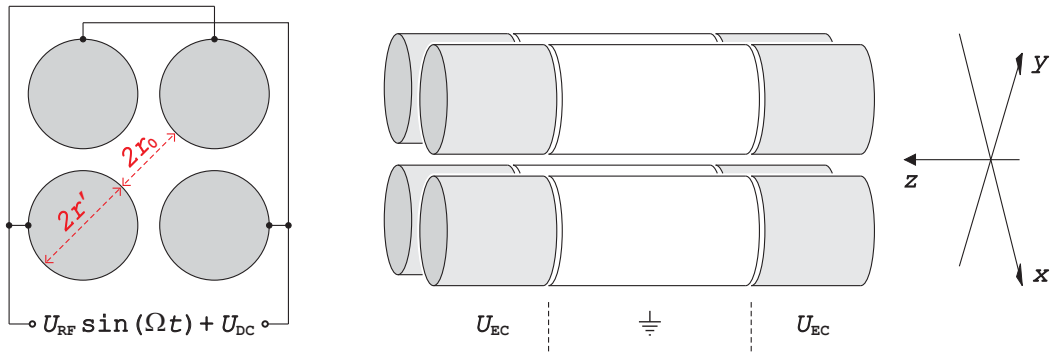

Figure 2.1: *Overview of the rf and static voltages applied to the linear trap.* ***Left:*** *cross section of the linear trap. The rf voltage* $U_{RF}\sin(\Omega t)$ *and the static voltage* U_{DC} *are applied to the electrode rods in a quadrupolar configuration.* ***Right:*** *side view of the linear trap. Each electrode rod is divided into three electrically isolated segments, the center electrode and the two endcap electrodes. In addition to the voltage* $U_{RF}\sin(\Omega t)+U_{DC}$ *applied throughout the whole length of the linear trap, a static voltage* U_{EC} *is applied to the eight endcap electrodes, while the four center electrodes are held at ground potential.*

hyperbolic shape. However, close to the trap axis the contribution of the higher order terms can be neglected. This is true in particular if the optimum value of 1.1468 [55] is chosen for the ratio r'/r_0. In the xy-plane, i.e. transverse to the trap axis, the equation of motion of a particle with charge Q and mass m thus can be solved analytically [56] in terms of the so-called Mathieu functions [57]. Stable solutions, i.e. solutions with an amplitude that stays finite, are determined by the criterion $q<0.908$, where

$$q \stackrel{\text{def}}{=} \frac{2\,Q\,U_{\mathrm{RF}}}{m\,r_0^2\,\Omega^2} \tag{2.1}$$

is the so-called Mathieu stability parameter. Furthermore, if $q \ll 1$, the transverse motion of a trapped particle can be adequately described by the motion in a time-averaged harmonic potential [58], superimposed by an additional jitter motion at the radio frequency Ω. For the linear trap geometry shown in Fig. 2.1, the time-averaged (electric) potential is given by

$$\phi_{\mathrm{trap}} = \frac{m\,\omega_0^2}{2\,Q}\left(x^2+y^2\right), \quad \text{where} \tag{2.2a}$$

$$\omega_0 = \frac{Q\,U_{\mathrm{RF}}}{\sqrt{2}\,m\,\Omega\,r_0^2}\,. \tag{2.2b}$$

Accordingly, ω_0 is the frequency of the trapped particle motion transverse to the trap axis. From the condition $q \ll 1$ together with Eqs. (2.1) and (2.2b), the relation

$\omega_0 = (q/\sqrt{8})\,\Omega \ll \Omega$ can be derived which states that the motion in the time-averaged potential, the so-called *secular motion*, is of much lower frequency than the jitter motion at the radio frequency Ω, the so-called *micromotion*.

Confinement along the trap axis is achieved by applying a static voltage U_{EC} to the endcap electrodes as indicated in Fig. 2.1. A numerical solution of the resulting electrostatic potential on the trap axis will be shown in Sect. 3.2. Furthermore, a static voltage U_{DC} can be added to the rf voltage $U_{\mathrm{RF}} \sin(\Omega\, t)$, thus augmenting the time-varying quadrupole potential by a static component. The corresponding time-averaged (electric) trap potential, including the effect of the additional static voltages U_{EC} and U_{DC}, is given by

$$\phi_{\mathrm{trap}} = \frac{m}{2\,Q}\left(\omega_x^2\, x^2 + \omega_y^2\, y^2 + \omega_z^2\, z^2\right), \quad \text{where} \tag{2.3a}$$

$$\omega_x = \sqrt{\omega_0^2 + \frac{Q\,U_{\mathrm{DC}}}{m\,r_0^2} - \frac{1}{2}\,\omega_z^2} \tag{2.3b}$$

$$\omega_y = \sqrt{\omega_0^2 - \frac{Q\,U_{\mathrm{DC}}}{m\,r_0^2} - \frac{1}{2}\,\omega_z^2} \tag{2.3c}$$

$$\omega_z = \sqrt{\frac{2\,\kappa\,Q\,U_{\mathrm{EC}}}{m}}\ . \tag{2.3d}$$

Accordingly, ω_x and ω_y are the transverse trap frequencies of the particle motion in x and y-direction, respectively, while ω_z is the axial trap frequency of the particle motion along the trap axis. The frequency ω_0 which appears in Eqs. (2.3b) and (2.3c) is given by Eq. (2.2b), whereas κ in Eq. (2.3d) is a constant determined by the trap geometry. Appearance of the term $-\omega_z^2/2$ in Eqs. (2.3b) and (2.3c) reflects the fact that the static electric field caused by the endcap voltage U_{EC} also has components in the x and y-direction. Finally, it should be noted that Eqs. (2.3a–d) apply to particles of both polarities, positive and negative, if choosing the endcap voltage U_{EC} appropriately. However, in the remainder of this chapter, a positive charge $Q>0$ and thus a positive endcap voltage $U_{\mathrm{EC}}>0$ shall be assumed.

If no static voltage U_{DC} is applied, the transverse trap frequencies ω_x and ω_y, given by Eqs. (2.3b) and (2.3c), are degenerate and the time-averaged trap potential (2.3a) possesses cylindrical symmetry. By applying a static voltage $U_{\mathrm{DC}} > 0$, the cylindrical symmetry is broken and the transverse trap frequency ω_x increases while ω_y decreases. Finally, for a sufficiently large voltage U_{DC}, the transverse trap frequency ω_y vanishes, implying that the motion in y-direction becomes unstable. The same is true for $U_{\mathrm{DC}}<0$, where in this case the motion in x-direction becomes unstable. Application of a static voltage U_{DC} may be used to remove high-mass impurity ions from the trap as well as to produce ellipsoidal shaped plasmas as will be demonstrated in Sect. 6.3.

2.2 Thermal Equilibrium States of the Confined Single-Species Plasma

In this section, a general introduction will be given to the single species plasma and the one-component plasma (OCP) model. Furthermore, a charged fluid description will be used to predict the outer shape and average number density of a crystalline single species plasma, confined in the time-averaged trap potential (2.3). In both the OCP model as well as the charged fluid description, thermal equilibrium is assumed. Thus, when comparing the predictions of the charged fluid description with the outer shape of the $^9Be^+$ ion crystals in chapter 6, it should be noted that strictly speaking the latter are not in a thermal equilibrium state. Rather, the $^9Be^+$ ion crystals are in a stationary state which is governed by the balance between laser cooling and rf heating (→ Sect. 6.2).

2.2.1 Single-Species Plasmas and the OCP Model

The $^9Be^+$ ion crystals presented in chapter 6 as well as the $^9Be^+$ ions in the cloud-like state which precedes the crystalline state, are, apart from a few additionally trapped impurity ions, examples of confined *single-species plasmas* [59,60]. Whereas "normal" plasmas are defined as (partially) ionized gases which are macroscopically neutral, single-species plasmas are completely unneutralized and in that respect they are the limiting case of a more general class of plasmas referred to as *nonneutral plasmas* [61]. However, despite the fundamental difference between neutral and nonneutral plasmas, many of the collective phenomena which are characteristic of neutral plasmas are also observed for confined nonneutral plasmas. This justifies the designation of the latter as *plasmas*. In particular, a test charge introduced into a neutral plasma at temperature T, consisting in equal shares of particles with charges $\pm Q$, is effectively shielded at distances larger than the Debye length

$$\lambda_D \stackrel{\text{def}}{=} \sqrt{\frac{\epsilon_0\, k_B\, T}{n\, Q^2}}\ , \tag{2.4}$$

where n is the number density of all particles regardless of their sign of charge [62]. Similarly, Eq. (2.4) applies to the case of a confined single-species plasma, consisting solely of particles with charge Q, where any externally imposed electrostatic field is shielded out from the plasma interior within a distance in the order of the Debye length (2.4) [61]. In this case, n denotes the number density of the single-species plasma, i.e. the number density of the particles with charge Q. Thus, a criterion for the designation of a system of confined charged particles as a *plasma* can be derived, according to which the system has to be large in all its dimensions compared to the Debye length (2.4) [59,60].

A standard theoretical model to study correlations in neutral plasmas is the *one-component plasma* (OCP) which consists of a system of identical, classical charged particles embedded in a uniform neutralizing background charge of opposite sign and number density n_0 [63–66]. The OCP is of great astrophysical importance since it provides an excellent model for describing many aspects of superdense, completely ionized matter, typical of the interior of brown (Jupiter: $T = 2\text{–}3 \cdot 10^4\,\mathrm{K}$, $n = 3.5 \cdot 10^{24}\,\mathrm{cm}^{-3}$) and white dwarfs ($T$ up to $2 \cdot 10^7\,\mathrm{K}$, n up to $10^{34}\,\mathrm{cm}^{-3}$) [30]. As was first shown in Ref. [63], the nature of the thermal equilibrium state of an *infinite* OCP at temperature T is solely determined by a single dimensionless parameter, the so-called plasma coupling parameter

$$\Gamma \stackrel{\text{def}}{=} \frac{Q^2}{4\pi\epsilon_0 a_{\mathrm{WS}} k_B T} \quad . \tag{2.5}$$

Here, Q is the charge of the particles embedded in the uniform neutralizing background charge. The Wigner-Seitz radius a_{WS} is a measure of the interparticle spacing and is defined by $(4/3)\pi a_{\mathrm{WS}}^3 = n_0^{-1}$. Accordingly, the plasma coupling parameter (2.5) is the ratio of the average Coulomb interaction energy between neighboring particles to the average thermal energy $k_B T$. For an infinite OCP, the formation of a liquid phase and a liquid-solid phase transition are predicted to occur at

- $\Gamma > 2$ [64], where the system begins to exhibit local order characteristic of a fluid, and
- $\Gamma \approx 170$ [65,66], where a phase transition to a crystal state with a bcc lattice structure takes place.

A general review on strongly correlated ($\Gamma \gg 1$) OCPs is given by Ichimaru in Ref. [67].

Laboratory realizations of *finite* OCPs are provided by single-species plasmas confined in Penning as well as rf (Paul) traps, where in each case a *3-D harmonic* trap potential [a] acts as the uniform neutralizing background charge. In particular, the number density n_0 can be derived from the 3-D harmonic trap potential using Poisson's equation $n_0 = (Q/\epsilon_0)\Delta\phi_{\mathrm{trap}}$. Furthermore, as will be shown in Sect. 2.2.2, the number density n_0 becomes equal to the number density of the confined charges in the low temperature limit where the Debye length (2.4) is negligibly small compared to all plasma dimensions. Accordingly, the plasma coupling parameter Γ as defined by Eq. (2.5) also applies to a confined single-species plasmas. In general, confined plasmas with a plasma coupling parameter $\Gamma \ll 1$ are referred to as weakly correlated plasmas, whereas confined plasmas with a plasma coupling parameter $\Gamma \gg 1$ are referred to as strongly correlated plasmas. Comparisons of strongly

[a] Penning trap: effective trap potential in the rest frame of the rotating plasma. Rf (Paul) trap: time-averaged trap potential (→ Sect. 2.1).

correlated single-species plasmas, confined in Penning and rf (Paul) traps, with the predictions of the OCP model are found in Ref. [68] (Penning trap) and Ref. [69] (linear rf trap).

Finally, it should be noted that the ion crystals presented in chapter 7, consisting of laser-cooled $^9Be^+$ ions as well as sympathetically cooled $^4He^+$ ions, are examples of confined *plasmas with a single sign of charge*. This is a further subset of the nonneutral plasma.

2.2.2 The Charged Fluid Model

A weakly correlated ($\Gamma \ll 1$) single-species plasma consisting of N ions with charge Q and mass m, confined in a given trap geometry and in thermal equilibrium at temperature T, may be described as a macroscopic charged fluid with number density $n_f(\boldsymbol{r})$ [61]. In their review article, Dubin and O'Neil [60] (see also Ref. [70]) derive a set of equations which determines the thermal equilibrium state of such a charged fluid by the requirement of *force balance*, i.e. no net force on any fluid region. For a few simple trap geometries, numerical solutions are presented in Ref. [71] which all have in common a number density $n_f(\boldsymbol{r})$ which is nearly constant within the fluid and then drops to zero at the outer fluid boundary on the scale of the Debye length λ_D [Eq. (2.4)] [a]. This characteristic behavior was confirmed by measurements of the density profiles of pure electron [72] as well as buffer-gas-cooled Mg^+ ion plasmas [73], confined in Penning-like traps. A simplification of the equations derived in Refs. [60,70] is shown to be possible in the limit where the Debye length λ_D becomes negligibly small compared to all plasma dimensions. In this limit, the requirement of force balance is already fulfilled if at any point within the fluid the repulsive forces due to space charge are compensated by the external confining forces. For a crystalline single-species plasma, like the $^9Be^+$ ion crystals in chapter 6, the Debye length λ_D is even smaller than the interparticle spacing ($\rightarrow$ Sect. 6.2). Thus, the condition of a negligibly small Debye length compared to all plasma dimensions is fulfilled. However, crystalline plasmas are strongly correlated plasmas ($\Gamma \gg 1$) for which the charged fluid model becomes inadequate. In the framework of a N-particle description (canonical ensemble) of the thermal equilibrium state of a confined, strongly correlated single-species plasma, it can be shown that correlations merely establish order within the plasma rather than causing any appreciable change of the outer plasma shape or the average number density [60]. Therefore, the predictions of the charged fluid model remain valid even for a crystalline plasma, as long as the above characteristics are concerned. In

[a] Since in the cited references, the focus is on Penning traps where radial confinement is provided by an uniform magnetic field along the trap axis, a further characteristic of the presented solutions is the rigid rotation of the whole fluid around the trap axis. However, by replacing the corresponding effective trap potential in the rotating frame by the time-averaged potential of the rf (Paul) trap, the theoretical treatment can be easily adapted to the latter type of traps.

the following, the charged fluid model shall be used to determine the outer shape and average number density of a crystalline single-species plasma, confined in the time-averaged trap potential (2.3).

If the confining forces can be expressed in terms of a trap potential [b], the requirement that the repulsive forces due to space charge have to be compensated by the external confining forces can be stated in the form $\phi_{\mathrm{trap}}(\boldsymbol{r})+\phi_f(\boldsymbol{r})=const$ $\forall\, \boldsymbol{r}\in V_f$. Here, ϕ_f and V_f designate the space charge potential and the volume of the charged fluid, respectively. Since ϕ_f is related to the number density n_f by Poisson's equation $\Delta\phi_f(\boldsymbol{r}) = -(Q/\epsilon_0)\, n_f(\boldsymbol{r})$, application of the Laplace operator Δ to both sides of the equation $\phi_{\mathrm{trap}}(\boldsymbol{r})+\phi_f(\boldsymbol{r}) = const$ directly yields the number density $n_f(\boldsymbol{r}) = (\epsilon_0/Q)\Delta\phi_{\mathrm{trap}}(\boldsymbol{r})$ within the charged fluid. Accordingly, a trap potential with a harmonic dependence on the spatial coordinates x, y, and z yields a number density which is constant within the charged fluid. In particular, if ϕ_{trap} is given by the time-averaged trap potential (2.3) of the linear rf trap, the number density within the charged fluid is given by

$$n_0 \;=\; \frac{\epsilon_0\, U_{\mathrm{RF}}^2}{m\,\Omega^2\, r_0^4}\;, \tag{2.6}$$

where Eq. (2.2b) was used. It should be noted that n_0 neither depends on the static voltages U_{DC} and U_{EC} ($\rightarrow$ Sect. 2.1) nor on the charge Q of the ions constituting the plasma.

In order to determine the outer shape of the charged fluid, confined in the time-averaged trap potential (2.3), it suffices to note that the electrostatic potential of a tri-axial ellipsoid of constant charge density ρ_0 has a harmonic dependence on the spatial coordinates x, y, and z within the ellipsoid [74]. In particular, with the additional boundary condition of vanishing at infinity, the potential ϕ_f within the ellipsoid is given by

$$\phi_f(\boldsymbol{r}) \;=\; \frac{\rho_0}{4\,\epsilon_0}\left[A_x(R_x^2-x^2)+A_y(R_y^2-y^2)+A_z(L^2-z^2)\right]\;, \tag{2.7}$$

where R_x, R_y, and L are the principal axes of the ellipsoid in x, y, and z-direction, respectively. Eq. (2.7) matches onto an exterior solution which vanishes at infinity. The dimensionless coefficients A_x, A_y, and A_z can be expressed as functions of the principal axes ratios R_x/L and R_y/L as will be shown in appendix A. Thus, the requirement $\phi_{\mathrm{trap}}(\boldsymbol{r})+\phi_f(\boldsymbol{r})=const\ \forall\ \boldsymbol{r}\in V_f$ can be fulfilled for any given trap potential with a harmonic dependence on the spatial coordinates x, y, and z, by arrangement of the charged fluid into a tri-axial ellipsoid of appropriate shape and charge

[b] Throughout this work, the term *trap potential* designates an electric potential in the sense that the force acting on a particle with charge Q is given by $\boldsymbol{F} = -Q\nabla\phi_{\mathrm{trap}}(\boldsymbol{r})$. Of course, trap potentials like the time-averaged trap potential (2.3) are not electrostatic potentials in a true sense since they do not obey Laplace's equation $\Delta\phi(\boldsymbol{r}) = 0$.

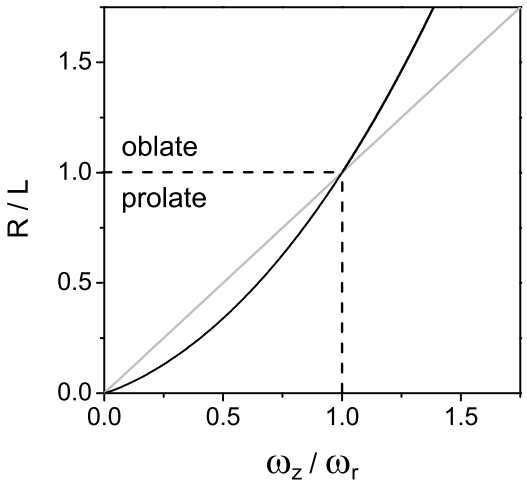

Figure 2.2: *Solution of Eqs.* (2.8a) *and* (2.8b) *for the special case* $\omega_x = \omega_y$ *in which the outer shape of the charged fluid is a spheroid with radius* R *and half-length* L*. The aspect ratio* R/L *is plotted as a function of the trap frequency ratio* ω_z/ω_r*, where* $\omega_r \stackrel{\text{def}}{=} \omega_x = \omega_y$*. For comparison, a grey line shows the aspect ratio* $R/L = \omega_z/\omega_r$ *as expected in case of noninteracting particles. Dashed lines mark the transition of the outer shape of the charged fluid from a prolate* ($R<L$) *to an oblate* ($R>L$) *spheroid.*

density. In particular, if ϕ_{trap} is given by the time-averaged trap potential (2.3), the requirement is fulfilled by $\rho_0 = Q n_0$ and $A_i = 2\epsilon_0 m \omega_i^2 / n_0 Q^2$ ($i = x, y, z$), where n_0 is given by Eq. (2.6) and ω_x, ω_y, and ω_z are the trap frequencies (2.3b–d). The principal axes ratios R_x/L and R_y/L can thus be calculated for a given set of trap frequencies (2.3b–d) by simultaneously solving the two equations

$$\left(\frac{\omega_x}{\omega_z}\right)^2 = \frac{A_x(R_x/L,\, R_y/L)}{A_z(R_x/L,\, R_y/L)} \tag{2.8a}$$

$$\left(\frac{\omega_y}{\omega_z}\right)^2 = \frac{A_y(R_x/L,\, R_y/L)}{A_z(R_x/L,\, R_y/L)} \quad . \tag{2.8b}$$

Fig. 2.2 shows a solution of Eqs. (2.8a) and (2.8b) for the special case of degenerate transverse trap frequencies $\omega_x = \omega_y$ ($\rightarrow$ Sect. 2.1) in which the trap potential possesses cylindrical symmetry around the trap axis. The resulting spatial distribution of the charged fluid is a spheroid (ellipse of revolution) of constant charge density $\rho_0 = Q n_0$ with radius R and half-length L. Accordingly, Eqs. (2.8a) and (2.8b) reduce to a single equation which relates the aspect ratio $R/L = R_x/L = R_y/L$ to the corresponding trap frequency ratio ω_r/ω_z, where $\omega_r \stackrel{\text{def}}{=} \omega_x = \omega_y$. With increasing value of ω_z/ω_r, the outer shape of the charged fluid changes from a prolate spheroid ($R<L$) to an oblate spheroid ($R>L$), where for the special case $\omega_z/\omega_r = 1$ the outer shape is a sphere with radius $R=L$. For comparison, Fig. 2.2 also shows the aspect ratio $R/L = \omega_z/\omega_r$ as expected in case of noninteracting particles ($\rightarrow$ Sect. 6.1).

Thus, the outer shape of the charged fluid is modified due to the collective interaction by space charge in so far as the prolate-oblate deformation becomes more pronounced.

Hornekær et al. [42, 75] have found good agreement between the predictions of the charged fluid model shown in Fig. 2.2 and the measured aspect ratios R/L of a large variety of spheroidal shaped $^{40}Ca^{+}$ ion crystals. In chapter 6, the measured aspect ratios $R_{45}/L \stackrel{\text{def}}{=} [(R_x^2+R_y^2)/2\,]^{1/2}/L$ of different-sized ellipsoidal shaped $^{9}Be^{+}$ ion crystals will be compared with a solution of Eqs. (2.8a) and (2.8b) for the most general case of non-degenerate transverse trap frequencies $\omega_x \neq \omega_y$.

2.3 Laser-Cooled Fluorescence Mass Spectrometry (LCF-MS)

In this section, a simplified model of laser-cooled fluorescence mass spectrometry (LCF-MS) will be reviewed which was formulated by Baba and Waki in Ref. [54]. The model is intended to describe LCF-MS, performed on ions in a cloud-like state and confined in a linear rf trap. Furthermore, the cooling laser frequency is assumed to be only slightly red-detuned with respect to the cooling transition frequency. Accordingly, a temporary heating of the laser-cooled ions will cause a dip in the fluorescence signal as will be further discussed in Sect. 5.1. This corresponds to the experimental conditions of the measurements presented in Refs. [50, 76, 77] as well as those in chapter 5 of this work. The simplified model is based on the time-averaged trap potential approximation (→ Sect. 2.1) and accounts for laser cooling, sympathetic cooling/heating, rf heating, and space charge. In particular, a simple analytical expression is used for the space charge potential of the laser-cooled ions which will first be derived in Sect. 2.3.1, before turning to the model itself in Sect. 2.3.2.

2.3.1 Effective Trap Potential

In the simplified model of LCF-MS, the sympathetically cooled ions are assumed to move in the superposition of the time-averaged trap potential (→ Sect. 2.1) and the space charge potential of the laser-cooled ions. Since the model is intended to describe LCF-MS performed on ions in a cloud-like state, a more or less Gaussian spatial distribution is expected for the laser-cooled ions (→ Sect. 6.1). However, in order to reduce the mathematical complexity of the model, the spatial distribution of laser-cooled ions is approximated by a constant density spheroid which was first formulated by Dehmelt [58]. Thus, no spatial dependence has to be considered, e.g., for the ion-ion collision rates within the cloud of laser-cooled ions. In this section, Dehmelt's approximation will be briefly reviewed. Furthermore, a simple analytical

expression will be derived for the *effective* trap potential, i.e. the superposition of the time-averaged trap potential and the space charge potential of the laser-cooled ions.

The cloud of laser-cooled ions which shall be approximated by a constant density spheroid, is assumed to consist of $N_{\rm LC}$ ions with charge $Q_{\rm LC}$ and mass $m_{\rm LC}$, confined in the time-averaged trap potential $\phi_{\rm trap}(\boldsymbol{r}) = m_{\rm LC}(\omega_{r({\rm LC})}^2 r^2 + \omega_{z({\rm LC})}^2 z^2)/2Q_{\rm LC}$. In the high-temperature limit where the Debye length (2.4) is large compared to the plasma dimensions, interactions between the ions can be neglected (→ Sect. 6.1). In this limit, the ions are assumed to occupy the entire volume determined by $\boldsymbol{r} \in V \Leftrightarrow \phi_{\rm trap}(\boldsymbol{r}) \leq 3k_B T_{\rm LC}/Q_{\rm LC}$, where $3k_B T_{\rm LC}$ is the total thermal energy per ion. Accordingly, the spatial distribution of laser-cooled ions in the high-temperature limit is approximated by a constant density spheroid with radius $R = (6k_B T_{\rm LC}/m_{\rm LC})^{1/2}\omega_{r({\rm LC})}^{-1}$, half-length $L = (6k_B T_{\rm LC}/m_{\rm LC})^{1/2}\omega_{z({\rm LC})}^{-1}$, and number density $n = N_{\rm LC}[(4/3)\pi R^2 L]^{-1}$. The corresponding aspect ratio R/L is equal to the inverse trap frequency ratio $\omega_{z({\rm LC})}/\omega_{r({\rm LC})}$ as expected for the case of noninteracting ions (→ Sect. 6.1). On the other hand, in the low-temperature limit where the Debye length (2.4) becomes negligibly small compared to all plasma dimensions, the number density n is expected to reach its maximum value $n_0 = 2\epsilon_0 (m_{\rm LC}/Q_{\rm LC}^2)\,\omega_{0({\rm LC})}^2$ (→ Sect. 2.2.2). In this limit, the spatial distribution of laser-cooled ions is approximated by a spheroid of constant number density n_0, radius R_0, and half-length L_0, determined by the two requirements $N_{\rm LC} = (4/3)\pi R_0^2 L_0\, n_0$ and $R_0/L_0 = \omega_{z({\rm LC})}/\omega_{r({\rm LC})}$. According to the latter, the effect of space charge on the outer plasma shape is neglected since this would imply a non-trivial dependence of the aspect ratio R_0/L_0 on the trap frequency ratio $\omega_{z({\rm LC})}/\omega_{r({\rm LC})}$ (→ Fig. 2.2). Finally, in order to adapt to the two limiting cases considered so far, the following expressions are chosen for the radius R and half-length L, each as function of the temperature $T_{\rm LC}$:

$$R(T_{\rm LC}) \;=\; \sqrt{R_0^2 + \frac{6\,k_B\,T_{\rm LC}}{m_{\rm LC}\,\omega_{r({\rm LC})}^2}} \tag{2.9a}$$

$$L(T_{\rm LC}) \;=\; \sqrt{L_0^2 + \frac{6\,k_B\,T_{\rm LC}}{m_{\rm LC}\,\omega_{z({\rm LC})}^2}} \tag{2.9b}$$

In Eqs. (2.9), $R_0^3 \stackrel{\rm def}{=} (3N_{\rm LC}/4\pi n_0)\,\omega_{z({\rm LC})}/\omega_{r({\rm LC})}$ and $L_0^3 \stackrel{\rm def}{=} (3N_{\rm LC}/4\pi n_0)\,\omega_{r({\rm LC})}^2/\omega_{z({\rm LC})}^2$. The number density $n = N_{\rm LC}[(4/3)\pi R^2 L]^{-1}$ may thus be written as

$$n(T_{\rm LC}) \;=\; n_0 \left[\frac{Q_{\rm LC}\,\phi_0}{Q_{\rm LC}\,\phi_0 + 3\,k_B\,T_{\rm LC}}\right]^{3/2} , \tag{2.10}$$

where $\phi_0 \stackrel{\rm def}{=} (m_{\rm LC}/2Q_{\rm LC})\,\omega_{r({\rm LC})}^2 R_0^2 = (m_{\rm LC}/2Q_{\rm LC})\,\omega_{z({\rm LC})}^2 L_0^2$ is the so-called *fluid level* [58]. Thus, according to Eqs. (2.9) and Eq. (2.10), the cloud of laser-cooled ions at temperature $T_{\rm LC}$ is approximated by constant density spheroid with radius $R(T_{\rm LC})$, half-length $L(T_{\rm LC})$, and number density $n(T_{\rm LC})$.

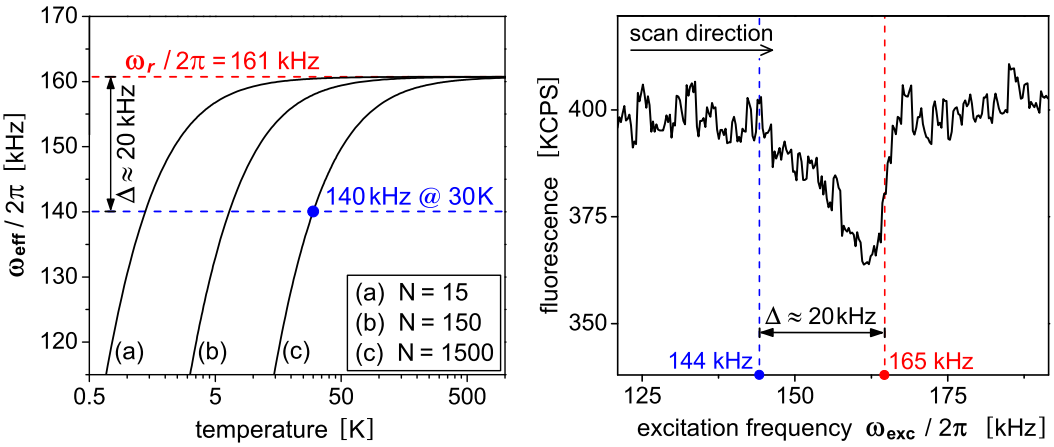

Figure 2.3: Left: *Effective trap frequency ω_{eff} [Eq. (2.12)] of a sympathetically cooled ion with mass $m_{SC} = 15$ u, moving within the cloud of $N_{LC} = 15$ (a), 150 (b), and 1500 (c) laser-cooled $^9Be^+$ ions ($m_{LC} = 9$ u). Typical trap frequencies of $\omega_{r(LC)}/2\pi = 271$ kHz and $\omega_{z(LC)}/2\pi = 69.7$ kHz were assumed (→ Sect. 3.2).* ***Right:*** *Excitation frequency scan, showing the presence of sympathetically cooled ions with a mass in the range of $14\text{ u} \leq m_{SC} \leq 16$ u. According to the simplified model of LCF-MS (→ Sect. 2.3.2), the fluorescence signal starts to decrease at $\omega_{\text{exc}} \approx \omega_{\text{eff}}(T_{LC})$, where T_{LC} is the initial temperature of the $^9Be^+$ ions. This is followed by a step-like increase at $\omega_{\text{exc}} = \omega_{r(SC)}$, i.e. the nominal trap frequency of the sympathetically cooled ions. Assuming $N_{LC} = 1500$ and $T_{LC} = 30K$, the theoretical value $(\omega_{r(SC)} - \omega_{\text{eff}})/2\pi \approx 20$ kHz agrees well with the measured fluorescence signal, as indicated by the blue and red dotted lines. The assumptions are consistent with the experimental conditions described in Sect. 5.3.1.*

With the above approximation, a simple analytical expression can be derived for the *effective* trap potential, i.e. the superposition of the time-averaged trap potential and the space charge potential of the laser-cooled ions, as seen by a sympathetically cooled ion. Assuming trap frequencies $\omega_{r(\text{LC})} \gg \omega_{z(\text{LC})}$, the spatial distribution of laser-cooled ions is highly prolate ($R \ll L$). The corresponding space charge potential at $z = 0$ is given by

$$\phi_{\text{spc}}(r) \;=\; \frac{n\,Q_{\text{LC}}}{4\,\epsilon_0} \cdot \begin{cases} R^2\Big(1 + 2\,\ln\dfrac{2\,L}{R}\Big) - r^2 & \text{if} \quad r < R \\[2ex] 2\,R^2\,\ln\dfrac{2\,L}{r} & \text{if} \quad R < r \ll L\ , \end{cases} \tag{2.11}$$

where radius R, half-length L, and number density n are given by Eqs. (2.9) and Eq. (2.10), respectively. Eq. (2.11) may be derived as the limiting case $R \ll L$ of the electrostatic potential of a prolate spheroid ($R > L$) with constant charge density $\rho = nQ_{\text{LC}}$ as given in Ref. [70]. Thus, for a sympathetically cooled ion with charge Q_{SC} and mass m_{SC}, the *effective* trap potential at $z = 0$ is given by the superposition of the time-averaged trap potential $\phi_{\text{trap}}(r) = (m_{\text{SC}}/2Q_{\text{SC}})\,\omega^2_{r(\text{SC})}\,r^2$

and the space charge potential $\phi_{\mathrm{spc}}(r)$ [Eq. (2.11)]. Within the cloud of laser-cooled ions ($r < R$), the *effective* trap potential is harmonic and thus may be written as $\phi_{\mathrm{eff}}(r) = (m_{\mathrm{SC}}/2Q_{\mathrm{SC}})\,\omega_{\mathrm{eff}}^2 r^2$ with *effective* transverse trap frequency

$$\omega_{\mathrm{eff}} \;=\; \sqrt{\omega_{r(\mathrm{SC})}^2 - \frac{n(T_{\mathrm{LC}})\,Q_{\mathrm{LC}}\,Q_{\mathrm{SC}}}{2\,\epsilon_0\,m_{\mathrm{SC}}}} \quad . \tag{2.12}$$

Here, $\omega_{r(\mathrm{SC})}$, Q_{SC}, and m_{SC} denote the transverse trap frequency, charge, and mass of the sympathetically cooled ions, respectively, while $n(T_{\mathrm{LC}})$ and Q_{LC} denote the number density (2.10) and charge of the laser-cooled ions, respectively. It should be noted however, that the subscripts LC and SC are merely used to distinguish between two different ion species, since no assumptions have been made with regards to sympathetic or laser-cooling.

In order to give a numerical example, Fig. 2.3 (left) shows three plots of the *effective* transverse trap frequency (2.12) as a function of temperature T_{LC}. To this end, a sympathetically cooled ion with mass $m_{\mathrm{SC}} = 15\,\mathrm{u}$ is assumed to move within the cloud of $N_{\mathrm{LC}} = 15$, 150, and 1500 laser-cooled $^9\mathrm{Be}^+$ ions. With decreasing temperature T_{LC}, the trap potential is more and more shielded out, resulting in a decrease of ω_{eff}. The onset of shielding occurs the earlier the larger the ion cloud is. In LCF-MS, the shift of the *effective* transverse trap frequency of the sympathetically cooled ions due to space charge of the laser-cooled ions has major effect on the fluorescence signal shape. This is indicated in Fig. 2.3 (right).

2.3.2 Simplified Model of LCF-MS

In the LCF-MS mass spectra, each dip in the fluorescence signal indicates the resonant kinetic excitation of a particular sympathetically cooled ion species with a given mass-to-charge ratio m/Q. If both the sympathetically and the laser-cooled ions are in a cloud-like state, the frequencies where resonant kinetic excitations are observed usually show good agreement with the theoretical single particle frequencies $\omega_r \sim Q/m$. Thus, mass-to-charge ratios can be easily assigned to most dips in the fluorescence signal. However, the observed dip shapes in general strongly deviate from a simple symmetric shape and considerably vary (among others) with: (i) the strength of the applied kinetic excitation, (ii) the scan direction and scan rate of the excitation frequency scan, and (iii) the temperature and composition of the whole trap content. A better theoretical understanding of the underlying physical processes therefore would be helpful, e.g., in order to optimize LCF-MS with respect to mass accuracy. To this end, one could start from a molecular dynamics (MD) simulation like that presented in Ref. [48], which includes the full time-dependence of the rf trapping fields to accurately account for rf heating. An additional term describing external kinetic excitation and being added to the equation of motion then would extent the simulation to the case of LCF-MS. However, in order to reproduce a complete dip in a LCF-MS mass spectrum, a scan of the excitation frequency over

a range of at least 10 kHz would have to be simulated. With a realistic scan rate of 1 kHz/s and a typical rf trap frequency of $\Omega/2\pi = 10\,\mathrm{MHz}$ ($\rightarrow$ Sect. 3.2), this corresponds to a duration of more than 10^8 rf periods. Such a simulation would require unreasonably long computing time, especially for the case of a realistic total number of at least 10 ions. For this reason, a simplified model of LCF-MS was derived by Baba and Waki in Ref. [54], based on the time-averaged trap potential approximation ($\rightarrow$ Sect. 2.1) and including the effects of laser cooling, rf heating, sympathetic cooling/heating, and space charge. In the following, a brief review is given of the model in a rather qualitative fashion.

The simplified model of LCF-MS describes the external kinetic excitation of a number of N_{SC} sympathetically cooled (SC) ions, confined in a linear rf trap together with a much larger number $N_{\mathrm{LC}} \gg N_{\mathrm{SC}}$ of laser-cooled (LC) ions. In particular, the SC ions are assumed to move in the superposition of the time-averaged trap potential $\phi_{\mathrm{trap}} = m_{\mathrm{SC}}(\omega_{r(\mathrm{SC})}^2 r^2 + \omega_{z(\mathrm{SC})}^2 z^2)/2Q_{\mathrm{SC}}$ and the space charge potential of the LC ions, where $\omega_{r(\mathrm{SC})} \gg \omega_{z(\mathrm{SC})}$. Furthermore, the LC ions are assumed to be in a cloud-like state, thus with a spatial distribution which is more or less Gaussian ($\rightarrow$ Sect. 6.1). However, in order to reduce the mathematical complexity of the model, the spatial distribution of laser cooled ions is approximated by a constant density spheroid with radius $R(T_{\mathrm{LC}})$ [Eq.(2.9a)], half-length $L(T_{\mathrm{LC}})$ [Eq.(2.9b)], and number density $n(T_{\mathrm{LC}})$ [Eq.(2.10)] as described in the previous section. Thus, no spatial dependence of, e.g., the ion-ion collision rates has to be considered within the cloud of LC ions. The temperature T_{LC} and mean kinetic energy W_{LC} of the LC ions are related by $W_{\mathrm{LC}} = (5/2)k_B T_{\mathrm{LC}}$ [a], where the change in time of W_{LC} is governed by the rate equation

$$N_{\mathrm{LC}}\dot{W}_{\mathrm{LC}} \;=\; N_{\mathrm{LC}}\frac{\Delta W_{\mathrm{LC}}}{\Delta t}\bigg|_{\mathrm{lc}} + N_{\mathrm{LC}}\frac{\Delta W_{\mathrm{LC}}}{\Delta t}\bigg|_{\mathrm{rfh}} - N_{\mathrm{SC}}\frac{\Delta W_{\mathrm{SC}}}{\Delta t}\bigg|_{\mathrm{sc}} . \tag{2.13}$$

Here, the rates $\Delta W_i/\Delta t\,|_j$ denote the change of mean kinetic energy per unit time and ion, either laser-cooled ($i = \mathrm{LC}$) or sympathetically cooled ($i = \mathrm{SC}$), due to laser cooling ($j = \mathrm{lc}$), rf heating ($j = \mathrm{rfh}$), and sympathetic cooling ($j = \mathrm{sc}$). The rates $\Delta W_i/\Delta t\,|_j$ are functions of both W_{LC} and W_{SC}, explicit expressions of which are found in Ref. [54]. Here, only qualitative descriptions will be given.

The **laser cooling** rate $\Delta W_{\mathrm{LC}}/\Delta t\,|_{\mathrm{lc}}$ relies on a semi-classical description which treats the internal states of the LC ions with a quantum mechanical two-level model and the ion motion as classical motion. If expressed as a function of W_{LC}, the particular shape of $\Delta W_{\mathrm{LC}}/\Delta t\,|_{\mathrm{lc}}$ is determined by a set of parameters regarding the cooling transition and the cooling laser. In particular, $\omega_L < \omega_A \Rightarrow \Delta W_{\mathrm{LC}}/\Delta t\,|_{\mathrm{lc}} < 0$,

[a] The total thermal energy of an ion in the time-averaged trap potential is $3k_B T$, where the mean kinetic and potential energy each contribute $(3/2)k_B T$. However, in a linear rf trap, the mean potential energy of the *transverse* motion may as well be regarded as the mean kinetic energy of the *micromotion* [58]. Thus, a mean kinetic energies of $W_i = (5/2)k_B T_i$ is assumed in Ref. [54], where $i \in \{LC, SC\}$. This difference becomes of particular importance when calculating the sympathetic cooling rate in Ref. [29].

i.e. *cooling* of the LC ions is achieved by red-detuning the frequency ω_L of the cooling laser with respect to the frequency ω_A of the cooling transition. A derivation of $\Delta W_{\mathrm{LC}}/\Delta t\,|_{\mathrm{lc}}$ is found in Refs. [78–80].

The **rf heating** rate $\Delta W_{\mathrm{LC}}/\Delta t\,|_{\mathrm{rfh}}$ which for the main part is adopted from Ref. [81], accounts for the transfer of energy from the rf field of the linear trap to the mean kinetic energy of the LC ions via ion-ion collisions. However, while in Ref. [81] only collisions between the LC ions are considered, $\Delta W_{\mathrm{LC}}/\Delta t\,|_{\mathrm{rfh}}$ includes collisions between the LC and SC ions as well, due to a slight modification in Ref. [54]. In particular, $\Delta W_{\mathrm{LC}}/\Delta t\,|_{\mathrm{rfh}} \sim \gamma'(W_{\mathrm{LC}}, W_{\mathrm{SC}})$, where γ' is the ion-ion collision rate which gives the average number of collisions per unit time, a LC ion suffers from ions of either species [b].

The **sympathetic cooling** rate $\Delta W_{\mathrm{SC}}/\Delta t\,|_{\mathrm{sc}}$, derived by Baba and Waki in Ref. [29], accounts for the transfer of kinetic energy from the SC ions to the LC ions via ion-ion collisions in the presence of the rf field of the linear trap. Accordingly, $\Delta W_{\mathrm{SC}}/\Delta t\,|_{\mathrm{sc}}$ is equal to zero if the SC ions are located outside the cloud of laser cooled ions. Within the cloud, $\Delta W_{\mathrm{SC}}/\Delta t\,|_{\mathrm{sc}} \sim \gamma(W_{\mathrm{LC}}, W_{\mathrm{SC}})\cdot(W_{\mathrm{LC}} - W_{\mathrm{SC}})$, where $\gamma(W_{\mathrm{LC}}, W_{\mathrm{SC}})$ is the ion-ion collision rate which gives the average number of collisions per unit time, a SC ion suffers from the LC ions. In particular, $W_{\mathrm{LC}} < W_{\mathrm{SC}} \wedge m_{\mathrm{SC}} > (8/15)\, m_{\mathrm{LC}} \Rightarrow \Delta W_{\mathrm{SC}}/\Delta t\,|_{\mathrm{sc}} < 0$, i.e. *cooling* of the SC ions not only requires the temperature of the LC ions to be lower than that of the SC ions but also the condition $m_{\mathrm{SC}} > (8/15)\, m_{\mathrm{LC}}$ to be fulfilled. Thus, according to the sympathetic cooling rate $\Delta W_{\mathrm{SC}}/\Delta t\,|_{\mathrm{sc}}$, ions with a mass lower than $(8/15)\, m_{\mathrm{LC}} \approx 0.53\, m_{\mathrm{LC}}$ can not be sympathetically cooled at all. In that case, the transfer of energy from the micromotion of the LC ions to the secular motion of the SC ions is predicted to become dominant.

In addition to the rate equation (2.13), a simplified equation of motion is formulated for the SC ions. Since a much smaller number of SC ions than LC ions is assumed, Coulomb interactions between the SC ions can be neglected. Also, only a small spread of SC ions along the trap axis is expected compared to the axial dimensions of the cloud of LC ions. Thus, a single equation of motion

$$m_{\mathrm{SC}}\,\ddot{r} \;=\; -Q_{\mathrm{SC}}\,\frac{d}{dr}\Big[\phi_{\mathrm{trap}}(r) + \phi_{\mathrm{spc}}(r)\Big] + \frac{1}{\dot{r}}\,\frac{\Delta W_{\mathrm{SC}}}{\Delta t}\bigg|_{\mathrm{sc}} + \frac{Q_{\mathrm{SC}}\,U_{\mathrm{exc}}}{x_0}\cos(\omega_{\mathrm{exc}}\,t) \quad (2.14)$$

applies to the whole number of SC ions moving in the plane $z = 0$, where r is the transverse displacement from the trap axis. The three terms on the right-hand side of Eq. (2.14) can be understood as follows. The first term accounts for the motion of SC ions in the superposition of the time-averaged trap potential $\phi_{\mathrm{trap}}(r) = (m_{\mathrm{SC}}/2Q_{\mathrm{SC}})\,\omega_r^2 r^2$ and the space charge potential $\phi_{\mathrm{spc}}(r)$ [Eq. (2.11)]

[b] As argued in Ref. [29], rf heating can not be adequately modeled by ion-ion collisions but rather relies on many-ion ($n > 2$) collisions (see also Refs. [78,82]). Nevertheless, despite the lack of an adequate model, the rf heating rate $\Delta W_{\mathrm{LC}}/\Delta t\,|_{\mathrm{rfh}}$ can be justified by comparison with MD simulations as was argued in Ref. [54].

Interaction	Resulting Effect	Corresponding Expression	
LC-LC Coulomb	Coulomb repulsion	$n(T_{\mathrm{LC}})$	$\rightarrow$ note 1
	rf heating	$\Delta W_{\mathrm{LC}}/\Delta t\,\big\vert_{\mathrm{rfh}}$	
LC-SC Coulomb	*effects on LC ions:*		
	Coulomb repulsion	neglected	$(N_{\mathrm{SC}} \ll N_{\mathrm{LC}})$
	sympathetic heating	$-\Delta W_{\mathrm{SC}}/\Delta t\,\big\vert_{\mathrm{sc}}$	
	rf heating	$\Delta W_{\mathrm{LC}}/\Delta t\,\big\vert_{\mathrm{rfh}}$	
	effects on SC ions:		
	Coulomb repulsion	$\phi_{\mathrm{spc}}(r)$	
	sympathetic cooling	$\Delta W_{\mathrm{SC}}/\Delta t\,\big\vert_{\mathrm{sc}}$	
	rf heating	$\Delta W_{\mathrm{SC}}/\Delta t\,\big\vert_{\mathrm{sc}}$	$\rightarrow$ note 2
SC-SC Coulomb	Coulomb repulsion	neglected	$(N_{\mathrm{SC}} \ll N_{\mathrm{LC}})$
	rf heating	neglected	$(N_{\mathrm{SC}} \ll N_{\mathrm{LC}})$

Table 2.1: *Overview of the various effects resulting from Coulomb interactions between the laser-cooled ions (LC-LC), the laser-cooled and sympathetically cooled ions (LC-SC), and the sympathetically cooled ions (SC-SC), and their incorporation into the simplified model of LCF-MS.* ***Notes: (1)*** *In the number density $n(T_{LC})$ [Eq. (2.10)], LC-LC Coulomb repulsion is reflected by the fact that $n(T_{LC})$ is bound by an upper limit for $T_{LC} \rightarrow 0$. In the simplified model of LCF-MS, $n(T_{LC})$ enters into expressions $\phi_{spc}(r)$, $\Delta W_{LC}/\Delta t\,\big\vert_{rfh}$, and $\Delta W_{SC}/\Delta t\,\big\vert_{sc}$, the latter two via the collision rates $\gamma'(W_{LC}, W_{SC})$ and $\gamma(W_{LC}, W_{SC})$, respectively.* ***(2)*** *By allowing for the transfer of energy from the rf field of the linear trap to the secular motion of the SC ions, the sympathetic cooling rate $\Delta W_{SC}/\Delta t\,\big\vert_{sc}$ accounts for rf heating as well. However, no adequate description of rf heating is given by $\Delta W_{SC}/\Delta t\,\big\vert_{sc}$ as can be seen from the fact that $m_{LC}=m_{SC} \wedge W_{LC}=W_{SC} \Rightarrow \Delta W_{SC}/\Delta t\,\big\vert_{sc}=0$ [29].*

of the LC ions. The second term accounts for the effect of sympathetic cooling/heating, where $\Delta W_{\mathrm{SC}}/\Delta t\,\big\vert_{\mathrm{sc}}$ is the the sympathetic cooling rate from Eq. (2.13). In particular, this is a damping term if $\Delta W_{\mathrm{SC}}/\Delta t\,\big\vert_{\mathrm{sc}} < 0$, i.e. if sympathetic *cooling* of the SC ions takes place. Finally, the third term accounts for the external kinetic excitation, where $U_{\mathrm{exc}} \cos(\omega_{\mathrm{exc}} t)$ is the applied excitation voltage and x_0 is a constant determined by the excitation electrode geometry. In Eqs. (2.13) and (2.14), Coulomb interactions between the individual ions are treated in various levels of approximation as summarized in Tab. 2.1. In contrast to this, no level of approximation is used in a molecular dynamics (MD) simulation.

With the two coupled equations (2.13) and (2.14), a LCF-MS mass spectrum can be modeled by calculating the change in fluorescence of the LC ions during a scan of the excitation frequency ω_{exc}. In particular, numerical solution of Eqs. (2.13) and (2.14) yields the mean kinetic energy $W_{\mathrm{LC}}(t)$ of the LC ions and the transverse displacement $r(t)$ of the SC ions, each as a function of time. From this, the corresponding temperatures $T_{\mathrm{LC}} = 2W_{\mathrm{LC}}/5k_B$ and $T_{\mathrm{SC}} = m_{\mathrm{SC}}\langle \dot{r}^2(t)\rangle/k_B$ are calculated together with the fluorescence $N_{\mathrm{LC}} \cdot \bar{\Gamma}_{\mathrm{ph}}(W_{\mathrm{LC}})$. Here, $\bar{\Gamma}_{\mathrm{ph}}$ denotes the mean photon scattering rate of the LC ions which will be derived in appendix B. In order to gain

more insight into the mechanisms that lead to the characteristic asymmetric shape of the fluorescence dips, usually observed in LCF-MS, the *effective* trap frequency ω_{eff} of the SC ions is calculated as well. Here, ω_{eff} is defined as the frequency of free oscillation of the SC ions in the *effective* trap potential $\phi_{\text{trap}}(r) + \phi_{\text{spc}}(r)$. As was shown in Sect. 2.3.1, a simple analytical expression can be derived for ω_{eff} in case where the motion of SC ions is restricted entirely to regions within the cloud of LC ions. However, in general the motion of SC ions extends well beyond the cloud of LC ions which leads to an anharmonic oscillation. Thus, in the general case, ω_{eff} has to be calculated numerically. Nevertheless, since ω_{eff} is defined as the frequency of free oscillation of the SC ions in the time averaged trap potential $\phi_{\text{trap}}(r) = (m_{\text{SC}}/2Q_{\text{SC}})\,\omega_{r(\text{SC})}^2 r^2$ modified by space charge of the LC ions, a general rule can be stated: the higher the temperature T_{LC} of the LC ions, the more ω_{eff} increases. This is due to the thermal expansion of the cloud of LC ions by which space charge becomes less pronounced. In the limit $T_{\text{LC}} \to \infty$, the *effective* trap frequency ω_{eff} will reach the *nominal* trap frequency $\omega_{r(\text{SC})}$.

Figs. 2.4 and 2.5, taken from Ref. [54], each shows a numerical solution of the coupled equations (2.13) and (2.14). In both figures, a scan of the excitation frequency ω_{exc} is assumed across the *nominal* trap frequency $\omega_{r(\text{SC})}$ of the SC ions. However, in Fig. 2.4, a scan of ω_{exc} from below to above $\omega_{r(\text{SC})}$ is assumed, while in Fig. 2.5, a scan of ω_{exc} from above to below $\omega_{r(\text{SC})}$ is assumed. Each numerical solution is represented by plots versus time of (i) the *effective* trap frequency ω_{eff} of the SC ions, (ii) the temperatures T_{LC} and T_{SC} of the LC and SC ions, and (iii) the fluorescence of the LC ions. In solving Eqs. (2.13) and (2.14), $N_{\text{LC}} = 40$ LC ions with mass $m_{\text{LC}} = 24\,\text{u}$ and charge $Q_{\text{LC}} = 1\,\text{e}$ were assumed to sympathetically cool $N_{\text{SC}} = 10$ SC ions with mass $m_{\text{SC}} = 26\,\text{u}$ and charge $Q_{\text{SC}} = 1\,\text{e}$. Furthermore, the parameters characterizing the time-averaged trap potential, laser cooling, and the external kinetic excitation were chosen to match the experiments described in Refs. [50, 77]. In these experiments, laser-cooled $^{24}\text{Mg}^+$ ions were used to sympathetically cool $^{26}\text{Mg}^+$ ions as well as other species of atomic and molecular ions. Despite the specific assumptions made, the mechanisms revealed by the numerical solutions are quite general and thus will be described below. Since restricted to a rather qualitative description, all numbers are omitted from the plot axes in Figs. 2.4 and 2.5.

I. Scan of ω_{exc} from below to above $\omega_{r(\text{SC})}$

In Fig. 2.4, the scan of the excitation frequency ω_{exc} starts well below the *effective* trap frequency ω_{eff} which due to space charge of the LC ions is shifted below the *nominal* trap frequency $\omega_{r(\text{SC})}$. In consequence, no kinetic excitation of the SC ions takes place and the temperature T_{SC} adapts to the temperature T_{LC} of the LC ions, the latter being determined by the balance between laser cooling and rf heating [Eq. (2.13) with $\Delta W_{\text{SC}}/\Delta t\,|_{\text{sc}} \to 0$]. Next, when ω_{exc} approaches the *effective* trap frequency ω_{eff}, kinetic excitation of the SC ions sets in and both temperatures T_{SC} and T_{LC} start to rise, the latter caused by sympathetic heating of the LC ions. Thus, the cloud of LC ions expands and space charge becomes less pronounced. Since this in turn implies an increase in *effective* trap frequency

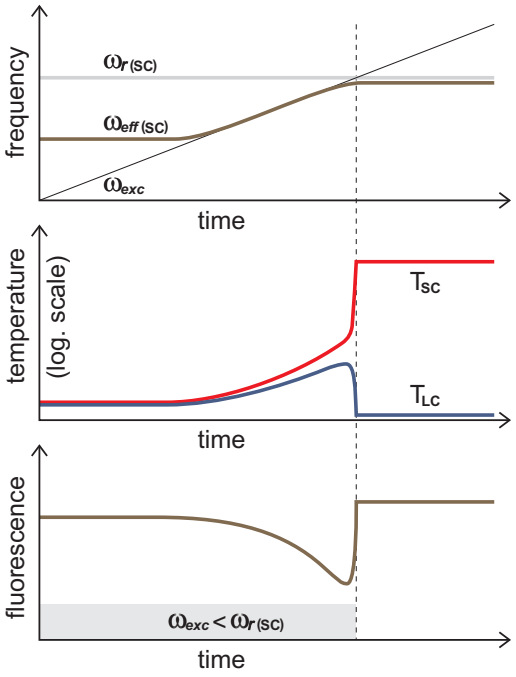

Fig. 2.4: *Numerical solution of Eq. (2.13) and Eq. (2.14), showing an* ***upward*** *excitation frequency scan. The graphical representation has been slightly changed with respect to Ref. [54].*

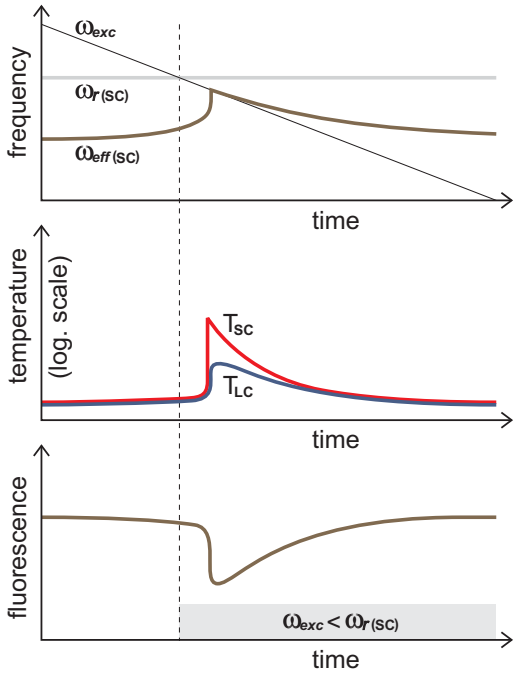

Fig. 2.5: *Numerical solution of Eq. (2.13) and Eq. (2.14), showing a* ***downward*** *excitation frequency scan. The graphical representation has been slightly changed with respect to Ref. [54].*

ω_{eff}, a negative feedback is established which in effect locks ω_{eff} to the excitation frequency ω_{exc} (a further increase of ω_{eff} above the excitation frequency ω_{exc} would decouple the SC ions from the external excitation). As ω_{exc} approaches the *nominal* trap frequency $\omega_{r(\mathrm{SC})}$, the difference in temperature between T_{LC} and T_{SC} exceeds a certain limit above which the sympathetic cooling rate $\Delta W_{\mathrm{SC}}/\Delta t\,|_{\mathrm{sc}}$ starts to decrease and quickly tends to zero. As a result, the SC ions are decoupled from the LC ions and the negative feedback is broken. The LC ions are quickly cooled down, while the temperature T_{SC} of the SC ions strongly increases. Thus, when ω_{exc} finally reaches the *nominal* trap frequency $\omega_{r(\mathrm{SC})}$ (dotted line in Fig. 2.4), the SC ions oscillate with a large amplitude and are mainly located outside the cloud of LC ions which has contracted due to the drop in temperature T_{LC}. In addition, damping of the motion of SC ions inside the cloud of LC ions is almost negligible since the sympathetic cooling rate $\Delta W_{\mathrm{SC}}/\Delta t\,|_{\mathrm{sc}}$ in Eq. (2.14) has strongly decreased due to the large difference in temperature between T_{LC} and T_{SC}. Thus, when ω_{exc} finally reaches the *nominal* trap frequency $\omega_{r(\mathrm{SC})}$, almost undamped kinetic excitation of the SC ions takes place. This may result in their loss from the trap, depending on the strength of the applied kinetic excitation as well as the depth of the trap potential. In Fig. 2.4, the SC ions are not lost from the trap but rather are heated up to a temperature sufficiently high to permanently decouple them from the LC ions. Finally, after the excitation frequency ω_{exc} is scanned across the *nominal* trap frequency $\omega_{r(\mathrm{SC})}$, the temperature T_{LC} of the LC ions is determined again by

the balance between laser-cooling and rf heating [Eq. (2.13) with $\Delta W_{\mathrm{SC}}/\Delta t\,|_{\mathrm{sc}} \rightarrow 0$]. However, since collisions between the LC and the SC ions do not contribute to the rf heating rate $\Delta W_{\mathrm{LC}}/\Delta t\,|_{\mathrm{rfh}}$ anymore, the temperature T_{LC} even drops below its value at the start of the excitation frequency scan. In Fig. 2.4, the change in temperature T_{LC} during the excitation frequency scan is reflected by a corresponding change in fluorescence of the LC ions.

II. Scan of ω_{exc} from above to below ω_r

In Fig. 2.5, the same parameters were chosen as in Fig. 2.4, except from a reversed scan direction and a 20-fold increase in excitation amplitude U_{exc}. The scan of the excitation frequency ω_{exc} starts well above the *effective* trap frequency ω_{eff}, leading to the same initial conditions as in Fig. 2.4. When ω_{exc} is scanned across the *nominal* trap frequency $\omega_{r(\mathrm{SC})}$ (dotted line in Fig. 2.5), kinetic excitation of the SC ions already takes place to a certain extent. This is reflected by the gradual increase in *effective* trap frequency ω_{eff}, caused by the sympathetic heating of the LC ions due to which space charge becomes less pronounced. After ω_{exc} has been scanned across the *nominal* trap frequency $\omega_{r(\mathrm{SC})}$, both ω_{exc} and the *effective* trap frequency ω_{eff} approach each other up to the point where a positive feedback is triggered: the smaller the difference between ω_{exc} and ω_{eff}, the more effective the coupling of the kinetic excitation to the SC ions becomes. This in turn further reduces the difference between ω_{exc} and ω_{eff}, due to the increased kinetic excitation of the SC ions and the resulting sympathetic heating of the LC ions, leading to an increase in ω_{eff} as well. Thus, strong kinetic excitation of the SC ions sets in, which is reflected by a step-like increase in temperature T_{SC}. Furthermore, sympathetic heating of the LC ions results in a step-like increase in temperature T_{LC} as well, and a corresponding increase in *effective* trap frequency ω_{eff}. The particular excitation frequency ω_{exc} at which the positive feedback sets in, in general depends on the strength of the applied kinetic excitation: with increasing excitation amplitude U_{exc}, the onset of positive feedback is more and more shifted towards the *nominal* resonance $\omega_{\mathrm{exc}} = \omega_{r(\mathrm{SC})}$ (dotted line in Fig. 2.5). In the limit of a high excitation amplitude U_{exc}, almost undamped kinetic excitation of the SC ions is expected to take place as already described under case I. However, in the numerical simulations presented in Ref. [54], no loss of SC ions from the trap was observed in the downward excitation frequency scans, up to an increase of U_{exc} by a factor of 30 with respect to Fig. 2.4. The positive feedback is stopped once the *effective* trap frequency ω_{eff} has reached the excitation frequency ω_{exc} (a further increase of ω_{eff} above ω_{exc} would decouple the SC ions from the external kinetic excitation). Finally, the positive feedback turns into a negative feedback as already described under case I. At the end of the excitation frequency scan, the temperatures T_{LC} and T_{SC} of the LC and SC ions, as well as the *effective* trap frequency ω_{eff}, again reach their initial values. The change in temperature T_{LC} is reflected by a corresponding change in fluorescence of the LC ions.

The numerical solutions shown in Figs. 2.4 and 2.5 both reproduce the characteristic asymmetric shape of the fluorescence dips, usually observed in LCF-MS. In particular, the gradual decrease/increase in fluorescence on the low-frequency

side of the frequency scans is explained by a negative feedback which more or less locks the *effective* trap frequency ω_{eff} to the applied excitation frequency ω_{exc}. Furthermore, two different explanations are provided for the step-like increase in fluorescence on the high-frequency side of the frequency scans, depending on the scan direction: (i) decoupling of the SC ions from the LC ions at the *nominal* resonance $\omega_{\text{exc}} = \omega_{r(\text{SC})}$ in Fig. 2.4, and (ii) onset of strong kinetic excitation of the SC ions at $\omega_{\text{exc}} < \omega_{r(\text{SC})}$ in Fig. 2.5. Thus, a choice of scan direction is suggested as follows. If a possible loss of SC ions shall be avoided, a scan of ω_{exc} from above to below $\omega_{r(\text{SC})}$ should be preferred. On the other hand, if mass accuracy matters, a scan of ω_{exc} from below to above $\omega_{r(\text{SC})}$ should be preferred.

Chapter 3

UHV Setup

The experimental setup, used to perform the experiments described in chapters 5–7, consists of two main parts: (i) the cooling laser system which will be described in chapter 4, and (ii) the UHV setup together with the photomultiplier tube (PMT) and CCD camera which will be described in the present chapter. Both (i) and (ii) are based on respective previous versions, designed and built at the University of Konstanz as described in detail in Refs. [1,2]. Thus, only major modifications with respect to Refs. [1, 2] shall be considered here, besides from a short overview of the complete UHV setup which will be given in **Sect. 3.1.** In particular, major modifications and/or addition of new components turned out to be necessary in case of the linear rf trap (→ **Sect. 3.2**), the trap supply electronics (→ **Sect. 3.3**), and both the PMT and the CCD camera optical setup (→ **Sect. 3.4**). Accordingly, the term *new* shall be used here in order to distinguish these components from their respective previous versions, described in Refs. [1,2], which shall be referred to as *old*. Finally, an alternative trap setup was designed and built for future experiments, including a curved linear rf trap and a miniature electron gun. This will be described in appendix C.

3.1 Overview of the Complete Setup

The ultra-high vacuum (UHV) which is required to minimize collisions between the trapped ions and the residual background gas, was provided by the vacuum chamber and pumps described in Refs. [1,2]. After a typical bakeout of 5 days at a temperature of 180 – 220°C, a final pressure of $P < 1 \cdot 10^{-10}$ mbar was reached inside the vacuum chamber. This was measured with an Bayard-Alpert type pressure gauge (*Varian*, type *UHV-24p*). For a more detailed vacuum analysis, a residual gas analyzer (RGA) was used (*Vacuum Generators*, type *Smart IQ+100D*). Typical RGA mass spectra showed peaks at $m/Q = 14, 16, 20, 28, 32$, and 40 u/e with relative peak heights of 16, 5, 7, 100, 11, and 18 %, respectively, which were assigned to N^+ /N_2^{++}, O^+ /O_2^{++}, Ar^{++}, N_2^+, O_2^+ and Ar^+, respectively (see, e.g., Ref. [83]).

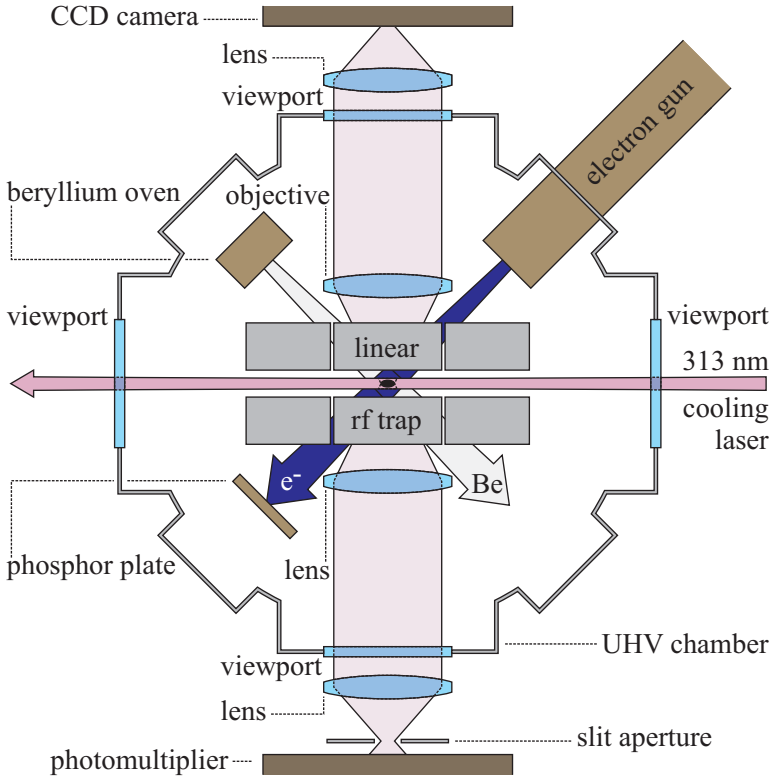

Figure 3.1: *Schematic overview of the complete ultra-high vacuum (UHV) setup, including the linear rf trap, Be oven, electron gun, and the fluorescence detection optics.*

Fig. 3.1 shows a schematic overview of the complete UHV setup, including the linear rf trap, Be oven, electron gun, and the fluorescence detection optics. Laser light at 313 nm wavelength delivered from the cooling laser system was directed along the trap axis and passed through two fused silica UV viewports (*Caburn-MDC*, type *DUV-200*), each attached to a DN100CF flange. The beam waist was located in the trap center with a typical size of $w_0 = 500 - 800\,\mu$m. In the experiments, care was taken to prevent 313 nm stray light scattered from the viewports, from further penetrating into the vacuum chamber and reaching the trap region. To this end, two blackened baffles were placed behind the viewports, each made of stainless steel sheet which was bent into appropriate shape and coated with a colloidal graphite (*Acheson Industries*, type *Aquadad 18 %*). Loading of the linear rf trap with $^9Be^+$ ions was achieved by evaporating Be atoms from a small oven (→ Sect. 3.2) and by electron impact ionization in the trap center using a commercial electron gun (*Kimball*, type *EFG-8*). Since this electron gun is of a flood gun type with a typical beam diameter of $\phi = 1$ cm and a current of $I = 20\,\mu$A, charging of the trap electrodes was likely to occur. As a consequence, development of a new trap supply electronics (→ Sect. 3.3) proved necessary, providing low impedance connections between the trap electrodes and the corresponding dc voltage supplies. Finally, a phosphor plate was used to optimize the transmission of the electron beam through the linear rf trap center. As will be further explained in chapter 4, a weak static magnetic field applied along the trap axis was required as a quanti-

zation axis for the $^9Be^+$ ions, in order to realize a closed cooling transition between the $^2S_{1/2}(F=2, m_F=2)$ ground and the $^2P_{3/2}(F=3, m_F=3)$ excited state. The magnetic field was generated by two coils in nearly Helmholtz configuration, each consisting of $N=150$ turns of insulated copper wire wrapped around the DN100CF flanges and the attached UV viewports. The coil diameter and the mutual coil distance were $\phi=15\,\mathrm{cm}$ and $d=29\,\mathrm{cm}$, respectively, fixed by the outer dimensions of the vacuum chamber. With a typical current of $I=2\,\mathrm{A}$, a magnetic field of approximately 5 Gauss was generated in the trap center as measured with a Gaussmeter. This agrees well with the theoretical value of $B_0=2\,\mu_0 N I \phi^2/(\phi^2+d^2)^{3/2}$. It should be noted that the given coil diameter and mutual coil distance do not conform to the ideal case $\phi=2d$ with respect to homogeneity of the magnetic field. However, since the $^9Be^+$ ions were confined to a small region in the trap center with typical dimensions of $<2\,\mathrm{mm}$ ($\rightarrow$ Sect. 6.3), homogeneity of the magnetic field was not a critical issue. As indicated in Fig. 3.1, detection of the 313 nm fluorescence light emitted from the $^9Be^+$ ions was possible by using a photomultiplier tube (PMT) and/or a CCD camera, the first ensuring high sensitivity while the latter providing spatial resolution. In particular, the CCD camera was used to image the $^9Be^+$ ion crystals shown in chapters 6 and 7, as well as $^9Be^+$ plasmas in the cloud-like state. For both the PMT as well as the CCD camera, an UV lens/objective was mounted transverse to the trap axis, close to the trap electrodes ($\rightarrow$ Sect. 3.4). By this, a maximum amount of fluorescence light could be collected from the $^9Be^+$ ions. In addition, blackened baffles were used to block the residual 313 nm stray light from entering the PMT and the CCD camera. Finally, an all-metal leak valve (*Vacuum Generators*, type *ZVLM263R*) was connected to the vacuum chamber in order to allow a precise inlet of neutral gases such as H_2 , HD, D_2 and He.

3.2 Linear RF Trap

For the experiments described in chapters 5–7, a new linear rf trap was built by adopting the basic design from Refs. [1, 2], i.e. the segmenting and fixing of the electrode rods. Furthermore, an external excitation electrode was added to the linear rf trap in order to perform laser-cooled fluorescence mass spectrometry (LCF-MS) as will be described in chapter 5. Finally, a new Be oven was built. In the following, a description is given of the new linear rf trap setup, using the terminology which was introduced in Sect. 2.1.

The linear rf trap which is shown in Fig. 3.2 consists of four parallel electrode rods made of stainless steel (type 1.4404 / 316L), each with a diameter of $2r'=9.9\,\mathrm{mm}$ and a minimum distance to the trap axis of $r_0=4.32\,\mathrm{mm}$. This corresponds to a ratio of $r'/r_0=1.146$, close to the optimum value of 1.147 ($\rightarrow$ Sect. 2.1). Each electrode rod of total length 70 mm was divided into three electrically isolated segments, where the center electrode length was $L=16\,\mathrm{mm}$. By this choice, a harmonic dependence of the trap potential on the axial coordinate z was ensured for the region $-2.5 < z/\mathrm{mm} < +2.5$ (see below). This is large compared to the

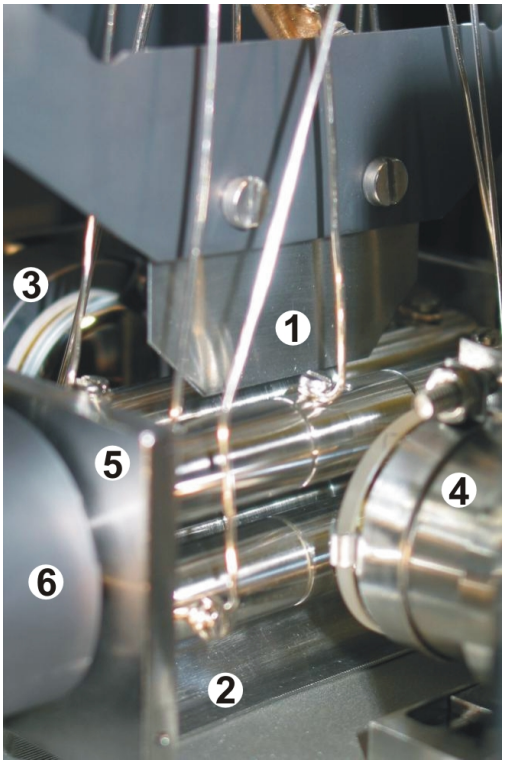

Figure 3.2: *Linear rf trap with external excitation electrode (1) and Be oven shielding (2). A single UV lens (3) and an UV objective (4) are mounted transverse to the trap axis. In the extension of the trap axis, a rectangular side plate (5) (→ Refs. [1,2]) and a part of a blackened baffle (6) can be seen.*

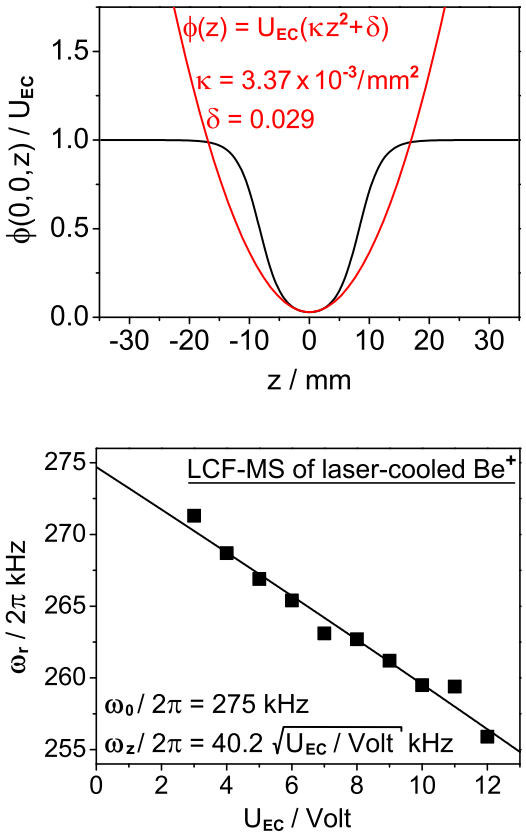

Figure 3.3: ***Top:*** *SIMION 6 simulation of the static potential along the trap axis.* ***Bottom:*** *Experimental determination of the axial trap frequency by performing LCF-MS on a small number of trapped $^9Be^+$ ions in a cloud-like state.*

typical axial dimensions of a $^9Be^+$ ion crystal [a] (→ Sect. 6.3). If used together with the new trap supply electronics, which will described in the next section, the rf frequency was fixed at $\Omega/2\pi = 14.2\,\mathrm{MHz}$. Typically, a rf amplitude of $U_{\mathrm{RF}} = 380\,\mathrm{V}$ and an endcap voltages of $U_{\mathrm{EC}} = 3\,\mathrm{V}$ were used in the experiments. In order to perform laser-cooled fluorescence mass spectrometry (LCF-MS), an external excitation electrode was mounted slightly above the upper electrode rods as can be seen in Fig. 3.2. Furthermore, a small Be oven was mounted below the linear rf trap, consisting of a beryllium wire of 50 μm diameter wrapped around a tungsten wire of 100 μm diameter. The latter was stretched between the two ends of a forked mount (two appropriately bent silver wires fixed in a Macor™ socket). By heating the tungsten wire with a typical current of 1 A, a sufficiently high flux of Be atoms was produced to allow for a complete trap loading within a typical time of 1 minute. In

[a] In the old linear rf trap described in Refs. [1,2], the center electrode length was $L = 40\,\mathrm{mm}$, giving rise to a box-shaped rather than a harmonic potential in axial direction. With this trap, no crystallization of the $^9Be^+$ plasma could be achieved.

order to prevent contamination of the trap electrodes with beryllium, a shielding was placed below the lower electrode rods, consisting of a stainless steel sheet with a small slit aperture along the trap axis.

Fig. 3.3 (top) shows a SIMION 6 simulation of the electrostatic potential $\phi_{\mathrm{trap}}(0,0,z)$ (black line) along the trap axis, assuming a voltage $U_{\mathrm{EC}} > 0$ applied to the endcap electrodes while keeping the center electrodes at ground. Accordingly, $\phi_{\mathrm{trap}}(0,0,z)$ is well approximated by a harmonic potential in the region $-2.5 < z/\mathrm{mm} < 2.5$. This can be seen from the fit of expression $\phi(z) = U_{\mathrm{EC}}(\kappa\, z^2 + \delta)$ (red line) at $z = 0$, yielding $\kappa = 3.37 \cdot 10^{-3}/\mathrm{mm}^2$ and $\delta = 0.029$. Since the parameter κ is identical to the geometric constant introduced in Sect. 2.1, axial trap frequencies of any given ion species may be calculated according to $\omega_z = [2\kappa\, Q U_{\mathrm{EC}}/m]^{1/2}$ [Eq. (2.3d)]. In particular, an axial trap frequency of $\omega_z/2\pi = 74.1\,\mathrm{kHz}$ is calculated for the $^9\mathrm{Be}^+$ ions, axially confined by an endcap voltage of $U_{\mathrm{EC}} = 3\,\mathrm{V}$. Alternatively, an experimental determination of the axial trap frequency is possible, employing LCF-MS as shown in Fig. 3.3 (bottom). In particular, the transverse trap frequency ω_r of a small number of trapped $^9\mathrm{Be}^+$ ions in a cloud-like state was measured by LCF-MS at different values of the endcap voltage $U_{\mathrm{EC}} = 3, 4, ..., 12\,\mathrm{V}$ ($\rightarrow$ Sect. 5.2). The linear rf trap was operated at a rf frequency of $\Omega/2\pi = 14.2\,\mathrm{MHz}$ and a rf amplitude of $U_{\mathrm{RF}} = 380\,\mathrm{V}$. A fit of expression $\omega_r = [\omega_0^2 - \omega_z^2(U_{\mathrm{EC}})/2]^{1/2}$ [Eqs.(2.3b) and (2.3c) with $U_{\mathrm{DC}} = 0$] and assuming $\omega_z^2(U_{\mathrm{EC}}) \propto U_{\mathrm{EC}}$ directly yields the transverse trap frequency $\omega_0/2\pi = 257\,\mathrm{kHz}$ in the limit $U_{\mathrm{EC}} \rightarrow 0$, and the axial trap frequency $\omega_z/2\pi = 40.2[U_{\mathrm{EC}}/\,\mathrm{V}]^{1/2}$ of the $^9\mathrm{Be}^+$ ions. The latter is equivalent to a geometric constant of $\kappa = 2.98 \cdot 10^{-3}/\mathrm{mm}^2$, in reasonable agreement with the theoretical value obtained by the SIMION 6 simulations.

Trap potential imperfections with respect to the ideal case, e.g., a transverse shift of the potential minimum relative to the trap axis, may result from contact potentials [84] due to an accidental coating of the trap electrodes with beryllium. However, even if preventing this, residual contaminations of the trap electrodes may cause significant trap potential imperfections as well. This was investigated in detail in Ref. [85] for a cylindrical Penning-type trap with electrodes made of stainless steel. Accordingly, even with careful cleaning of the electrode surfaces, potential variations of $\langle \Delta V \rangle_{\mathrm{rms}} \approx 250\,\mathrm{mV}$ with a characteristic length of 1 cm were measured at a distance of 1 mm from the electrode surfaces. In the same work, a strong reduction of the potential variations down to $\langle \Delta V \rangle_{\mathrm{rms}} \approx 15\,\mathrm{mV}$ was shown to be possible by coating the trap electrodes with a colloidal graphite. Thus, in case where a trap potential is required close to the ideal case, coating of the linear rf trap with a colloidal graphite like *Aquadag 18 %* (*Acheson Industries*) may be an option too.

3.3 Trap Supply Electronics

In Ref. [1], a description is given of the design and setup of a trap supply electronics, capable of driving both the old as well as the new linear rf trap with a maximum rf amplitudes of $U_{\mathrm{RF}} = 600\,\mathrm{V}$ at a fixed frequency of $\Omega/2\pi = 6.25\,\mathrm{MHz}$.

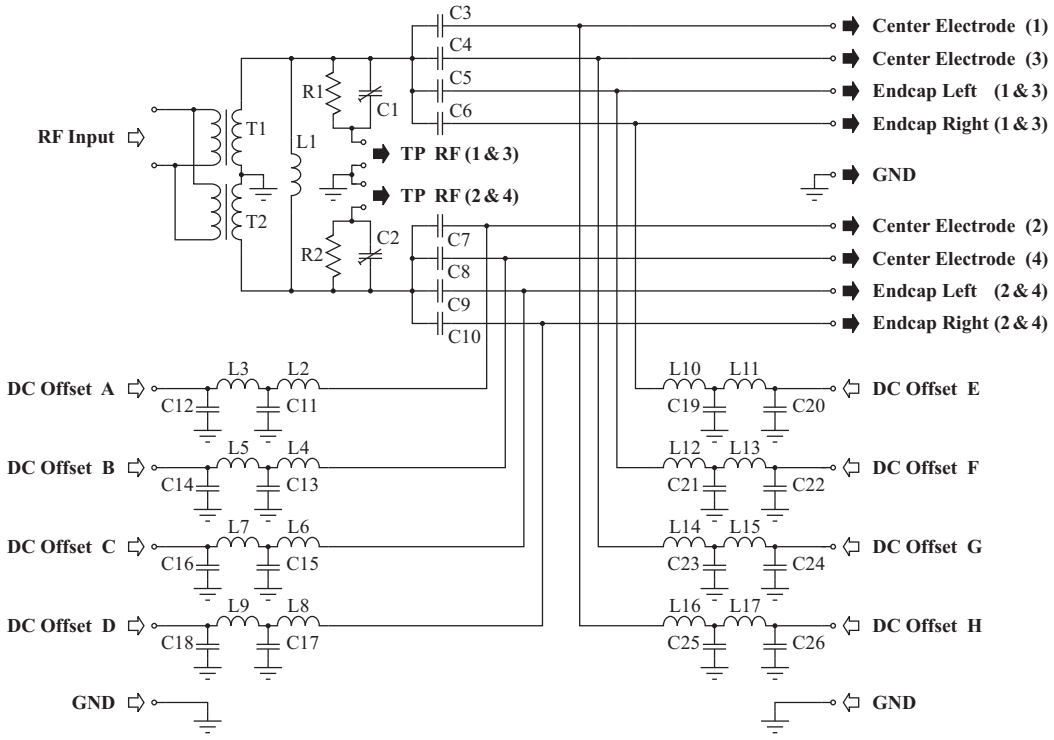

Figure 3.4: *Circuit diagram of the new trap supply electronics. Inputs are given by the rf voltage and the dc offset voltages A–H. In specifying the outputs, numbers 1–4 are used to label the electrode rods of the linear trap, where the pairs of numbers (1, 3) and (2, 4) each corresponds to a pair of opposing electrode rods.*

However, when this trap supply electronics was used in the UHV setup described in Sect. 3.1, charging of the trap electrodes was observed. This was caused by a combination of both the flood gun characteristics of the electron gun ($\rightarrow$ Sect. 3.1) and the high-impedance connections (1.5 MΩ each) of the trap electrodes to the dc voltage supplies. The latter was the price to be paid for a rather simple design of the trap supply electronics. Thus, development of a new trap supply electronics was required with the main goal of providing low-impedance connections between the trap electrodes and the dc voltage supplies. In addition, an increase in both rf frequency Ω and amplitude U_{RF} was aimed at as well, in order to allow simultaneous trapping of a large mass range. In particular, simultaneous trapping of both $^9\mathrm{Be}^+$ and H_2^+ should be made possible, with (i) the time-averaged potential description still valid, i.e. $q(\mathrm{Be}^+) < q(\mathrm{H}_2^+) < 0.3$, and (ii) a trap potential depth of at least a few eV, i.e. $\Psi(\mathrm{Be}^+) > \Psi(\mathrm{H}_2^+) > 3\,\mathrm{eV}$. Here, the trap potential depth is defined by $\Psi \stackrel{\mathrm{def}}{=} Q\phi_{\mathrm{trap}}(r = r_0)$ ($\rightarrow$ Sect. 2.1).

Fig. 3.4 shows the circuit diagram of the new trap supply electronics. The rf input is directly fed into a parallel connection of the two transformers T1 and T2, each consisting of a single primary and eleven secondary windings on a ferrite toroid core ($\mu_r = 125$, material type 61, see Ref. [86]). A LC resonator is formed by the series connection of the secondary sides of T1 and T2 together with the total capacitance of the trap electrodes. Silk wound hf litz wire is used for the secondary

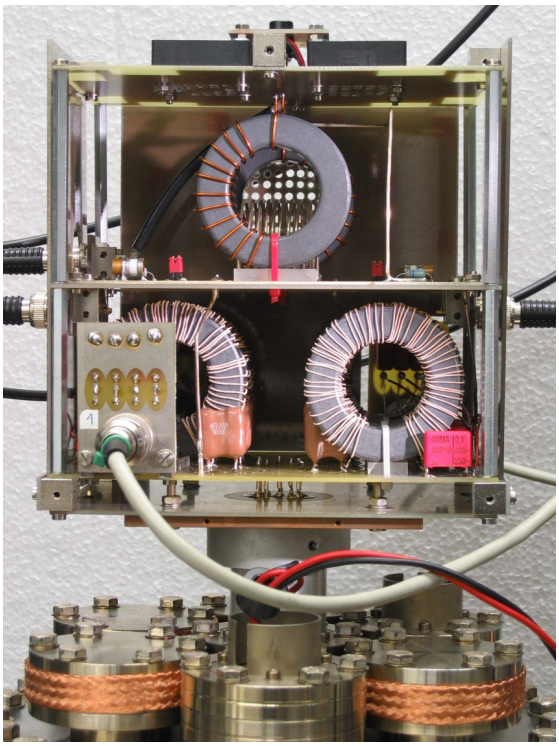

Figure 3.5: *Trap supply electronics with the front panel removed, mounted on top of the vacuum chamber. The transformers T1 and T2, and inductors L2, L4, ..., L16 are located on the upper and lower circuit board, respectively.*

windings of T1 and T2 in order to reduce both ohmic losses as well as stray capacitance between adjacent windings, thus ensuring a high quality-factor Q as well as avoiding a further increase in total capacitance C. In addition, a $3\,\mu$H air coil L1 is connected in parallel to the secondary sides of T1 and T2. By this, a decrease in total inductance L is achieved, resulting in a rf frequency of $\Omega/2\pi = 14.2\,$MHz (LC resonance) if the trap supply electronics is used together with the linear rf trap described in the previous section. Finally, by grounding the central connection between the secondary sides of T1 and T2, a symmetric distribution of the generated rf voltage $U_{\mathrm{RF}}\sin(\Omega\,t)$ on the two rf phases is guaranteed. Continuous monitoring of the two rf phases is possible by connecting an oscilloscope to the two test points TP RF (1&3) and TP RF (2&4): the two parallel connections R1||C1 and R2||C2, each consisting of a $33\,\mathrm{M}\Omega$ resistor and a variable $1.1-11\,$pF capacitor, are forming voltage dividers together with the respective oscilloscope input impedances $\mathrm{R_{CH\,1}}||\mathrm{C_{CH\,1}}$ and $\mathrm{R_{CH\,2}}||\mathrm{C_{CH\,2}}$. With the particular oscilloscope in use, and adjusting C1 and C2 such that $\mathrm{C1} \stackrel{!}{=} (\mathrm{R_{CH\,1}}/\mathrm{R1})\,\mathrm{C_{CH\,1}}$ and $\mathrm{C2} \stackrel{!}{=} (\mathrm{R_{CH\,2}}/\mathrm{R2})\,\mathrm{C_{CH\,2}}$, the voltage divider ratio was 1/38.

In the circuit diagram shown in Fig. 3.4, each rf phase is split into four branches, corresponding to a total number of $2\cdot 4 = 8$ dc offsets which can be added to the rf voltage $U_{\mathrm{RF}}\sin(\Omega\,t)$. Mutual blocking between the dc offsets is ensured by the capacitors C3–C10, each realized by a 22 nF mica capacitor with low dielectric losses.

Furthermore, by the series connections of two second order LC low-pass filters built from inductors L2–L17 and capacitors C11–C26, the rf voltages $U_{\mathrm{RF}} \sin(\Omega\, t)$ is blocked from the dc offset inputs as well. In order to keep the ohmic losses and stray capacitance low, inductors L2, L4, ..., L16 are realized by 65 turns of hf litz wire on a ferrite toroid core ($\mu_r = 125$, material type 61, see Ref. [86]). The resulting inductances are approximately $600\,\mu$H. Capacitors C11, C13, ..., C25 are 100 nF capacitors (*WIMA*, type *MKP*). Due to the circuit design, low-impedance connections of typically $10.3\,\Omega$ (dc) are provided between the dc offset inputs A–H and the trap electrodes. In Fig. 3.4, numbers 1–4 are used to label the four electrode rods of the linear rf trap, where the pairs of numbers (1,3) and (2,4) each corresponds to a pair of opposing electrode rods. Thus, the four dc offsets A, B, G, and H can be applied to the four center electrodes individually, while the remaining four offsets F, C, D, and E are left for the eight endcap electrodes, matching all experimental needs in this work.

In the experiments described in chapters 5–7, a self-built rf sine wave generator followed by a 15 W power amplifier (*Amplifier Research*) was connected to the rf input of the new trap supply electronics. Due to the low losses (high quality-factor Q) occurring in the LC resonator, a maximum rf amplitudes of $U_{\mathrm{RF}} > 1000\,\mathrm{V}$ could be achieved at $\Omega/2\pi = 14.2\,\mathrm{MHz}$ [a]. This has to be compared with a maximum rf amplitude of 600 V at 6.25 MHz which could be achieved with the old trap supply electronics, when connected to the same rf power amplifier. The increase in rf amplitude is remarkable in so far as the increase in rf frequency required a reduction of the total number of windings on the secondary sides of T1 and T2 from 170 [1] to $2 \cdot 11 = 22$. Finally, in order to minimize electronic noise, all dc voltage sources (inputs A–H) were realized using rechargeable batteries. Fig. 3.5 shows the complete trap supply electronics in a shielded housing, mounted directly on an electric feedthrough on top of the vacuum chamber, thus minimizing capacitances associated with cable length.

3.4 Photomultiplier Tube and CCD Camera

As already indicated in the schematic overview Fig. 3.1, detection of the 313 nm fluorescence light emitted from the laser-cooled $^9\mathrm{Be}^+$ ions was possible by using a photomultiplier tube (PMT) and/or a CCD camera, the first ensuring high sensitivity while the latter providing spatial resolution. From a first (failed) attempt at fluorescence detection with the old experimental setup described in Refs. [1,2], the importance of two measures was recognized: (i) maximum care in reducing the level of 313 nm stray light within the vacuum chamber, and (ii) collection of a maximum amount of fluorescence light from the $^9\mathrm{Be}^+$ ions by placing an UV lens/objective

[a] As a further characteristic, the input impedance of the new trap supply electronics was measured at $\Omega/2\pi = 14.2\,\mathrm{MHz}$, yielding $|Z| = 100 - 250\,\Omega$ ($\arg\{Z\} \approx +15^\circ$) which is not far from the $50\,\Omega$ output impedance of the 15 W rf power amplifier. Thus, improved impedance matching could be a reason too for the achieved gain in rf amplitude U_{RF}.

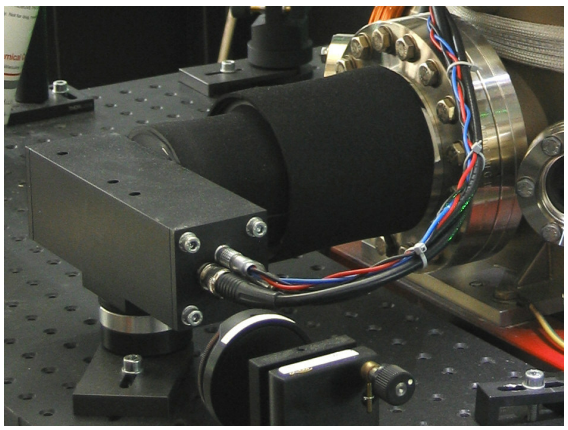

Figure 3.6: *Light-proof aluminum housing for the photomultiplier tube (PMT), connected to a vacuum chamber viewport via a removable optics mount. A black rubber mat is wrapped around the optics mount.*

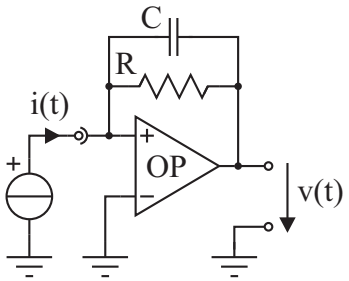

Figure 3.7: *Equivalent circuit of the photomultiplier tube (PMT) and the self-built preamplifier. The PMT is treated as an ideal current source (see text).*

close to the linear rf trap (→ Fig. 3.2). Measure (i) also includes the spatial filtering of the 313 nm cooling laser light as will be described in Sect. 4.1. In this section, a brief description is given of both the photomultiplier tube (PMT) and the CCD camera optical setup.

In case of detection with the photomultiplier tube (PMT), a single UV lens was used to collect the 313 nm fluorescence light from the $^9Be^+$ ions. In particular, a lens with diameter $\phi = 25.4$ mm and a focal length $f = 35$ mm was mounted at a distance $d = f$ from the trap center (→ Fig. 3.2). The lens was fitted into a blackened baffle, made of a stainless steel sheet which was bent into appropriate shape and coated with a colloidal graphite (*Acheson Industries*, type *Aquadag 18 %*). By this, residual 313 nm stray light scattered from the trap electrodes was prevented from reaching the PMT. After being collected by the UV lens and transmitted through an UV view port (*Caburn-MDC*, type *DUV-200*), the fluorescence light was focused through an adjustable slit and sent through a 313 nm interference filter (*Melles Griot*). Finally, the fluorescence light was detected by the photomultiplier tube (*Hamamatsu*, type *R1527P*). By properly adjusting the size of the adjustable slit, a further reduction of the 313 nm stray light could be achieved. The PMT was enclosed by a light-proof aluminum housing as shown in Fig. 3.6, which also contained a magnetic shielding (*Hamamatsu*, type *E989*), a PMT socket with an integrated voltage divider (*Hamamatsu*, type *E717*), and a self-built preamplifier. A rather old but still working photon counting unit (*Hamamatsu*, type *C1230*) was used to perform single photon counting. In particular, each detected photon typically gave rise to a 4 – 5 ns [87] *current* pulse at the PMT output. On the other hand, the photon counting unit was expecting *voltage* pulses with an optimum width of 30 ns. Thus, a self-built preamplifier was designed to match both the PMT output and the photon counting unit input. Fig. 3.7 shows the equivalent circuit of the PMT and the self-built preamplifier, where the latter was built from

an operational amplifier (*Analog Devices*, type *AD9631*), a resistor $R = 10\,\mathrm{k\Omega}$, and a capacitor $C = 6.8\,\mathrm{pF}$. Accordingly, each current pulse $i(t)$ with a total charge $Q_p = \int dt\, i(t)$ was converted into a voltage pulse with an approximate width and height of $RC = 70\,\mathrm{ns}$ and $-Q_p/C = 160\,\mathrm{mV}$, respectively [a]. Here, a typical charge of $Q_p = -1.1\,\mathrm{pC}$ [87] is assumed. Due to careful reduction of 313 nm stray light by use of the blackened baffles, adjustable slit aperture, and by spatial filtering of the cooling laser light (→ Sect. 4.1), a strong decrease of the background photon count rate could be achieved. In particular, a typical background photon count rate of 8 KCPS (kilo-counts per second) was measured at a laser power of $P_{313} = 1\,\mathrm{mW}$ [b]. Clipping of the photon count rate was observed at approximately 1400 KCPS, presumably caused by a baseline shift at the output of the self-built preamplifier, due to the rapid succession of voltage pulses. Finally, the overall detection efficiency ϵ of the PMT setup can be estimated from the solid angle $S \approx \pi(0.5 \cdot 25.4/35)^2$ covered by the UV lens, the transmission $T \approx 10\,\%$ of the 313 nm interference filter, and the quantum efficiency $\mathrm{QE} \approx 10\,\%$ [87] of the PMT: $\epsilon \approx (S/4\pi) \cdot T \cdot \mathrm{QE} = 3.3 \cdot 10^{-4}$.

For imaging of the $^9Be^+$ ion crystals with the CCD camera, an UV objective (*Special Optics*, type *54-17-29*, $f = 30.9\,\mathrm{mm}$, modified for use in UHV) was placed close to the linear rf trap (→ Fig. 3.2). A protective window (fused silica, UV-AR coated) was put in front of the UV objective in order to prevent it from accidental coating with beryllium from the Be oven. As in case of the single UV lens, collecting fluorescence light for the PMT, a blackened baffle was used to block 313 nm stray light from reaching the CCD camera. After passing through an UV viewport (*Caburn-MDC*, type *DUV-200*) and an UV broadband filter (*Schott*, type *DUG 11 X*), the fluorescence light was focused onto the CCD chip of the camera (*PCO*, type *Sensicam*) by a second UV objective (*Special Optics*, type *54-17-29*, $f = 30.9\,\mathrm{mm}$). Slight adjustment of the resulting lateral magnification was possible by moving the CCD camera onto the optical table by a few centimeter. Usually, the lateral magnification was 3.0 – 3.5, determined by placing an object of known size in the trap center and illuminating it with 313 nm laser light. Alternatively, the lateral magnification could be determined by use of molecular dynamics (MD) simulations, reproducing the structure of the $^9Be^+$ ion crystals in the CCD images.

[a] Since the current pulse width is small compared to the time constant RC, the current pulse can be approximated by $i(t) = Q_p \delta(t)$, where $\delta(t)$ is the Dirac delta function (unit s^{-1}). Thus, the generated voltage pulse is given by $v(t) = -(Q_p/C)\, u(t)\, e^{-t/RC}$, where $u(t)$ is the unit step-function.

[b] This has to be compared with a background count rate of far more than 1000 KCPS in case where no measures were taken.

Chapter 4

Cooling Laser System

In this chapter, the cooling laser system will be described which was used for laser cooling of the $^9Be^+$ ions. Starting with an overview of the complete laser system in **Sect. 4.1**, doubly resonant sum-frequency generation (DR-SFG) of 313 nm light will be described in **Sect. 4.2**. In particular, a brief review will be given in **Sect. 4.2.1** of the theoretical results from Refs. [1,2]. This is followed by a description of the experimental DR-SFG setup, including the optical enhancement cavity and the nonlinear crystal (**Sect. 4.2.2**), as well as the two fundamental lasers and the DR-SFG stabilization scheme (**Sect. 4.2.3**). Since the DR-SFG setup is based on a previous version, described in detail in Refs. [1,2], the focus will be on major modifications with respect to Refs. [1,2]. In particular, two new fundamental lasers and a further optimized nonlinear crystal were added. Sect. 4.2 will be completed by an experimental characterization of the DR-SFG setup with respect to output power, tunability and spectral purity (**Sect. 4.2.4**). An absolute frequency stabilization of the 313 nm cooling laser light will be described in **Sect. 4.3**, based on an I_2 frequency standard for the 532 nm fundamental laser which will be described in **Sect. 4.3.1**. In addition, an optical frequency shifter at 532 nm wavelength will be described in **Sect. 4.3.2**, which was used for frequency fine-adjustment of the absolutely frequency-stabilized 313 nm laser light.

In order to formulate the requirements on the cooling laser system, some data concerning laser cooling of $^9Be^+$ ions at 313 nm wavelength shall be summarized here. Doppler laser cooling of $^9Be^+$ ions in a rf (Paul) trap is preferably done by using σ^+ polarization of the cooling laser light which is directed along a quantization axis, defined by a weak magnetic field ($\rightarrow$ Sect. 3.1). Accordingly, if excited at a wavelength of $\lambda = 313.1327\,\text{nm}$, the $^9Be^+$ ions are expected to exclusively cycle between the $^2S_{1/2}(F=2, m_F=2)$ ground and the $^2P_{3/2}(F=3, m_F=3)$ excited state with a natural linewidth of $\gamma/2\pi = 19.4\,\text{MHz}$ (FWHM) and a saturation intensity of $I_{\text{sat}} = 0.83\,\text{mW/mm}^2$ [88]. However, due to imperfect σ^+ polarization, decay of the excited $^9Be^+$ ions into the $F = 1$ ground state will also take place, thus requiring additional "repumping" laser light. In particular, laser light red-detuned by $-1.25\,\text{GHz}$ and with an intensity of a few percent as compared to that of the

"main" cooling laser light is needed. Furthermore, if producing the $^9Be^+$ ions by electron impact ionization of thermally evaporated Be atoms, an initial temperature of the $^9Be^+$ ions of more than 1000 K should be expected. This corresponds to a Doppler width of approximately 7 GHz (FWHM) for the $^2S_{1/2}(F = 2, m_F = 2) \leftrightarrow {}^2P_{3/2}(F = 3, m_F = 3)$ cooling transition. Thus, continuous tuning of the 313 nm cooling laser light over a complete red wing of the Doppler broadened line is required for effective cooling of the $^9Be^+$ ions.

4.1 Overview of the Complete Setup

Fig. 4.1 shows a schematic of the complete cooling laser system. Laser light at 313 nm wavelength is generated by doubly resonant sum-frequency generation (DR-SFG) between two fundamental lasers: a resonantly frequency-doubled monolithic Nd:YAG laser (*InnoLight*, type *Diabolo 1000 DW*), emitting up to 1 W at 532 nm wavelength, and a Ti:sapphire laser (*Coherent*, type *MBR-110*), emitting up to 1.5 W at 760 nm wavelength. The 532 nm light delivered by the frequency-doubled Nd:YAG laser first passes through a pair of cylindrical lenses and a 30 dB Faraday isolator (*Linos Photonics*), in order to correct for astigmatism and to protect the laser from retroreflected light, respectively. Next, a power of typically 40 mW is split off from the 532 nm laser light and sent to an optical frequency shifter (→ Sect. 4.3.2) which then is followed by an I_2 frequency standard. The latter is realized by Doppler-free modulation transfer spectroscopy (MTS) of molecular iodine (→ Sect. 4.3.1). In Fig. 4.1, a dashed line is pointing from the I_2 frequency standard back to the Nd:YAG laser. This indicates an electronic feedback loop which stabilizes the frequency of the Nd:YAG laser with respect to the I_2 frequency standard. Thus, absolutely frequency stabilized 532 nm laser light, tunable by up to 200 MHz, is finally sent to the DR-SFG setup. In contrast to this, no further frequency stabilization is needed for the 760 nm laser light, due to the employed DR-SFG stabilization scheme (see below). After being emitted from the Ti:sapphire laser and sent through a two-stage 60 dB Faraday isolator (*Linos Photonics*), a typical power of 1 mW is split off from the 760 nm laser light and coupled into a wavemeter (*Burleigh*, type *WA-1500*). By this, precise adjustment of the frequency of the Ti:sapphire laser is possible. Due to the optical components (in particular the Faraday isolators) placed between the two fundamental lasers and the setup for DR-SFG, only about 74% and 66% of the initial laser powers at 532 and 760 nm wavelength, respectively, are finally available for DR-SFG. The DR-SFG setup is built on a separate optical breadboard, including a bow-tie shaped ring cavity and a nonlinear crystal (→ Sect. 4.2.2), as well as a set of lenses, mirrors, and waveplates for polarization adjustment and mode matching of the two fundamental waves (→ Sect. 4.2.4). Furthermore, two electronic feedback loops are employed for DR-SFG, where the first one is locking the optical cavity to the 532 nm laser light by adjusting the cavity length, while the second one is locking the 760 nm laser light to the cavity (→ Sect. 4.2.3). Due to this stabilization scheme, the frequency of the generated light at 313 nm wavelength is essentially controlled by the frequency of the 532 nm laser light which in turn is stabilized on the I_2 frequency standard. After leaving the DR-SFG setup, the 313 nm light is first corrected for astigmatism by a

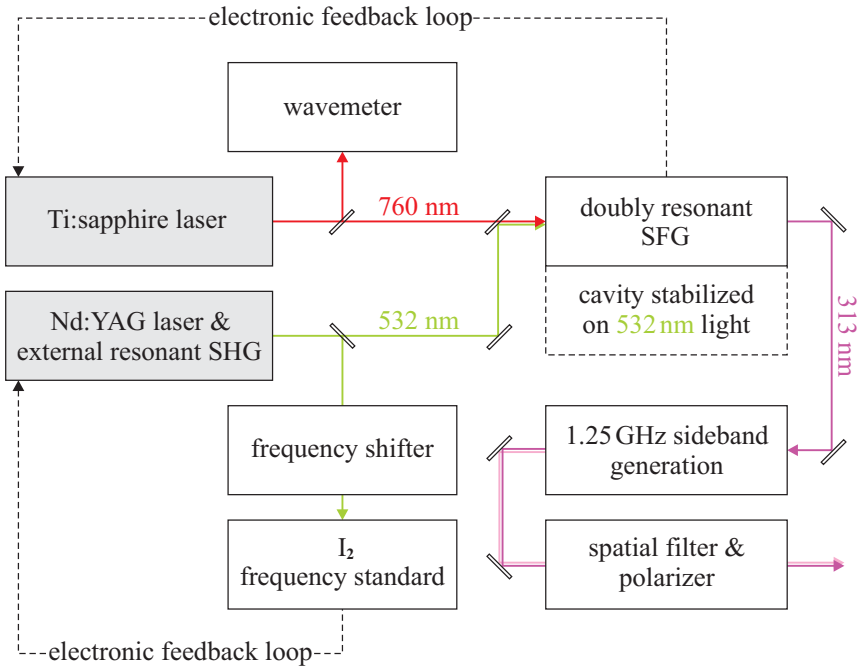

Figure 4.1: *Schematic of the complete laser system used for laser cooling of the $^9Be^+$ ions at 313 nm wavelength. Solid and dashed lines indicate schematic paths of the laser beams and the electronic feedback loops, respectively.*

pair of cylindrical lenses. Next, generation of 1.25 GHz sidebands is performed with an electro-optical modulator (EOM), custom fabricated by *Leysop Ltd*, a detailed description of which is found in Ref. [1]. Spatial filtering by focusing the 313 nm light through a $\phi = 15\,\mu$m pinhole ensures a minimum level of residual stray light in the vacuum chamber. By adjusting the position of a plano-convex lens ($f = 40$ mm), placed behind the pinhole, a typical beam waist of $w_0 = 500 - 800\,\mu$m is obtained in the trap center ($\rightarrow$ Sect. 3.1). Finally, a Glan-Taylor prism (*ELAN Ltd.*) together with a quarter-wave ($\lambda/4$) plate is used to provide the σ^+ circular polarization. The Glan-Taylor prism is characterized by a high degree of polarization purity. Furthermore, since both prism parts are connected via an air gap rather than a cement layer, optical damage is avoided which occurred in the polarizing beam splitter (PBS) previously used. The complete cooling laser system is protected from dust by an acrylic glass enclosure, ventilated with clean filtered air.

4.2 Doubly Resonant SFG of 313 nm Light

As can be seen from Fig. 4.1, doubly resonant sum-frequency generation (DR-SFG) of 313 nm laser light is realized by choosing an all-solid state approach. A major advantage with this approach is that no significant amount of maintenance is required compared to, e.g., the use of a dye laser. Furthermore, by replacing the Ti:sapphire laser with a diode laser, an alternative setup of comparatively low costs is possible as was demonstrated in Refs. [1,2]. In contrast to this, the traditional

approach to the generation of 313 nm laser light would be a single-frequency dye laser, resonantly frequency-doubled to the UV [89]. Laser cooling of $^9Be^+$ ions with the latter approach is described in Refs. [90,91].

From the brief review of Doppler laser cooling of $^9Be^+$ ions in a rf (Paul) trap, given at the beginning of this chapter, the requirements

R1:	output power	$\geq 10\,\mathrm{mW}$
R2:	spectral linewidth	$\leq 1\,\mathrm{MHz}$
R3:	tunability	$\geq 10\,\mathrm{GHz}$

can be deduced for the 313 nm laser light, ensuring convenient experimental work. In specifying **R1**, a beam waist of $w_0 = 500 - 800\,\mu\mathrm{m}$ was assumed and losses were taken into account, occurring in the optical components between the DR-SFG setup and the linear rf trap (→ Sect. 4.1). In addition to **R1**–**R3**, long-term frequency stability is required as well. This will be discussed in Sect. 4.3.

4.2.1 Theory of DR-SFG

In Refs. [1, 2], the theory of DR-SFG with Gaussian beams is developed in detail, with the main goal of optimizing DR-SFG with respect to output power. Alternatively, a theory of DR-SFG is found in Ref. [92] as well. In this section, a brief review will be given of the theoretical results from Refs. [1,2], as far as relevant to the interpretation of the experimental data which will be presented in Sect. 4.2.4.

Sum-frequency generation (SFG) relies on the parametric interaction in a nonlinear medium of two fundamental waves with frequencies ω_1 and ω_2, respectively. Accordingly, both frequencies ω_1 and ω_2 as well as the sum-frequency $\omega_3 = \omega_1 + \omega_2$ are far off any resonance of the nonlinear medium which therefore acts purely reactive. As a realistic approximation, Gaussian TEM_{00} modes are considered in the two fundamental waves, assuming identical Rayleigh ranges $z_{R1} = z_{R2}$ and identical locations of foci in the center of the nonlinear crystal. Furthermore, identical polarization of the two fundamental waves along a crystal axis (type I interaction), negligible depletion due to frequency conversion, and good phase matching are assumed as well (→ Sect. 4.2.2). In this case, a Gaussian TEM_{00} mode at sum-frequency $\omega_3 = \omega_1 + \omega_2$ is expected to be generated with power

$$P_3 \;=\; E_{\mathrm{NL}}^{\mathrm{SFG}}\, P_1^{\mathrm{circ}}\, P_2^{\mathrm{circ}} \qquad \text{, where} \qquad E_{\mathrm{NL}}^{\mathrm{SFG}} \;\stackrel{\mathrm{def}}{=}\; 4 \cdot \frac{\mu_0 d^2}{\pi c^2}\, \frac{\omega_2\, \omega_2\, \omega_3}{n_3^2} \cdot h \cdot L\,. \tag{4.1}$$

In Eq. (4.1), P_1^{circ} and P_2^{circ} are the powers of the two incoming fundamental waves at frequencies ω_1 and ω_2, respectively, and $E_{\mathrm{NL}}^{\mathrm{SFG}}$ is the effective nonlinearity of sum-frequency generation. Adding the superscript "circ" to P_1 and P_2 already indicates

a placement of the nonlinear crystal inside an optical enhancement cavity. This will be further described below. In calculating the effective nonlinearity $E_{\mathrm{NL}}^{\mathrm{SFG}}$, the parameters characterizing the nonlinear crystal are: the crystal length L, the index of refraction n_3 at frequency ω_3, and the second-order effective nonlinear optical susceptibility d [1,2]. Phase matching as well as the overlap between the Gaussian TEM_{00} modes in the two fundamental waves are included in the Boyd-Kleinman factor h, defined analogous to the one known from the theory of second harmonic generation (SHG) [93]. In Eq. (4.1), $c = 2.998 \cdot 10^8\,\mathrm{m/s}$ and $\mu_0 = 1.256 \cdot 10^{-6}\,\mathrm{N/A^2}$ are the vacuum speed of light and the vacuum permeability, respectively.

In doubly resonant sum-frequency generation (DR-SFG), resonant enhancement of the two fundamental waves is employed to increase the power P_3 [Eq. (4.1)] of the generated wave. To this end, the nonlinear crystal is placed inside an optical enhancement cavity, where the cavity resonance condition has to be fulfilled simultaneously for both fundamental waves (→ Sect. 4.2.3). The *circulating* powers P_1^{circ} and P_2^{circ} of the two fundamental waves at frequencies ω_1 and ω_2, respectively, can be calculated from the two coupled equations

$$\sqrt{\frac{T_1\,P_1^{\mathrm{in}}}{P_1^{\mathrm{circ}}}} \;=\; 1 - \sqrt{(1-T_1)(1-S_1)\Big(1 -\; E_{\mathrm{NL}}^{\mathrm{SFG}} \cdot \frac{\omega_2}{\omega_3} \cdot P_2^{\mathrm{circ}}\Big)} \tag{4.2a}$$

$$\sqrt{\frac{T_2\,P_2^{\mathrm{in}}}{P_2^{\mathrm{circ}}}} \;=\; 1 - \sqrt{(1-T_2)(1-S_2)\Big(1 -\; E_{\mathrm{NL}}^{\mathrm{SFG}} \cdot \frac{\omega_2}{\omega_3} \cdot P_1^{\mathrm{circ}}\Big)}\,, \tag{4.2b}$$

where P_1^{in} and P_2^{in} are the input powers of the two fundamental waves in the respective Gaussian TEM_{00} cavity modes. Thus, in order to determine P_1^{in} and P_2^{in} correctly, input powers measured in front of the optical enhancement cavity have to be corrected by the corresponding factors quantifying mode matching. This will be described in Sect. 4.2.4. In Eqs. (4.2a) and (4.2b), the parameters characterizing the optical enhancement cavity are: the transmissions T_1 and T_2 of the incoupling mirror, and the sums S_1 and S_2 of all passive losses (except from those occurring at the incoupling mirror) at frequencies ω_1 and ω_2, respectively. Coupling of Eqs. (4.2a) and (4.2b) is due to the last terms below the square roots on the right-hand sides. These terms account for the losses due to conversion of the fundamental waves into the generated wave at sum-frequency $\omega_3 = \omega_1 + \omega_2$.

According to Eqs. (4.2a) and (4.2b), a maximum output power $P_3 \propto P_1^{\mathrm{circ}}\,P_2^{\mathrm{circ}}$ [Eq. (4.1)] is obtained by minimizing the passive losses S_1 and S_2, and by choosing optimum incoupling transmissions T_1 and T_2 for given values of P_1^{in}, P_2^{in}, S_1, S_2, and $E_{\mathrm{NL}}^{\mathrm{SFG}}$. A plot of the output power P_3 as a function of the two incoupling transmissions T_1 and T_2 is possible by repeated numerical solution of Eqs. (4.2a) and (4.2b). This was done in Refs. [1,2] in order to determine the optimum incoupling transmissions T_1^{opt} and T_2^{opt}. Alternatively, T_1^{opt} and T_2^{opt} can be stated explicitly

in the case of small passive losses $S_{1,2} \ll 1$ and small conversion losses $E_{\mathrm{NL}}^{\mathrm{SFG}} P_{1,2}^{\mathrm{circ}} \ll 1$ when the square roots on the right-hand sides of Eqs. (4.2a) and (4.2b) can be approximated. In this case,

$$T_1^{\mathrm{opt}}/S_1 = \frac{1}{2}\left(1 - \epsilon_1 + \epsilon_2 + \sqrt{(1+\epsilon_1+\epsilon_2)^2 - 4\epsilon_1\epsilon_2}\ \right) \tag{4.3a}$$

$$T_2^{\mathrm{opt}}/S_2 = \frac{1}{2}\left(1 + \epsilon_1 - \epsilon_2 + \sqrt{(1+\epsilon_1+\epsilon_2)^2 - 4\epsilon_1\epsilon_2}\ \right), \tag{4.3b}$$

where the normalized input powers are defined as $\epsilon_1 \stackrel{\mathrm{def}}{=} (\omega_2/\omega_3) E_{\mathrm{NL}}^{\mathrm{SFG}} P_1^{\mathrm{in}}/S_1 S_2$ and $\epsilon_2 \stackrel{\mathrm{def}}{=} (\omega_1/\omega_3) E_{\mathrm{NL}}^{\mathrm{SFG}} P_2^{\mathrm{in}}/S_1 S_2$.

4.2.2 Nonlinear Crystal and Optical Cavity

The high output power (→ Sect. 4.2.4) which was achieved with the DR-SFG setup, results from the careful design of the optical enhancement cavity as well as the choice of the nonlinear crystal. This is described in detail in Refs. [1,2]. However, while the optical cavity is still unchanged, a new nonlinear crystal was used in the experiments described in chapters 5–7 of this work, leading to a significant increase in output power. This will be described in Sect. 4.2.4. In the present section, a brief review and update will be given on the optical cavity and the nonlinear crystal. Corresponding to the three wavelengths involved, the indices $i = 1, 2$, and 3 of the previous section will be replaced by the more specific indices $i = 532, 760$, and 313, respectively.

The optical enhancement cavity, doubly resonant for both fundamental waves, is realized by four mirrors M1–M4, directing light along a bow-tie shaped path [1, 2]. In particular, mirror M1 is used as an incoupling mirror for the two fundamental waves with transmissions of $T_{532} = 1.85\,\%$ and $T_{760} = 2.67\,\%$ at 532 and 760 nm wavelength, respectively. Mirror M4 is used as an outcoupling mirror for the generated wave at 313 nm wavelength. Accordingly, mirrors M2–M4 are provided with a highly reflective (HR) coating for 532 nm and 760 nm wavelength, and an antireflective (AR) coating for 313 nm wavelength. Furthermore, mirrors M1 and M2 are planar, while mirrors M3 and M4 are concave ($f = 50$ mm) in order to focus the two fundamental waves into the nonlinear crystal which is placed between them. Calculation of the Gaussian TEM_{00} cavity modes at 532 and 760 nm wavelength yields beam waists of $w_{0\,532} \approx 41\,\mu$m and $w_{0\,760} \approx 49\,\mu$m, respectively, located in the crystal center [1,2]. Slightly different values are obtained for the tangential and sagittal planes due to a small astigmatism of a few percent. As will be further discussed below, these beam waists are not the optimum with respect to output power of the generated 313 nm wave. Rather they are the result of a stability analysis, described in Refs. [1,2]. The cavity total round-trip length is $U = 483$ mm and can be fine-adjusted by a piezoelectric actuator driving mirror M2. The cavity free spectral range is $\mathrm{FSR} = c/U = 620$ MHz, where $c = 2.998 \cdot 10^8$ m/s is the vacuum speed of light.

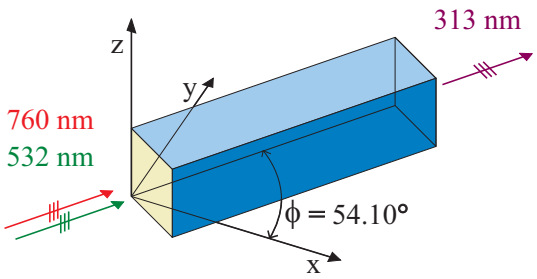

Figure 4.2: *LBO crystal, cut for critical phase matching. Polarizations of the 532 and 760 nm fundamental waves and the 313 nm generated wave are indicated.*

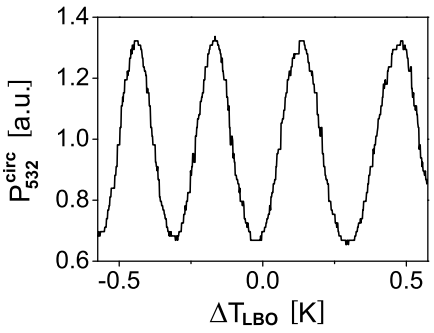

Figure 4.3: *Measured periodic variation of the resonated power P_{532}^{circ} with crystal length $L \propto T_{LBO}$, caused by residual reflections at the crystal end faces.*

Criteria such as high nonlinearity, low absorption losses, and the possibility to achieve phase matching have led to the choice of lithium triborate LiB_3O_5 (LBO) for the nonlinear crystal. In particular, phase matching $\Delta k = 0$ is achieved by taking advantage of the birefringence property of LBO, where $\Delta k \stackrel{\text{def}}{=} k_{313} - k_{532} - k_{760}$ with wavenumbers $k_i = 2\pi n_i/\lambda_i$ and $i \in \{532, 760, 313\}$. Even though LBO is a biaxial crystal with two optical axes, the situation is rather simple for an optical wave propagating in the principal plane (X,Y), defined by the crystal X and Y axis, as indicated in Fig. 4.2: if polarized perpendicular to (X,Y), the wave will experience a constant index of refraction n_o. On the other hand, if polarized parallel to (X,Y), the wave will experience a variable index of refraction $n_e(\phi)$. Here, ϕ is defined as the angle between the direction of propagation of the optical wave and the crystal X axis [a]. Thus, phase matching can be achieved by adjusting the angle ϕ, i.e. by cutting the crystal appropriately (critical phase matching). In particular, $\phi = 54.10°$ for the three wavelengths 532, 760, and 313 nm, where the two fundamental waves are polarized perpendicular to (X,Y), while the generated 313 nm wave is polarized parallel to (X,Y) (ooe type I interaction). The corresponding second-order nonlinear susceptibility is $d \approx 0.5 \cdot 10^{-12}$ m/V [1,2] and the index of refraction at 313 nm wavelength is $n_e(54.10°, 313\,\text{nm}) = 1.6177$. Thus, according to Eq. (4.1), the resulting effective nonlinearity of sum-frequency generation is

$$E_{\text{NL}}^{\text{SFG}} = \frac{0.092}{\text{m W}} \cdot h \cdot L \ , \tag{4.4}$$

where h and L are the Boyed-Kleinman factor and the crystal length, respectively. In particular, a length of $L = 15$ mm was chosen for the LBO crystal, where a further increase would be of no use due to the walk off between the two fundamental waves and the generated 313 nm wave [1,2]. A theoretical maximum of $h = 1.07$ [93] could

[a] By using symbols n_o and $n_e(\phi)$, the analogy to the case of an uniaxial crystal is emphasized which usually is described by an ordinary (o) and an extraordinary (e) index of refraction.

be reached for the Boyed-Kleinman factor in case of a small phase mismatch $\Delta k \neq 0$ and with the optimum Rayleigh ranges $z_{R532} = z_{R760} = L/5.7$. However, the latter would imply beam waists of $w_{0532} \approx 17\,\mu$m and $w_{0760} \approx 20\,\mu$m in the crystal center at 532 and 760 nm wavelength, respectively. This follows directly from the definition of the Rayleigh range $z_{Ri} \stackrel{\text{def}}{=} \pi w_{0i}^2 n_i/\lambda_i$, where $i \in \{532, 760\}$. Thus, while a small phase mismatch $\Delta k \neq 0$ is easily achieved by slightly tilting the LBO crystal with respect to the optical cavity, fulfillment of the second condition $z_{R532} = z_{R760} = L/5.7$ would imply a deviation from the optimum with respect to stability [1,2].

A first LBO crystal which was used in the previous version of the DR-SFG setup [1,2], was ordered from *Photox* and triple AR-coated by *Dünnschicht-Technik Tafelmeier*. The residual reflectivities of the crystal end faces were measured as $R_{532} \approx 0.8\%$ and $R_{760} \approx 0.1\%$ at 532 and 760 nm wavelength, respectively. A strong periodic variation of the output power at 313 nm wavelength was observed when scanning the optical enhancement cavity ($\rightarrow$ Sect. 4.2.3). This could be explained by multiple reflections of the 532 nm laser light between the parallel end faces of the LBO crystal which, like in an etalon, resulted in a periodic dependence of the crystal transmission on optical wavelength. Fig. 4.3 shows the measured power P_{532}^{circ} circulating inside the optical cavity which is locked to the 532 nm laser light, while changing the temperature of the LBO crystal. With the resulting change in crystal length, any etalon-like effect is expected to show up as a change in circulating power P_{532}^{circ}, due to the change in crystal transmission. Indeed, a strong periodic variation of P_{532}^{circ} is observed in Fig. 4.3 [b]. A new LBO crystal was ordered from *Photox*, however with the end faces sloped by ± 30 arc minutes with respect to each other. In addition, a further optimization of the AR-coating could be achieved by *Dünnschicht-Technik Tafelmeier*. In particular, the residual reflectivities of the crystal end faces at 532 nm wavelength could be decreased to $R_{532} < 0.2\%$ while leaving R_{760} unchanged. After replacement of the old LBO crystal by the new one, no periodic variation in output power at 313 nm wavelength was observed anymore when scanning the optical cavity.

4.2.3 Fundamental Lasers and Stabilization Scheme

In DR-SFG, active stabilization of either the fundamental laser frequencies or the optical cavity length is required in order to fulfill the cavity resonance condition simultaneously for both fundamental waves. In the DR-SFG setup which was used in this work, the optical cavity was stabilized with respect to the 532 nm fundamental laser, while the 760 nm fundamental laser was stabilized with respect to the cavity. Accordingly, the 532 nm fundamental laser was chosen as the *master* laser, the spectral properties of which are (to a large extent) transferred to the generated

[b] In LBO, the thermal expansion is strongly anisotropic. Nevertheless, from the thermal expansion coefficients which are in the order of 10^{-5} to 10^{-4}/ K, a number of 0.5 to 5 periodic oscillations is expected for the circulating power P_{532}^{circ}. This is in a rather good agreement with Fig. 4.3.

313 nm wave. In the following, a brief description will be given of the two fundamental lasers and the stabilization scheme employed. A more detailed description is found in Ref. [4].

For the two fundamental lasers, a resonantly frequency-doubled monolithic Nd:YAG laser [94,95] (*InnoLight*, type *Diabolo 1000 DW*) was used together with a Ti:sapphire laser (*Coherent*, type *MBR-110*), emitting at 532 and 760 nm wavelength, respectively. The frequency-doubled Nd:YAG laser was capable of delivering up to 1 W at 532 nm wavelength with a narrow linewidth of less than 100 kHz (measured within 1 s) and a frequency drift of less than 100 MHz/h. Continuous frequency tuning was possible by either changing the temperature of the Nd:YAG laser crystal or by changing the crystal geometry with a piezoelectric transducer. The corresponding tuning ranges were approximately 12 GHz and 300 MHz, respectively. Characterized by excellent spectral properties as well, the Ti:sapphire laser, which was pumped by a frequency-doubled Nd:YAG laser (*Coherent*, type *Verdi-V10*), was capable of delivering up to 1.5 W at 760 nm wavelength with a narrow linewidth of approximately 100 kHz. With the particular optics set in use, either coarse tuning over a range of approximately 80 nm or continuous tuning (mode-hop-free) over a range of approximately 30 GHz was possible. Accordingly, both the frequency-doubled Nd:YAG laser as well as the Ti:sapphire laser were equally well suited as *master* lasers. However, in the DR-SFG setup used in this work, the original choice of the 532 nm fundamental laser as the *master* laser was maintained from the previous version of the DR-SFG setup described in Refs. [1,2].

Stabilization of the optical enhancement cavity with respect to the frequency-doubled Nd:YAG laser as well as stabilization of the Ti:sapphire laser with respect to the cavity was realized by employing standard Pound-Drever-Hall technique [96] in reflection. In particular, use could be made of a residual 12 MHz phase modulation in the 532 nm light, emitted by the frequency-doubled Nd:YAG laser. This phase modulation stemmed from a 12 MHz phase modulation in the 1064 nm laser light, which was imparted by use of an electro-optical modulator (EOM) in order to allow for stabilization of an external cavity for resonant frequency doubling. Laser light at 532 nm wavelength, reflected from the incoupling mirror M1 (→ Sect. 4.2.2), was detected by a photodetector, the rf output of which was mixed in a double-balanced mixer (DBM) with the 12 MHz local oscillator. The error signal thus obtained was fed back via a proportional-integral-derivative (PID) electronic feedback loop of 15 kHz bandwidth to the piezoelectric actuator driving mirror M2 (→ Sect. 4.2.2). By this, the optical cavity length was stabilized to the 532 nm laser light. Likewise, laser light at 760 nm wavelength emitted by the Ti:Sapphire laser was imparted a 400 kHz phase modulation by use of a laser cavity mirror which was mounted on a piezoelectric transducer. The 760 nm laser light which was reflected from the incoupling mirror M1, was separated from the 532 nm laser light by use of an optical grating and sent to a second photodetector. The rf output of the photodetector was mixed in a double balanced mixer (DBM) with the 400 kHz local oscillator. The error signal thus obtained was fed back to the frequency control of the Ti:sapphire laser via a PID electronic feedback loop of 100 kHz bandwidth. Both locks were stable, allowing uninterrupted operation for many hours [1,4].

With the stabilization scheme thus described, a change in optical frequency $\Delta\omega_{532}$ of the frequency-doubled Nd:YAG laser (the *master* laser) is expected to cause a corresponding change in optical frequency $\Delta\omega_{760} = (\omega_{760}/\omega_{532})\Delta\omega_{532}$ of the Ti:sapphire laser. Accordingly, a change in frequency $\Delta\omega_{532}$ is also expected to cause a change in optical frequency

$$\Delta\omega_{313} \;=\; (1 + \frac{\omega_{760}}{\omega_{532}})\,\Delta\omega_{532} \tag{4.5}$$

of the generated 313 nm light. Strictly speaking, Eq. (4.5) applies to the ideal case where errors in the electronic feedback loops and the influence of the nonlinear crystal can be neglected. In this case, long-term frequency drifts as well as short-term frequency fluctuations of the generated 313 nm light are reduced to the level of those of the 532 nm light.

4.2.4 Output Power, Tunability, and Spectral Purity

The high output power which was achieved with the DR-SFG setup, results from the proper choice of the nonlinear crystal as well as the careful design of the optical enhancement cavity. In particular, strong enhancement of the two fundamental waves was achieved by minimizing the passive cavity losses and by choosing appropriate incoupling transmissions. The latter usually is referred to as *impedance matching*. Furthermore, each fundamental wave was matched to the respective Gaussian TEM_{00} cavity mode by use of a two-lens telescope and a pair of mirrors. This usually is referred to as *mode matching*. In the following, the DR-SFG setup will be characterized with respect to impedance and mode matching, as well as output power, tunability, and spectral purity.

In order to quantify mode matching, the ratio of power in a TEM_{00} cavity mode to the sum of powers in all TEM_{mn} cavity modes was measured by scanning the optical enhancement cavity and detecting the light leaking through mirror M4 (→ Sect. 4.2.2). By this, good estimates were obtained for the mode-matching factors $P_{532}^{\mathrm{in}}/P_{532}^{\Sigma}$ and $P_{760}^{\mathrm{in}}/P_{760}^{\Sigma}$, i.e. the ratios of the mode-matched input powers P_{532}^{in} and P_{760}^{in} (→ Sect. 4.2.1) to the measured total input powers P_{532}^{Σ} and P_{760}^{Σ} at 532 and 760 nm wavelength, respectively. Next, the cavity was locked in turn to each fundamental wave while the other fundamental wave was off. By this, the resonated powers P_{532}^{circ} and P_{760}^{circ} could be determined from the light leaking through mirror M4, where the residual transmissions of mirror M4 were measured before. From the data thus obtained, the enhancement factors $P_{532}^{\mathrm{circ}}/P_{532}^{\mathrm{in}}$ and $P_{760}^{\mathrm{circ}}/P_{760}^{\mathrm{in}}$ were calculated, quantifying resonant enhancement of the two fundamental waves in case of no losses due to frequency conversion. Finally, from the enhancement factors $P_{532}^{\mathrm{circ}}/P_{532}^{\mathrm{in}}$ and $P_{760}^{\mathrm{circ}}/P_{760}^{\mathrm{in}}$, and the incoupling transmissions T_{532} and T_{760} of mirror M1 (→ Sect. 4.2.2), the sums of all passive losses S_{532} and S_{760} were calculated from Eqs. (4.2a) and (4.2b). Since no losses due to frequency conversion were considered at that point, Eqs. (4.2a) and (4.2b) reduce to the two equations

		old LBO	new LBO	empty cavity
passive losses	$P_{532}^{\mathrm{circ}}/P_{532}^{\mathrm{in}}$	41.5	76.9	130
	$P_{760}^{\mathrm{circ}}/P_{760}^{\mathrm{in}}$	77.5	75.8	95.5
	S_{532}	2.4 %	1.3 %	0.53 %
	S_{760}	1.0 %	1.1 %	0.66 %
SFG	P_{313}	52 mW	101 mW	—
	h	0.051	0.054	—
optimized SFG	T_{532}^{opt}	2.6	1.5	—
	T_{760}^{opt}	1.1	1.2	—
	P_{313}^{opt}	65 mW	118 mW	—

Table 4.1: *Enhancement factors P_i^{circ}/P_i^{in}, passive losses S_i, output power P_i, Boyd-Kleinman factor h, optimum incoupling transmissions T_i^{opt}, and maximum output power P_i^{opt}, where $i \in \{313, 532, 760\}$. For comparison, enhancement factors and passive losses are also shown for the empty cavity. Mode matching was performed in each case, where mode-matched input powers and mode-matching factors were as follows. Old LBO:* $(P_{532}^{in}, P_{532}^{in}/P_{532}^{\Sigma}, P_{760}^{in}, P_{760}^{in}/P_{760}^{\Sigma}) = (377\,mW, 90.3\%, 693\,mW, 95.8\%)$. *New LBO:* $(400\,mW, 92.2\%, 692\,mW, 96.6\%)$. *Empty cavity:* $(389\,mW, 96.6\%, 265\,mW, 94.6\%)$.

$[T_i P_i^{\mathrm{in}}/P_i^{\mathrm{circ}}]^{1/2} = 1-[(1-T_i)(1-S_i)]^{1/2}$, with $i \in \{532, 760\}$, which could be solved independently. In Tab. 4.1, a summary is given of the enhancement factors $P_{532}^{\mathrm{circ}}/P_{532}^{\mathrm{in}}$ and $P_{760}^{\mathrm{circ}}/P_{760}^{\mathrm{in}}$, and the passive losses S_{532} and S_{760} for both the DR-SFG setup including the old as well as the new LBO crystal (→ Sect. 4.2.2). Accordingly, a significant decrease in passive losses S_{532} at 532 nm wavelength from 2.4% to 1.3% and a corresponding increase in enhancement factor $P_{532}^{\mathrm{circ}}/P_{532}^{\mathrm{in}}$ from 41.5 to 76.9 was achieved with the new LBO crystal, featuring sloped end faces and an improved AR coating. For comparison, the enhancement factors and the passive losses are also shown in case of an empty cavity, i.e. with the LBO crystal removed.

With the old LBO crystal, an average power of $P_{313} = 52\,\mathrm{mW}$ was generated at 313 nm wavelength. The mode-matched input powers were $P_{532}^{\mathrm{in}} = 377\,\mathrm{mW}$ and $P_{760}^{\mathrm{in}} = 693\,\mathrm{mW}$ at 532 and 760 nm wavelength, respectively. From this, a Boyd-Kleinman factor of $h = 0.051$ was calculated by numerical solution of the two coupled equations (4.2a) and (4.2b) together with Eq. (4.1), assuming passive losses as given in the first column of Tab. 4.1. Thus, only half the value was obtained for the Boyd-Kleinman factor h as compared to Ref. [4] [a]. With the new LBO crystal, an output power of $P_{313} = 101\,\mathrm{mW}$ was generated from mode-matched input powers of

[a] As noted in Sect. 4.2.2, noticeable changes of the enhancement factor $P_{532}^{\mathrm{circ}}/P_{532}^{\mathrm{in}}$ at 532 nm wavelength were observed with the old LBO crystal, caused by an etalon-like effect of the crystal endfaces. Thus, in Ref. [4], the passive losses of $S_{532} = 4.8\%$ which were calculated from a measured enhancement factor of $P_{532}^{\mathrm{circ}}/P_{532}^{\mathrm{in}} = 15$ are probably too high, leading to an overestimate of the Boyd-Kleinman factor h.

$P_{532}^{\mathrm{in}} = 400\,\mathrm{mW}$ and $P_{760}^{\mathrm{in}} = 692\,\mathrm{mW}$. This corresponds to a Boyd-Kleinman factor of $h = 0.054$ for the passive losses given in the second column of Tab. 4.1. Thus, almost identical values are obtained for the Boyd-Kleinman factor h with the two LBO crystals, indicating a good reliability of the measurements yielding the data of Tab. 4.1. Finally, it should be noted that requirement **R1** on the power of the generated light at 313 nm wavelength is easily fulfilled with both LBO crystals.

Perfect impedance matching would be achieved if choosing the incoupling transmissions equal to the respective total cavity losses, including passive losses as well as losses due to frequency conversion in the nonlinear crystal. Since the incoupling transmissions are $T_{532} = 1.85\%$ and $T_{760} = 2.67\%$, and the total cavity losses are dominated by the passive losses S_{532} and S_{760}, non-perfect impedance matching already can be inferred from the first four lines in Tab. 4.1. In particular, strong overcoupling of the optical enhancement cavity at 760 nm wavelength can be inferred for both LBO crystals. In order to estimate the possible gain in power P_{313}, perfect impedance matching is considered in Tab. 4.1 as well, assuming mode-matched input powers P_{532}^{in} and P_{760}^{in} as given above. To this end, the optimum incoupling transmissions T_{532}^{opt} and T_{760}^{opt} were calculated according to Eqs. (4.3a) and (4.3b) for both LBO crystals, assuming passive losses S_{532} and S_{760}, and Boyd-Kleinman factors h as given in Tab. 4.1. From this, the maximum output power P_{313}^{opt}, expected in case of perfect impedance matching, was calculated by numerical solution of the two coupled equations (4.2a) and (4.2b) together with Eq. (4.1). Accordingly, replacement of mirror M1 by a new one with optimum incoupling transmissions T_{532}^{opt} and T_{760}^{opt} would only yield a moderate increase in output power P_{313}. This is true in particular in case of the new LBO crystal.

With the stabilization scheme described in Sect. 4.2.3, a change in optical frequency $\Delta\omega_{532}$ of the 532 nm *master* laser is expected to cause a change in optical frequency $\Delta\omega_{760} = 0.6997 \cdot \Delta\omega_{532}$ of the 760 nm fundamental laser, assuming that errors in the electronic feedback loops and the influence of the crystal are negligible. This was confirmed experimentally by measuring the response of the locked Ti:sapphire laser to tuning of the frequency-doubled Nd:YAG laser, showing perfect agreement with the above relation [1,4]. Furthermore, continuous tuning without mode hops of the generated light at 313 nm wavelength was shown to be possible over a frequency range of more than 15 GHz. Thus, requirement **R3** on the tunability of the 313 nm light is fulfilled by more than 150%.

Finally, long-term frequency stability and short-term frequency fluctuations of the generated 313 nm laser light shall be considered briefly, where a more detailed discussion is found in Ref. [4]. Frequency drifts of the 313 nm light due to errors in the electronic feedback loops are estimated to be well below 1 MHz/h. Thus, long-term frequency stability of the 313 nm light is essentially determined by the long-term frequency stability of the 532 nm laser light, the latter being guaranteed by the absolute frequency stabilization which will be described in Sect. 4.3.1. Short-term frequency fluctuations $\delta\omega_{313}(t)$ of the 313 nm light, which are indicative of the spectral linewidth, were considered in Ref. [4]. In particular, it was shown that $\delta\omega_{313}(t)$ can be expressed in terms of the short-term frequency fluctuations $\delta\omega_{532}(t)$ of the 532 nm laser light and the deviations $\delta\omega_{532}^{\mathrm{cav}}(t)$ and $\delta\omega_{760}^{\mathrm{cav}}(t)$ of the cavity resonance

frequencies from the respective fundamental laser frequencies. Accordingly, in the ideal case of perfect electronic feedback loops, the short-term frequency fluctuations at 313 nm wavelength would be reduced to the level of those of the 532 nm laser light. By taking time records of the error signals of both frequency locks over 1 s time within a bandwidth of 10 Hz – 100 kHz, rms values of $\langle \delta\omega_{532}^{\mathrm{cav}}(t)/2\pi \rangle = 24\,\mathrm{kHz}$ and $\langle \delta\omega_{760}^{\mathrm{cav}}(t)/2\pi \rangle = 55\,\mathrm{kHz}$ were obtained. With the rms frequency fluctuations $\langle \delta\omega_{532}(t)/2\pi \rangle \approx 50\,\mathrm{kHz}$ of the frequency-doubled Nd:YAG *master* laser in the same bandwidth as above, an upper limit of $\langle \delta\omega_{313}(t)/2\pi \rangle \approx 160\,\mathrm{kHz}$ was calculated for the rms value of the short-term frequency fluctuations of the 313 nm light. Thus, requirement **R2** on the spectral linewidth of the generated 313 nm light can be expected to be fulfilled as well.

4.3 Absolute Frequency Stabilization

Due to the stabilization scheme described in Sect. 4.2.3, long-term frequency stability of the generated light at 313 nm wavelength essentially depends on the frequency stability of the 532 nm master laser. The long-term frequency stability of the free-running, frequency-doubled monolithic Nd:YAG laser is specified by a frequency drift of less than 100 MHz/h. According to Eq. (4.5), this directly translates into a corresponding frequency drift of 170 MHz/h at 313 nm wavelength. Although this is quite remarkable for a free-running system, a frequency drift small with respect to the natural linewidth $\gamma/2\pi = 19.4\,\mathrm{MHz}$ (FWHM) of the $^2S_{1/2} \leftrightarrow {}^2P_{3/2}$ cooling transition would be preferable in order to allow convenient experimental work for 1 – 2 h. Thus, long-term frequency stability of the generated light at 313 nm wavelength shall be specified by the requirement

R4: frequency drift $\leq$ 1 MHz/h .

This could be fulfilled easily by locking the frequency-doubled Nd:YAG laser to the I_2 frequency standard which will be described in Sect. 4.3.1.

In order to allow a frequency fine-adjustment of the absolute frequency stabilized 313 nm light, a standard acousto-optic modulator (AOM) in a double-pass configuration was used as a frequency shifter at 532 nm wavelength. This will be described in Sect. 4.3.2. The resulting tuning ranges are $\Delta\omega_{532}/2\pi = 200\,\mathrm{MHz}$ and $\Delta\omega_{313}/2\pi = 340\,\mathrm{MHz}$ [Eq. (4.5)] at 532 and 313 nm wavelength, respectively. Using both the I_2 frequency standard and the frequency shifter, the experimental steps used to produce a $^9Be^+$ ion crystal (→ chapters 6 & 7) were as follows.

Step 1: In order to effectively cool the $^9Be^+$ ions with an initial temperature of more than 1000 K, several scans of the 313 nm cooling laser light over a range of 3 – 5 GHz were required. To this end, the frequency-doubled Nd:YAG laser was unlocked from the I_2 frequency standard and scanned repeatedly by changing the temperature of the Nd:YAG laser crystal (→ Sect. 4.2.3).

Step 2: Once the $^9Be^+$ plasma crystallized, the absorption line of the $^9Be^+$ cooling transition narrowed down to a width not much more than the natural linewidth $\gamma/2\pi = 19.4\,\text{MHz}$ ($\rightarrow$ Sect. 6.2). At this point, the frequency-doubled Nd:YAG laser was stopped from scanning and locked to the I_2 frequency standard. Next, the frequency of the 313 nm cooling laser light was adjusted step-wise such that the center frequency of the $^9Be^+$ absorption line was within the frequency shifter tuning range $\Delta\omega_{532}/2\pi = 340\,\text{MHz}$. This was achieved by repeatedly unlocking and relocking the optical enhancement cavity to the 532 nm laser light as well as the 760 nm laser to the enhancement cavity.

Step 3: Finally, the frequency of the 313 nm cooling laser light was fine-adjusted with the frequency shifter by maximizing the fluorescence of the $^9Be^+$ ions.

If any unlocking between the fundamental lasers and the enhancement cavity or the I_2 frequency standard shall be avoided, a further increase of the frequency shifter tuning range would be required to at least a few GHz. This could be realized by, e.g., a second frequency doubled Nd:YAG laser, phase locked to the first one which in turn is locked to the I_2 frequency standard. Phase locking of the two lasers could be achieved by use of an electronic feedback loop as described in Ref. [97]. However, this would involve considerable costs of a second laser without reducing the experimental complexity significantly.

4.3.1 Doppler-Free Modulation Transfer Spectroscopy

The I_2 frequency standard for stabilization of the 532 nm laser light, was realized by Doppler-free modulation transfer spectroscopy (MTS) of molecular iodine [98]. By this, a frequency drift of less than 1 MHz/h could be achieved easily for the generated 313 nm light, as was required in the previous section. Since the experimental setup is almost identical to the one described in Ref. [99], only a brief description will be given here.

Doppler-free spectroscopy was achieved by overlapping two counterpropagating beams within the iodine cell which is shown in Fig. 4.4. In particular, a *pump* beam was used to "burn" a population hole into the velocity distribution of I_2 molecules in ground state, which then was probed by the *probe* beam (see, e.g., Ref. [100]). Thus, an increase in transmission of the probe beam occurred if the same velocity class of I_2 molecules was addressed by both beams, i.e the velocity class with zero velocity in the direction of beam propagation. Furthermore, a frequency (phase) modulation technique was employed to improve the signal-to-noise ratio of the spectroscopic signal as well as to obtain a first derivation of the absorption line profile, used as error signal for electronic feedback. In particular, a 455 kHz phase modulation was imparted to the pump beam by use of an electro-optic modulator (EOM). The phase modulation was transferred to the probe beam and converted into an amplitude modulation in case of resonance of the 532 nm laser light with an I_2 (hyperfine) transition. A rf photodetector including a narrow bandwidth 455 kHz ceramic filter was used to detect the amplitude modulation in the probe

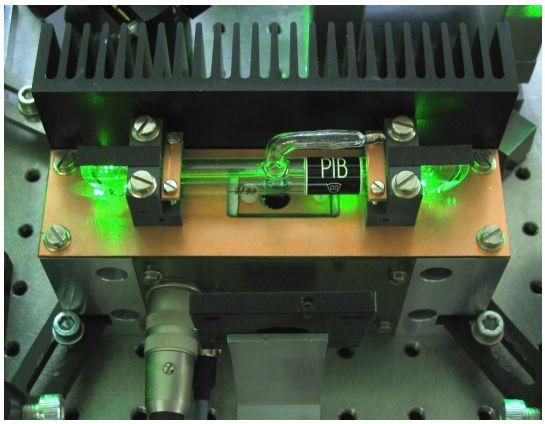

Figure 4.4: *Iodine cell, traversed by a pump and a counterpropagating probe beam. A Peltier cooler is integrated into the cell mount, allowing to cool down the cell finger to $-5°C$. However, in most cases the iodine cell was operated at room temperature (see text).*

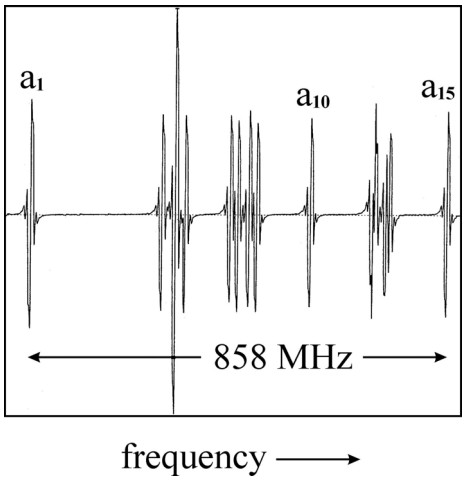

Figure 4.5: *Spectroscopic signal obtained by Doppler-free modulation transfer spectroscopy (MTS), showing the hyperfine structure of the 1110 [R(56)32-0] iodine line (taken from Ref. [99]). Usually, the laser light at 532 nm wavelength was locked to the a_{10} hyperfine line.*

beam. The detector output was mixed in a double balanced mixer (DBM) with the 455 kHz local oscillator. The signal thus obtained is shown in Fig. 4.5, illustrated by the 1110 [R(56)32-0] I_2 absorption line. Because of the transfer of 455 kHz modulation from the pump to the probe beam, this technique is usually referred to as modulation transfer spectroscopy (MTS). Finally, the MTS signal was fed back to the frequency-doubled Nd:YAG laser via a two-channel proportional-integral-derivative (PID) electronic feedback loop: a slow channel with a 1 Hz bandwidth was acting on the temperature of the Nd:YAG laser crystal, while a fast channel with a 1.4 kHz bandwidth was acting on the crystal geometry with a piezoelectric transducer (→ Sect. 4.2.3). By this, a stable as well as fast and tight lock was provided for the 532 nm laser light to the chosen I_2 hyperfine line. In Ref. [99], high long-term frequency stability of 532 nm laser light was demonstrated to be possible using an almost identical setup, where a frequency drift of less than 5 kHz/h [a] could be achieved.

According to requirement **R4**, frequency drifts of up to 1 MHz/h are still tolerable at 313 nm wavelength. Thus, a frequency drift of up to 600 kHz/h [Eq. (4.5)] is still tolerable at 532 nm wavelength, which is more than two orders of magnitude larger than that demonstrated in Ref. [99]. In consequence, the experimental MTS setup was slightly changed with respect to that described in Ref. [99], in favor of reducing both the number and costs of the required optical components.

[a] Actually, a frequency drift of less than 5 Hz/h is stated in Ref. [99]. However, this is obviously a mistake as can be seen from the estimate of light shifts as well as the axis labels in Fig. 3.21 (both in Ref. [99]).

In particular, an additional optical isolator was omitted from the pump beam and a low-cost acousto-optic modulator (AOM) was used in the probe beam. Thus, a residual interference of the two beams on the photodetector and an additional frequency drift of the probe beam were accepted, respectively. Furthermore, the experimental parameters were chosen somewhat different from their optimum values derived in Ref. [99], thus sacrificing frequency stability in favor of an increased signal-to-noise ratio of the MTS signal. In particular, the power of the pump beam typically was increased to 16 mW and the iodine cell was operated at room temperature, thus accepting an increase in power as well as pressure broadening of the I_2 hyperfine lines, respectively. Likewise, the 455 kHz rf drive voltage applied to the EOM was increased to 400 V (peak-to-peak), causing an increase in phase modulation index above its optimum value of $\beta_{\text{opt}} \approx 1$ [99]. Last but not least, a significantly more compact design of the experimental setup could be realized compared to that described in Ref. [99].

4.3.2 Frequency Shifter

In the schematic drawing of Fig. 4.1, a frequency shifter is placed between the frequency-doubled Nd:YAG laser and the I_2 frequency standard. The frequency shifter was realized by use of a standard acousto-optic modulator (AOM) in a double pass configuration, capable of shifting the 532 nm laser light by 300 – 500 MHz, i.e. with a tuning range of 200 MHz. A brief description of the experimental setup is given below.

The frequency shifter is shown in Fig. 4.6. A polarizing beamsplitter (PBS) was used to split off a typical power of $P_{\text{in}} = 40$ mW of horizontally polarized light at 532 nm wavelength from a total power of $P_\Sigma \approx 600$ mW, available from the frequency-doubled Nd:YAG laser. The horizontally polarized light which served as the input for the frequency shifter, straightly passed through the PBS before being 90°-deflected by two plane mirrors as can be seen in Fig. 4.6. The vertically polarized light of remaining power $P_\Sigma - P_{\text{in}}$ was reflected by the PBS to the left side of Fig. 4.6 and sent towards the DR-SFG setup (→ Sect. 4.2). A plano-convex lens ($f = 7.5$ cm), placed between the two plane mirrors, focused the light through a quarter-wave plate ($\lambda/4$) and into the AOM (*NEOS Technologies*, model *15200*). The beam waist was $w_0 \approx 60\mu$m and was located in the center of the AOM crystal. Light diffracted into the first order was retroreflected and focused back into the AOM by a concave mirror ($R = -10$ cm). Two iris diaphragm were used to block the zeroth as well as higher diffraction orders. Finally, after having doubly passed the AOM, the 532 nm laser light was counterpropagating along the path of the incoming beam and frequency-shifted by twice the frequency f_{rf} of the AOM rf drive voltage. Furthermore, by having doubly passed the $\lambda/4$ plate as well, the polarization of the outgoing 532 nm laser light was rotated by 90° with respect to that of the incoming beam. Thus, the outgoing light of power P_{out} was vertically polarized and reflected by the PBS to the right side of Fig. 4.6, i.e. towards the I_2 frequency standard (→ Sect. 4.3.1).

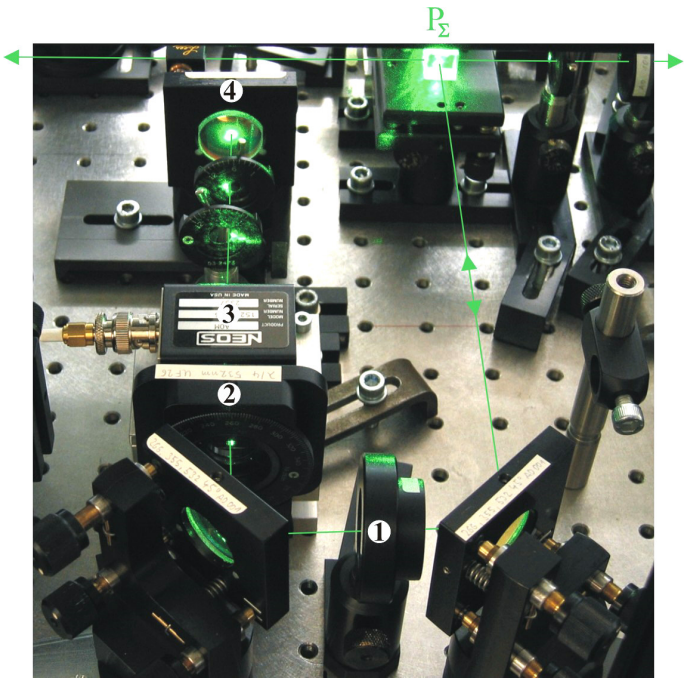

Figure 4.6: *Frequency shifter, including focusing lens (1), quarter-wave plate (2), acousto-optic modulator (3), and retroreflecting mirror (4). Laser beams at 532 nm wavelength are indicated by green lines. The two beams leaving at the upper left and right corners are directed towards the DR-SFG setup and the absolute frequency stabilization, respectively.*

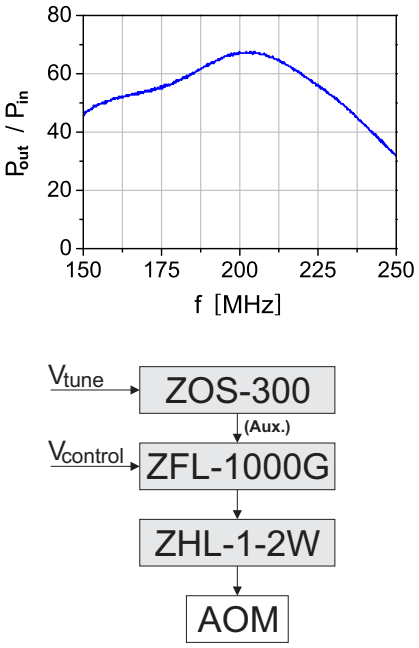

Figure 4.7: ***Top:*** *Efficiency P_{out}/P_{in} of the frequency shifter, measured as a function of the rf drive frequency f_{rf}. The optical tuning range at 532 nm wavelength is twice the tuning range of f_{rf}.* ***Bottom:*** *rf drive electronics, including a voltage controlled oscillator (ZOS-300), a variable gain amplifier (ZFL-1000G), and a power amplifier (ZHL-1-2W).*

Fig. 4.7 (top) shows the frequency shifter efficiency $P_{\text{out}}/P_{\text{in}}$, measured as a function of the rf drive frequency f_{rf}, where a maximum diffraction efficiency into the first order was ensured by adjusting the rf drive power to an optimum value of $P_{\text{rf}} = 28.2\,\text{dBm}$. Accordingly, more than 40% efficiency was possible over almost the full tuning range $\Delta f_{\text{rf}} = 100\,\text{MHz}$ which corresponds to an optical tuning range of $2 \cdot \Delta f_{\text{rf}} = 200\,\text{MHz}$ at 532 nm wavelength. A maximum efficiency of 67% was achieved around $f_{\text{rf}} = 200\,\text{MHz}$ which is the nominal center frequency of the AOM. Fig. 4.7 (bottom) shows a schematic of the rf drive electronics (all parts from *Mini-Circuits*), including a voltage-controlled oscillator (model *ZOS 300*), a variable gain amplifier (model *ZFL-1000G*), and a rf power amplifier (model *ZHL-1-2W*). Tuning of the rf drive frequency f_{rf} from 150 to 250 MHz was achieved by changing the voltage V_{tune} from 1.6 to 10.9 V. Likewise, adjustment of the rf drive power P_{rf} from -10 to $+30\,\text{dBm}$ was achieved by changing the voltage V_{control} from 5.0 to 1.2 V.

A further increase of the optical tuning range could be achieved by either using a high-frequency AOM [101] or by increasing the number of passes of the 532 nm laser light through the AOM. In particular, a sixtuple pass configuration

using a standard AOM was reported in Ref. [102], with a maximum efficiency of $P_{\mathrm{out}}/P_{\mathrm{in}} = 24\%$. However, while the first approach is based on expensive high-frequency components, the second approach requires a time-consuming adjustment in order to achieve a reasonable efficiency $P_{\mathrm{out}}/P_{\mathrm{in}}$.

Chapter 5

Laser-Cooled Fluorescence Mass Spectrometry (LCF-MS)

In chapter 6, dark regions in the CCD images of $^9Be^+$ ion crystals will be attributed to sympathetically cooled ions from the background gas which do not fluoresce in the 313 nm cooling laser light. In particular, it will be argued that dark regions in the crystal center consist of ions with a mass-to-charge ratio smaller than that of $^9Be^+$, i.e. $m/z < 9\,\mathrm{u}$, while dark regions at the outer crystal boundaries consist of ions with a mass-to-charge ratio larger than that of $^9Be^+$, i.e. $m/z > 9\,\mathrm{u}$. Here, $z = |Q|/e$, where $e = 1.602 \cdot 10^{-19}\mathrm{C}$ is the electron charge. More detailed information on the mass-to-charge ratios may be obtained by an experimental technique for which the term *laser-cooled fluorescence mass spectrometry* (LCF-MS) was introduced in Ref. [50]. This technique is non-destructive and easy to implement as compared to time-of-flight [52] as well as other mass-spectrometric techniques [53].

LCF-MS, as described in Ref. [50], relies on the excitation of secular ion motion at the transverse trap frequency

$$\omega_r(m/z) \;=\; \sqrt{\frac{e^2 z^2 U_{\mathrm{RF}}^2}{2\, m^2 \Omega^2 r_0^4} \;-\; \frac{\kappa\, e\, z\, U_{\mathrm{EC}}}{m}} \tag{5.1}$$

of the linear rf trap ($\rightarrow$ Sect.2.1). To this end, a dipolar electric excitation field $\mathbf{E}(t) = \mathbf{E}_{\mathrm{exc}} \sin(\omega_{\mathrm{exc}} t)$ is directed transverse to the trap axis and superimposed to the trapping fields. The excitation frequency ω_{exc} is scanned across the transverse trap frequency (5.1) of the sympathetically cooled ions, while monitoring the fluorescence of the laser-cooled ions. A temporary sympathetic heating of the laser-cooled ions is then reflected by a corresponding change in fluorescence signal, thus yielding a mass spectrum. In this work, the dipolar electric excitation field was generated by applying a voltage $U(t) = U_{\mathrm{exc}} \sin(\omega_{\mathrm{exc}} t)$ to an external electrode which was mounted slightly above the upper electrode rods of the linear rf trap ($\rightarrow$ Sect. 3.2). Finally, it should be noted that Eq. (5.1) is the degenerate case of Eqs. (2.3b) and (2.3c) at zero static voltage $U_{\mathrm{DC}} = 0$.

Historically, excitation of secular ion motion was first employed in measurements of charge transfer reactions [51] to selectively remove ions from a hyperbolic rf (Paul) trap. On the other hand, fluorescence detection of the resonant excitation of trapped ion motion was first employed in measurements of the electron-to-proton mass ratio m_e/m_p and the electron g_J factor [103]. In these measurements, resonant excitation of the cyclotron and axial motion of laser-cooled $^9Be^+$ ions in a Penning trap was detected by monitoring the fluorescence of the $^9Be^+$ ions, yielding m_e/m_p and g_J with sub-ppm-accuracies. Finally, LCF-MS which is a combination of both excitation of secular ion motion and fluorescence detection was introduced as a mass spectrometric technique [50,76,77,104] and used to identify several sympathetically cooled ion species. In addition, LCF-MS was also used to characterize a combined linear rf and magnetostatic trap [105]. Besides from excitation of the secular ion motion with a dipolar electric excitation field, LCF-MS in a linear rf trap could be performed as well by: (i) parametric excitation of the secular ion motion, i.e. excitation at twice the transverse trap frequency (5.1) with a quadrupolar rather than a dipolar electric field. (ii) excitation of the axial ion motion at the axial trap frequency ω_z [Eq. (2.3d)]. The practical use of both has been demonstrated in combination with ion counting, i.e. detection of the resonantly ejected ions with an electron multiplier. In particular, (i) was shown to yield a high mass resolution [106] while (ii) was introduced as a novel mass spectrometric technique, using an optimized axial trap potential [107].

The current chapter is organized as follows. In **Sect. 5.1**, a short description will be given of how the cooling laser detuning affects the fluorescence signal shape in the LCF-MS mass spectra. Next, direct secular excitation of the laser-cooled $^9Be^+$ ions will be described in **Sect. 5.2** as an intermediate step towards LCF-MS of the sympathetically cooled ions. Since the underlying physical mechanism is simpler as compared to the latter, this will serve as a first test of the understanding of the obtained fluorescence signal shapes. In particular, upward and downward excitation frequency scans will be compared in **Sect. 5.2.1** and **Sect. 5.2.2**, respectively. Furthermore, direct secular excitation of the laser-cooled $^9Be^+$ ions will be used to establish a precise mass scale for the LCF-MS mass spectra. This will be described in **Sect. 5.3**. This section also includes a summary of all sympathetically cooled ion species detected in this work using LCF-MS. Finally, a selection of LCF-MS mass spectra will be presented in **Sect. 5.3.1** (N^+), **Sect. 5.3.2** ($^4He^+$), and **Sect. 5.3.3** (HD^+ and D^+).

5.1 Cooling Laser Detuning

In LCF-MS, secular excitation of the sympathetically cooled ions in general results in the sympathetic heating of the laser-cooled ions. Exceptions to this are described in Sect. 5.3.2 and Sect. 5.3.3, where secular excitation leads to a decoupling of the two ion species. However, sympathetic heating of the laser-cooled ions still may be reflected by a decrease as well as an increase in fluorescence signal,

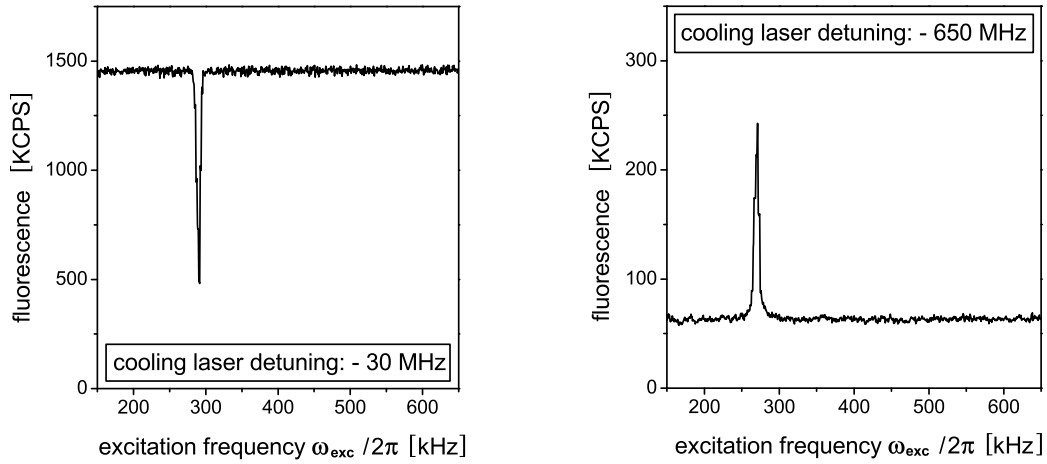

Figure 5.1: *Two excitation frequency scans across the transverse trap frequency of the $^9Be^+$ ions.* ***Left:*** *At a cooling laser detuning of approximately −30 MHz.* ***Right:*** *At a cooling laser detuning which was further increased by −620 MHz.*

depending on the particular cooling laser detuning. This will be demonstrated in the following, using direct secular excitation of the laser-cooled ions rather than secular excitation of the sympathetically cooled ions.

Fig. 5.1 (left) shows an excitation frequency scan across the transverse trap frequency of the $^9Be^+$ ions. The complete scan ranging from $\omega_{\rm exc}/2\pi = 100\,$kHz to 1 MHz was performed within 50 s and with an excitation amplitude of $U_{\rm exc} = 1\,$V. The linear rf trap was operated at $U_{\rm RF} = 380\,$V and $U_{\rm EC} = 3\,$V, corresponding to a theoretical trap frequency of $\omega_{r(\rm Be)}/2\pi = 271\,$kHz [Eq. (5.1)]. Preparation of the $^9Be^+$ ions included the following steps. First, the trap was loaded with $^9Be^+$ ions at a background pressure of $P < 1 \cdot 10^{-10}\,$mbar. Next, the $^9Be^+$ ions were cooled down to a temperature of few 10 K (→ Sect. 6.2) by several 3 – 5 GHz scans of the cooling laser frequency. Finally, a reduction of the total number of trapped ions by lowering the rf amplitude $U_{\rm RF}$ for a few seconds led to the crystallization of the trapped ion cloud. The cooling laser was locked to an I_2 hyperfine transition (→ Sect. 4.3.1) and fine-adjusted approximately −30 MHz below the cooling transition frequency by maximizing the fluorescence of the $^9Be^+$ ions. Accordingly, any broadening of the $^9Be^+$ absorption line by heating the $^9Be^+$ ions is expected to cause a decrease in fluorescence signal. Indeed, in Fig. 5.1 (left), a *dip* appears around the theoretical trap frequency $\omega_{r(\rm Be)}/2\pi = 271\,$kHz [Eq. (5.1)]. It should be noted that there is no significant frequency shift with respect to the theoretical value, even though the $^9Be^+$ ions were in a crystalline state. This is due to the fact that the $^9Be^+$ plasma was almost pure, leading to a coherent oscillation of the whole $^9Be^+$ ion crystal in the time-averaged trap potential (2.3).

Fig. 5.1 (right) shows a further excitation frequency scan performed right after the one shown in Fig. 5.1 (left). The same experimental settings were used, except from a somewhat lower excitation amplitude of $U_{\rm exc} = 0.5\,$V and a cooling laser detuning which was further increased by −620 MHz. To this end, the Ti:sapphire laser was unlocked from the SFG cavity (→ Sect. 4.2.2), red-detuned by one SFG

cavity free spectral range (FSR = 620 MHz), and locked to the SFG cavity again. As a result, melting of the $^9Be^+$ ion crystal and transition into a cloud-like state was observed with the CCD camera. This is reflected by the decrease in fluorescence signal in Fig. 5.1 (right) by approximately a factor of 20 with respect to Fig. 5.1 (left). Furthermore, a *peak* appears in place of the *dip*. The latter can be understood from the fact that for the given cooling laser detuning, the fluorescence already corresponds to the outer wing of the $^9Be^+$ absorption line (→ Sect. 6.2). Thus, any broadening of the $^9Be^+$ absorption line by heating the $^9Be^+$ ions is expected to cause an increase in fluorescence signal.

In the remainder of this chapter, solely excitation frequency scans will be shown which were performed at a cooling laser detuning similar to that in Fig. 5.1 (left). Thus, any heating of the $^9Be^+$ ions is expected to cause a corresponding decrease in fluorescence signal.

5.2 Secular Excitation of Laser-Cooled Ions

In this section, direct secular excitation of the laser-cooled $^9Be^+$ ions will be described, the $^9Be^+$ ions forming a large ion cloud together with additionally trapped ions from the background gas. The transverse trap frequency of the $^9Be^+$ ions is given by Eq. 5.1 which may be rewritten as

$$\omega_{r(\mathrm{Be})}\,[\mathrm{kHz}] \;=\; \sqrt{20.7\,U_{\mathrm{RF}}^2 \;-\; 32\cdot 10^3\,U_{\mathrm{EC}}}\quad , \tag{5.2}$$

where the trap voltages U_{RF} and U_{EC} are expressed in units of Volt. Fixed trap parameters were assumed as $r_0 = 4.32\,\mathrm{mm}$, $\kappa = 3.0\cdot 10^{-3}/\mathrm{mm}^2$ (→ Sect. 3.2), and $\Omega/2\pi = 14.2\,\mathrm{MHz}$ (→ Sect. 3.3). The main sources of error in Eq. (5.2) are the uncertainties in rf amplitude U_{RF} (up to ±10%) and geometric constant κ (up to ±15%), where the latter is entering Eq. (5.2) through the constant factor 32. Accordingly, the uncertainty in κ is only of minor importance since the second term below the square root in Eq. (5.2) only contributes a small correction of $< 3.2\%$ to the transverse trap frequency $\omega_{r(\mathrm{Be})}$. This at least is true for typical trap voltages $U_{\mathrm{RF}} > 350\,\mathrm{V}$ and $U_{\mathrm{EC}} < 5\,\mathrm{V}$. Finally, it should be noted that Eq. (5.2) is a single particle frequency. Thus, resonant secular excitation of the $^9Be^+$ ions is expected to occur at Eq. (5.2) if performed on either a pure $^9Be^+$ ion plasma or on a multi-species ion plasma which is in a cloud-like state. In the first case, the $^9Be^+$ ion plasma coherently oscillates as a whole while in the second case, Coulomb interactions are sufficiently small.

5.2.1 Experimental Results: I. $^9Be^+$ – Upward Scans

Fig. 5.2 shows an excitation frequency scan across the transverse trap frequency of the $^9Be^+$ ions. The complete scan ranging from $\omega_{\mathrm{exc}}/2\pi = 100\,\mathrm{kHz}$ to 500 kHz was performed within 50 s and with an excitation amplitude of $U_{\mathrm{exc}} = 1\,\mathrm{V}$. The

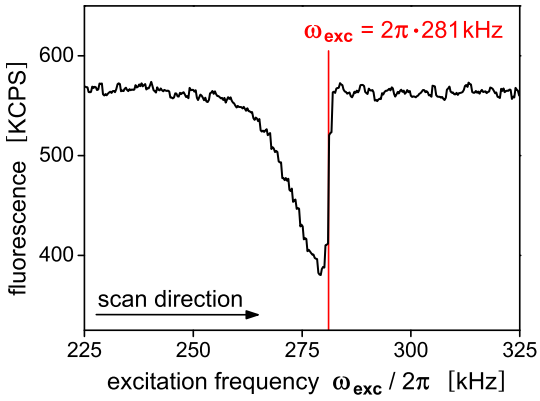

Figure 5.2: *Upward excitation frequency scan across the transverse trap frequency of the $^9Be^+$ ions.*

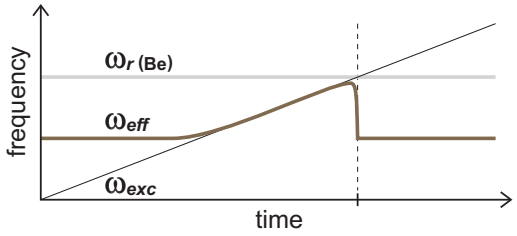

Figure 5.3: *Supposed change in time of ω_{eff}, drawn in a qualitative fashion in the style of Ref. [54].*

linear rf trap was operated at $U_{\text{RF}} = 380\,\text{V}$ and $U_{\text{EC}} = 3\,\text{V}$, corresponding to a theoretical trap frequency of $\omega_{r(\text{Be})}/2\pi = 271\,\text{kHz}$ [Eq. (5.2)]. The stability parameter is $q = 0.055$ [Eq. (2.1)], implying that the time-averaged trap potential description is valid (→ Sect. 2.1). Preparation of the trapped ion cloud included the same steps as described in the previous section. However, no further reduction of the number of trapped ions was performed, e.g., by lowering the rf amplitude U_{RF} for a few seconds. Thus, a large number of $^9Be^+$ ions as well as additionally trapped impurity ions were expected to be contained in the trap, with a temperature of a few 10 K (→ Sect. 6.2). In the RGA mass spectra (→ Sect. 3.1), peaks were observed at $m/z = 4, 14, 16, 20, 28, 32$ and 40 u, corresponding to He^+, N^+, O^+, Ar^{++}, N_2^+, O_2^+, and Ar^+, respectively (see, e.g., [83]).

In Fig. 5.2, the fluorescence signal shape exhibits the characteristic features explained by the simplified model of LCF-MS (→ Sect. 2.3.2): a gradual decrease on the low-frequency side and a step-like increase on the high frequency side in the upward excitation frequency scan. However, the model describes LCF-MS of sympathetically cooled ions rather than direct secular excitation of the laser-cooled ions. Nevertheless, a qualitative explanation of the fluorescence signal shape is possible in terms of the *effective* trap frequency ω_{eff} which was introduced as a major concept of the simplified model of LCF-MS in Sect. 2.3.1.

Fig. 5.3 shows the supposed change in time of the *effective* trap frequency ω_{eff}, i.e. the transverse trap frequency of the $^9Be^+$ ions in the superposition of the time-averaged trap potential and the space charge potential of the impurity ions. At the start of the excitation frequency scan, ω_{eff} is shifted well below the nominal trap frequency $\omega_{r(\text{Be})}$ [Eq. (5.2)]. As a rough estimate, a shift of $(\omega_{r(\text{Be})} - \omega_{\text{eff}})/2\pi \approx 20\,\text{kHz}$ is calculated from Eq. (2.12) for a total number of 1000 impurity ions with an average mass of $m/z = 20\,\text{u}$ and a temperature of 10 K. Next, as the excitation frequency ω_{exc} approaches the *effective* trap frequency ω_{eff}, kinetic excitation of the $^9Be^+$ ions sets in. A negative feedback is established similar to that described under case I in Sect. 2.3.2: kinetic excitation of the $^9Be^+$ ions causes a

sympathetic heating of the impurity ions, and the whole ion cloud expands. This in turn leads to an increase in *effective* trap frequency ω_{eff} since space charge becomes less pronounced. As a result, ω_{eff} becomes locked to the excitation frequency ω_{exc} (a further increase of ω_{eff} above the excitation frequency ω_{exc} would weaken the coupling of the external excitation to the $^9Be^+$ ions). Finally, as the excitation frequency ω_{exc} is scanned across the nominal trap frequency $\omega_{r(\text{Be})}$ [Eq. (5.2)] (dotted line in Fig. 5.3), the $^9Be^+$ ions are decoupled from the external excitation since ω_{eff} can not increase any more. As a result, the $^9Be^+$ ions are quickly cooled down. According to this explanation, the negative feedback and the decoupling of $^9Be^+$ ions from the external excitation are reflected by the gradual decrease and the step-like increase in fluorescence in Fig. 5.2, respectively. The latter occurs at $\omega_{\text{exc}}/2\pi = 281\,\text{kHz}$, corresponding to a deviation of +4% with respect to the theoretical value $\omega_{r(\text{Be})}/2\pi = 271\,\text{kHz}$ [Eq. (5.2)]. Taking into account the uncertainties in U_{RF} and κ ($\rightarrow$ Sect. 5.2), the agreement is rather good. In Fig. 5.2, the fluorescence signal finally reaches its initial level, indicating that no significant amount of $^9Be^+$ ions was lost from the trap.

5.2.2 Experimental Results: II. $^9Be^+$ – Downward Scans

Fig. 5.4 (top) shows a downward excitation frequency scan across the transverse trap frequency of the $^9Be^+$ ions. The complete scan ranging from $\omega_{\text{exc}}/2\pi = 290\,\text{kHz}$ down to 250 kHz was performed within 20 s and with an excitation amplitude of $U_{\text{exc}} = 0.5\,\text{V}$. The linear rf trap was operated at $U_{\text{RF}} = 380\,\text{V}$ and $U_{\text{EC}} = 3\,\text{V}$, corresponding to a theoretical trap frequency of $\omega_{r(\text{Be})}/2\pi = 271\,\text{kHz}$ [Eq. (5.2)]. Preparation of the trapped ion cloud included the following steps. First, the trap was loaded with $^9Be^+$ ions at a slightly elevated background pressure of $P = 1.2 \cdot 10^{-10}\,\text{mbar}$ since the experiment was performed shortly after a vacuum chamber bakeout. In the RGA mass spectra ($\rightarrow$ Sect. 3.1), peaks were observed at $m/z = 2, 14, 16, 17, 18, 20, 28, 32$ and 40 u, corresponding to H_2^+, N^+, O^+, HO^+, H_2O^+, Ar^{++}, N_2^+, O_2^+ and Ar^+, respectively [83]. After completing the loading process, the cooling laser was locked to an I_2 hyperfine transition ($\rightarrow$ Sect. 4.3.1) and fine-adjusted a few 10 MHz below the cooling transition frequency by maximizing the fluorescence of the $^9Be^+$ ions. No further cooling of the $^9Be^+$ ions nor any reduction of the total number of trapped ions was performed. Thus, a large ion cloud with an increased fraction of additionally trapped impurity ions and a temperature of $T \gg 10\,\text{K}$ ($\rightarrow$ Sect. 6.2) was expected to be confined in the trap.

In Fig. 5.4 (top), the fluorescence signal shows a broad symmetric dip, centered around $\omega_{\text{exc}}/2\pi = 274\,\text{kHz}$. This corresponds to a deviation of only +1% with respect to the theoretical trap frequency $\omega_{r(\text{Be})}/2\pi = 271\,\text{kHz}$ [Eq. (5.2)]. Since the dip shape does not exhibit any special features, no further explanation is needed. However, in order to serve as a starting point for the following discussion, Fig. 5.5 (top) shows the supposed change in time of the *effective* trap frequency ω_{eff}. As in the previous section, ω_{eff} is defined as the transverse trap frequency of the $^9Be^+$ ions in the superposition of the time-averaged trap potential and the space charge potential of the impurity ions. Accordingly, due to the comparatively high temperature of the

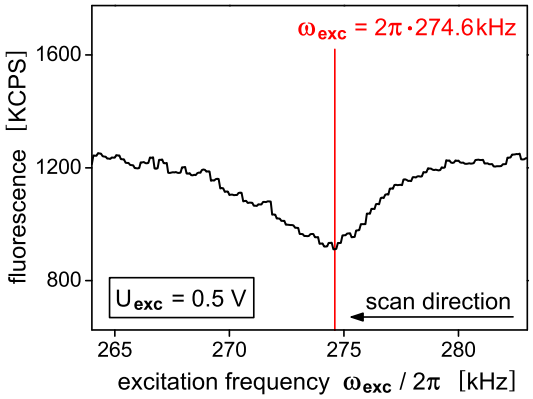

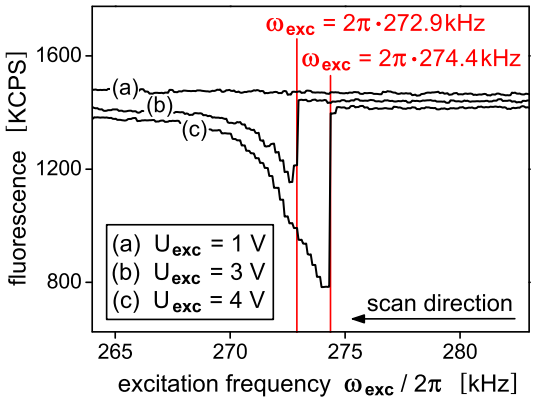

Figure 5.4: *Downward excitation frequency scans across the transverse trap frequency of the $^9Be^+$ ions.* ***Top:*** *Large ion cloud with an increased fraction of impurity ions.* ***Bottom:*** *After removal of the high-mass impurity ions. Note: Offsets of ±30 KCPS have been added to (a) and (c), respectively.*

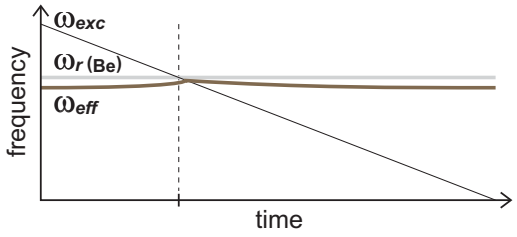

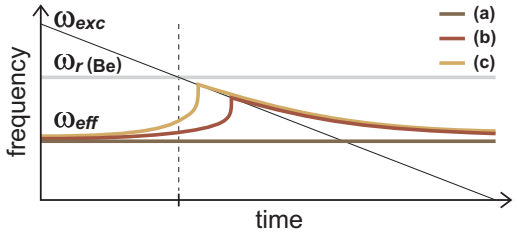

Figure 5.5: *Supposed change in time of ω_{eff}, drawn in a qualitative fashion in the style of Ref. [54].* ***Top:*** *Change in time of ω_{eff} corresponding to Fig. 5.4 (top).* ***Bottom:*** *Changes in time of ω_{eff} corresponding to the fluorescence signals (a), (b), and (c) in Fig. 5.4 (bottom).*

trapped ion cloud, space charge is less pronounced and ω_{eff} is only slightly shifted with respect to the nominal trap frequency $\omega_{r(\text{Be})}$ [Eq. (5.2)]. Thus, no asymmetric feature appears in the dip shape since this relies on space charge and a noticeable change in time of the *effective* trap frequency ω_{eff}.

Right after completing the excitation frequency scan, a static voltage $U_{\text{DC}} = 4\,\text{V}$ ($\rightarrow$ Sect. 2.1) was applied to the trap electrodes in a quadrupolar configuration. By this, all impurity ions with a mass-to-charge ratio $m/z \geq 12\,\text{u}$ were removed from the trap, leaving behind only H_2^+, H_3^+ (from the reaction $H_2^+ + H_2 \rightarrow H_3^+ + H$), Be^+ , and BeH^+ ions. After switching off the static voltage U_{DC}, the fluorescence signal immediately rose from approximately 1200 to 1450 KCPS due to the reduced rf heating by the impurity ions. Fig. 5.4 (bottom) shows three consecutive excitation frequency scans, performed right after removal of the high-mass impurity ions. The same experimental settings were used as in Fig. 5.4 (top), except from an excitation amplitude which was increased to $U_{\text{exc}} = 1\,\text{V}$ (a), 3 V (b) and 4 V (c). While in (a),

the fluorescence signal does not show any response at all, in (b) and (c), a dip appears with the same asymmetric features as in the upward excitation frequency of the previous section. Furthermore, by increasing the excitation amplitude from $U_{\mathrm{exc}} = 3\,\mathrm{V}$ (b) to $4\,\mathrm{V}$ (c), the step-like decrease in fluorescence noticeably shifts towards the high-frequency side of the excitation frequency scan.

Fig. 5.5 (bottom) shows the supposed change in time of the *effective* trap frequency ω_{eff} for the fluorescence signals (a), (b), and (c) in Fig. 5.4 (bottom). In each case, ω_{eff} is assumed to have shifted noticeably with respect to Fig. 5.4 (top), due to the decrease in temperature of the trapped ion cloud. As the excitation frequency ω_{exc} is scanned across the nominal trap frequency $\omega_{r(\mathrm{Be})}$ [Eq. 5.2] (dotted vertical line in Fig. 5.5), kinetic excitation of the $^9\mathrm{Be}^+$ ions already takes place to certain extents in the theoretical curves (b) and (c). This is indicated by a corresponding increase in *effective* trap frequency ω_{eff} which is due to the sympathetic heating of the impurity ions. Thus, a positive feedback is triggered similar to that described under case II in Sect. 2.3.2: the more the excitation frequency ω_{exc} approaches the *effective* trap frequency ω_{eff}, the more effective the coupling of the external excitation to the $^9\mathrm{Be}^+$ ions becomes. This in turn further reduces the difference between the two frequencies due to the increased sympathetic heating of the impurity ions and the resulting increase in ω_{eff}. Thus, an almost step-like increase in temperature of the $^9\mathrm{Be}^+$ ions occurs which is reflected by the step-like decrease in fluorescence signals (b) and (c) in Fig. 5.4 (bottom). Furthermore, the onset of positive feedback is expected to shift towards the nominal trap frequency $\omega_{r(\mathrm{Be})}$ [Eq. (5.2)] (dotted vertical lines in Fig. 5.5) with increasing excitation amplitude. This agrees well with the fluorescence signals (b) and (c) in Fig. 5.4 (bottom), obtained at $U_{\mathrm{exc}} = 3\,\mathrm{V}$ and $4\,\mathrm{V}$, respectively. Moreover, the step-like decrease in fluorescence (c) occurs at almost the same excitation frequency as the center of the broad symmetric dip in Fig. 5.4 (top). Accordingly, while at $U_{\mathrm{exc}} = 1\,\mathrm{V}$ (a), no positive feedback is triggered at all, at $U_{\mathrm{exc}} = 4\,\mathrm{V}$ (c), the onset of positive feedback almost has shifted completely towards the nominal trap frequency $\omega_{r(\mathrm{Be})}$ [Eq. (5.2)].

Finally, it should be noted that the asymmetric fluorescence signal shape may also be attributed to the residual anharmonicity of the trap potential due to the non-hyperbolic electrode cross sections (as was argued in Ref. [108]). However, for the linear rf trap used in this work (→ Sect. 3.2), a change in transverse trap frequency of less than 1 kHz is expected if increasing the amplitude of the $^9\mathrm{Be}^+$ ion transverse motion from 0.1 mm to 3 mm. This was shown by Fourier transforms of $^9\mathrm{Be}^+$ ion trajectories, simulated with SIMION 6 software.

5.3 LCF-MS of Sympathetically Cooled Ions

In this section, detection of sympathetically cooled ions by LCF-MS will be described. The transverse trap frequency of a sympathetically cooled ion with mass m_{SC} is given by Eq. (5.1) which may be rewritten as

m/z	RGA Detection	Assigned Ion Species	Further Discussions
2	yes	D^+, H_2^+	Sect. 5.3.3 & Ref. [9]
3	yes	HD^+, H_3^+	
4	yes	He^+	Sect. 5.3.2 & Ref. [8]
6	no	C^{++}	see caption, note 1
7	no	N^{++}	—
9	no	Be^+	Sect. 5.2.1 & 5.2.2
10	no	BeH^+	Ref. [109]
11	no	BeD^+	
12	no	C^+	see caption, note 1
14	yes	N^+, N_2^{++}	see caption, note 2
15	no	NH^+	
16	yes	O^+, O_2^{++}	
17	yes	HO^+	see caption, note 3
18	yes	H_2O^+, NH_4^+	
19	no	H_3O^+	

Table 5.1: *Summary of all mass-to-charge ratios m/z (in units of u) detected in this work, using laser-cooled fluorescence mass spectrometry (LCF-MS), together with the assigned ion species. Additional information is given on whether a particular m/z was also detected with the residual gas analyzer (RGA).* ***Notes:*** ***(1)*** *From dissociation of CO and CO_2.* ***(2)*** *No unambiguous assignment was possible to either m/z = 14, 15, or 16 u, where m/z=15 is the mass of the NH^+ [44] ion. This will be further discussed in Sect. 5.3.1.* ***(3)*** *While in the RGA mass spectra, two peaks appeared at m/z=17 and 18, a broad dip appeared in the LCF-MS mass spectra, covering the whole range m/z=17 –19. According to Ref. [77], trapped H_2O^+ is expected to react with neutral H_2 and H_2O from the background gas to H_3O^+ within 1 s. The trapped H_3O^+ may further react with NH_3 (ammonia), also contained in the background gas, to NH_4^+ on a much longer time scale. Thus, the broad dip in the LCF-MS mass spectra will be assigned to a combination of HO^+, H_2O^+, NH_4^+, and H_3O^+ ions.*

$$\omega_{r(\mathrm{SC})} \;=\; \frac{m_{\mathrm{Be}}}{m_{\mathrm{SC}}}\,\sqrt{\omega_{r(\mathrm{Be})}^2 \;-\; \frac{1}{2}\left(\frac{m_{\mathrm{SC}}}{m_{\mathrm{Be}}} \;-\; 1\right)\omega_{z(\mathrm{Be})}^2} \quad . \tag{5.3}$$

Here, singly charged ($z = 1$) ions were assumed, where the extension to the general case $z > 1$ does not imply any special difficulties. Thus, rather than being expressed in terms of r_0, κ, U_{RF}, U_{EC}, and Ω ($\rightarrow$ Sect. 2.1), Eq. (5.3) is expressed in terms of the mass ratio $m_{\mathrm{SC}}/m_{\mathrm{Be}}$ and the trap frequencies $\omega_{r(\mathrm{Be})}$ and $\omega_{z(\mathrm{Be})}$ of the $^9Be^+$ ions. The latter two frequencies both can be measured by direct secular excitation of the laser-cooled $^9Be^+$ ions as was shown in Sect. 3.2, thus circumventing the uncertainties in U_{RF} and κ ($\rightarrow$ Sect. 5.2). However, the axial trap frequency still may be calculated according to $\omega_{z(\mathrm{Be})}[\mathrm{kHz}] = 2.5 \cdot 10^2 \sqrt{U_{\mathrm{EC}}[\mathrm{V}]}$ [Eq. (2.3d) with

$\kappa = 3.0 \cdot 10^{-3}/\,\mathrm{mm}^2$] since the second term below the square root in Eq. (5.3) only contributes a small correction of $< 3.3\%$ to the transverse trap frequency $\omega_{r(\mathrm{SC})}$. This at least is true for typical trap voltages $U_{\mathrm{RF}} > 350\,\mathrm{V}$ and $U_{\mathrm{EC}} < 5\mathrm{V}$, and for the mass range $2\,\mathrm{u} < m_{\mathrm{SC}} < 18\,\mathrm{u}$. Finally, it should be noted that Eq. (5.3) is a single particle frequency. Thus, resonant secular excitation of the sympathetically cooled ions is expected to occur at $\omega_{r(\mathrm{SC})}$ [Eq. (5.3)] if the ions are in a cloud-like state where Coulomb interactions are sufficiently small.

By means of Eq. (5.3), a mass scale can be assigned to the fluorescence signal monitored over a given excitation frequency range. However, identification of a particular mass m_{SC} may be complicated by the fact that the fluorescence signal shape can differ considerably from the characteristic asymmetric dip explained in Sect. 2.3.2. This depends on the particular experimental settings and the sympathetically cooled ion species. Examples will be given in Sect. 5.3.1 (N^+), Sect. 5.3.2 ($^4He^+$), and Sect. 5.3.3 (HD^+ and D^+). Finally, a summary is shown in Tab. 5.1 of all mass-to-charge ratios detected in this work, using LCF-MS, together with the assigned ion species. Additional information is given on whether a particular mass-to-charge ratio was also detected with the residual gas analyzer (RGA) ($\rightarrow$ Sect. 3.1).

5.3.1 Experimental Results: I. $^{14}N^+$

Fig. 5.6 shows a LCF-MS mass spectrum of either N^+, NH^+, or O^+ sympathetically cooled ions (see discussion below), obtained from an upward excitation frequency scan. The complete scan ranging from $\omega_{\mathrm{exc}}/2\pi = 100\,\mathrm{kHz}$ to 500 kHz was performed within 50 s and with an excitation amplitude of $U_{\mathrm{exc}} = 1\,\mathrm{V}$. The linear rf trap was operated at $U_{\mathrm{RF}} = 380\,\mathrm{V}$ and $U_{\mathrm{EC}} = 3\,\mathrm{V}$, corresponding to a stability parameter of $q \leq 0.25$ [Eq. (2.1)] for $m/z \geq 2\,\mathrm{u}$. This implies that the time-averaged potential description is valid for the whole mass range $m/z \geq 2\,\mathrm{u}$ ($\rightarrow$ Sect. 2.1). Preparation of the trapped ion cloud included the following steps. First, the trap was loaded with $^9Be^+$ ions at a background pressure of $P < 1 \cdot 10^{-10}$ mbar. Next, the $^9Be^+$ ions were cooled down to a temperature of a few 10 K ($\rightarrow$ Sect. 6.2) by several 3 – 5 GHz scans of the cooling laser frequency. The cooling laser was locked to an I_2 hyperfine transition ($\rightarrow$ Sect. 4.3.1) and fine-adjusted a few 10 MHz below the cooling transition frequency by maximizing the fluorescence of the $^9Be^+$ ions. Since the total number of trapped ions was not further reduced, the ions remained in a cloud-like state. Finally, neutral H_2 gas [a] was introduced into the vacuum chamber through a leak valve up to a pressure of $P = 1.9 \cdot 10^{-9}$ mbar. Before obtaining the LCF-MS mass spectrum shown in Fig. 5.6, the transverse trap frequency of the $^9Be^+$ ions was determined as $\omega_{r(\mathrm{Be})}/2\pi = 279\,\mathrm{kHz}$ ($\rightarrow$ Sect. 5.2). From this, a mass scale was established by use of Eq. (5.3) which is shown on the upper horizontal axis in Fig. 5.6.

[a] The main goal of the experiment was to investigate the formation of BeH^+ molecular ions by the chemical reaction $Be^+ + H_2 \rightarrow BeH^+ + H$ [109].

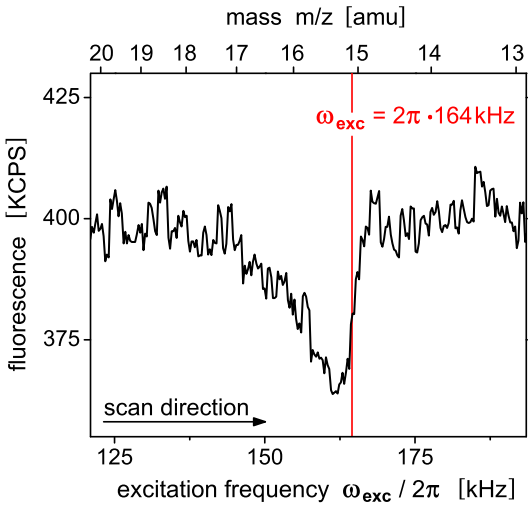

Figure 5.6: *LCF-MS mass spectrum, showing the presence of either N^+, NH^+, or O^+ sympathetically cooled ions (see text).*

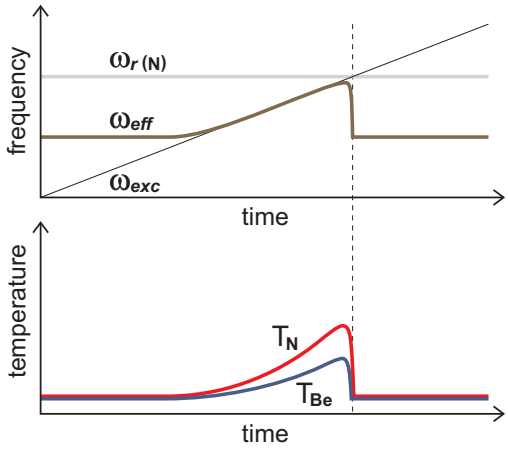

Figure 5.7: *Supposed change in time of ω_{eff}, T_{LC}, and T_{SC}, drawn in a qualitative fashion in the style of Ref. [54].*

In Fig. 5.6, a dip appears in the fluorescence signal with the characteristic asymmetric features explained by the simplified model of LCF-MS (→ Sect. 2.3.2). In particular, a gradual decrease on the low frequency side is followed by a step-like increase on the high frequency side in the upward excitation frequency scan. According to the model, the step-like increase is expected to occur at the transverse trap frequency (5.3). In Fig. 5.6, the step-like increase occurs at $\omega_{\text{exc}}/2\pi = 164\,\text{kHz}$, corresponding to mass $m/z \approx 15\,\text{u}$ on the upper mass scale. However, in LCF-MS, significant frequency shifts may occur even in the cloud-like state [110]. Accordingly, the dip in Fig. 5.6 may be assigned to $m/z = 14\,\text{u}$ or $16\,\text{u}$ as well. In particular, $^{14}N^+$ and $^{16}O^+$ ions are likely to be trapped since neutral N_2 and O_2 molecules are always present in the background gas. In Ref. [44], an experiment is described where $^{24}Mg^+$ ions were loaded into a Penning trap while at the same time air was introduced into the vacuum chamber up to a pressure of a few 10^{-8} mbar. A LCF-MS mass spectrum was obtained from the fluorescence of the laser-cooled $^{24}Mg^+$ ions by exciting the plasma breathing modes [111]. Besides from masses $m/z = 12\,\text{u}$ and $24\,\text{u}$, corresponding to $^{24}Mg^{++}$ and $^{24}Mg^+$, respectively, no masses other than $m/z = 29\,\text{u}$ and $15\,\text{u}$ were found. These masses were assigned to the N_2H^+ molecular ion and its fragment NH^+, respectively, since it was argued that the proton affinity energy of trapped N_2^+ makes the reaction $N_2^+ + H_2 \rightarrow N_2H^+ + H$ very likely [112]. Thus, the fluorescence dip in Fig. 5.6 may be assigned to either $^{14}N^+$, $^{14}NH^+$, or $^{16}O^+$ sympathetically cooled ions, where the first is the most likely. Finally, it should be noted that the fluorescence signal base line ($\approx 400\,\text{KCPS}$) is rather low if taking into account the low temperature of the $^9Be^+$ ions. This indicates that a large fraction of the $^9Be^+$ ions has already been lost by the chemical reaction $Be^+ + H_2 \rightarrow BeH^+ + H$ [109].

Fig. 5.7 shows a qualitative explanation of the fluorescence signal shape in terms of the *effective* trap frequency ω_{eff} and the temperatures T_{Be} and T_{N} of the $^9Be^+$ and $^{14}N^+$ ions, respectively. In particular, ω_{eff} is the transverse trap frequency

of the $^{14}N^+$ ions in the superposition of the time-averaged trap potential and the space charge potential of the Be^+ and BeH^+ ions (→ Sect. 2.3.1). At the start of the excitation frequency scan, ω_{eff} is shifted well below the nominal trap frequency $\omega_{r(\text{N})}$ [Eq. 5.3]. As a rough estimate, a shift of $(\omega_{r(\text{N})} - \omega_{\text{eff}})/2\pi \approx 30\,\text{kHz}$ is calculated from Eq. (2.12) for a total number of 3000 ions with an average mass of $m/z = 9.5$ ($^9Be^+$ and BeH^+) and a temperature of 30 K. As the excitation frequency ω_{exc} approaches the *effective* trap frequency ω_{eff}, a negative feedback is established as described under case I in Sect. 2.3.2. As a result, the *effective* trap frequency ω_{eff} is locked to the excitation frequency ω_{exc} and both temperatures T_{Be} and T_{N} start to rise. As the excitation frequency ω_{exc} approaches the nominal trap frequency $\omega_{r(\text{N})}$ [Eq. (5.3)] (dotted vertical line in Fig. 5.7), the $^{14}N^+$ ions are decoupled from the kinetic excitation since ω_{eff} can not increase anymore. Thus, in contrast to the numerical solution shown in Fig. 2.4 of Sect. 2.3.2, the $^{14}N^+$ ions are sympathetically cooled once more by the laser-cooled $^9Be^+$ ions, rather than being decoupled from the $^9Be^+$ ions. This can be inferred from the fluorescence signal in Fig. 5.6 which at the end of the excitation frequency scan again reaches its initial level.

5.3.2 Experimental Results: II. $^4He^+$

Fig. 5.8 shows a LCF-MS mass spectrum of sympathetically cooled $^4He^+$ ions, obtained from an upward excitation frequency scan. The complete scan ranging from $\omega_{\text{exc}}/2\pi = 400\,\text{kHz}$ to 1.2 MHz was performed within 100 s and with an excitation amplitude of $U_{\text{exc}} = 1\,\text{V}$. The linear rf trap was operated at $U_{\text{RF}} = 380\,\text{V}$ and $U_{\text{EC}} = 3\,\text{V}$. Preparation of the trapped ion cloud included the following steps. First, the trap was loaded with $^9Be^+$ ions while neutral He gas was introduced through a leak valve into the vacuum chamber up to a pressure of $P = 7 \cdot 10^{-10}\,\text{mbar}$. Right after completing the loading process, the cooling laser was locked to an I_2 hyperfine transition (→ Sect. 4.3.1) and fine-adjusted a few 10 MHz below the cooling transition frequency by maximizing the fluorescence of the $^9Be^+$ ions. No further cooling of the trapped ion cloud nor any reduction of the total number of trapped ions was performed. Thus, a large ion cloud with a temperature of $T \gg 10\,\text{K}$ (→ Sect. 6.2) was expected to be confined in the trap. This agrees well with the measured fluorescence signal in Fig. 5.8 which is rather low, indicating an increased temperature of the $^9Be^+$ ions and a large fraction of additionally trapped impurity ions. Before obtaining the LCF-MS mass spectrum, the transverse trap frequency of the $^9Be^+$ ions was determined as $\omega_{r(\text{Be})}/2\pi = 280\,\text{kHz}$ (→ Sect. 5.2). From this, a mass scale was established by use of Eq. (5.3) which is shown on the upper horizontal axis in Fig. 5.8.

In Fig. 5.8, an almost step-like increases in fluorescence signal occurs at $\omega_{\text{exc}}/2\pi = 628\,\text{kHz}$, corresponding to mass $m/z = 4\,\text{u}$ on the upper mass scale, i.e. the mass of the $^4He^+$ ion. Furthermore, a small gradual drop precedes the step-like increase which then is followed by a second gradual drop. Thus, the fluorescence signal shape considerably differs from the characteristic asymmetric dip shown in the previous section.

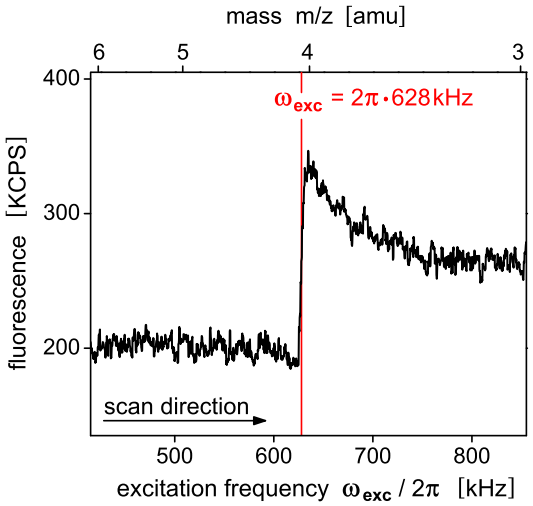

Figure 5.8: *LCF-MS mass spectrum, showing the presence of sympathetically cooled $^4He^+$ ions.*

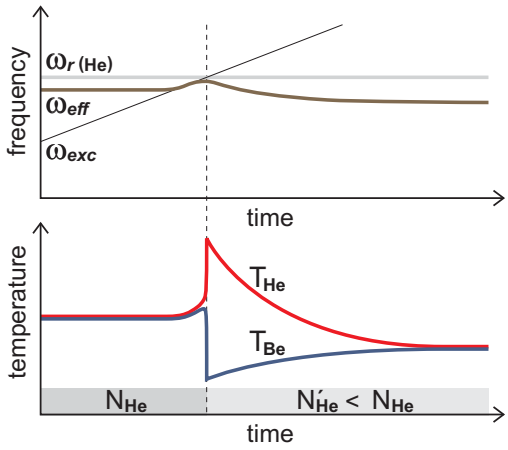

Figure 5.9: *Supposed change in time of ω_{eff}, T_{LC}, and T_{SC}, drawn in a qualitative fashion in the style of Ref. [54].*

Fig. 5.9 shows a qualitative explanation of the fluorescence signal shape in terms of the *effective* trap frequency ω_{eff} and the temperatures T_{Be} and T_{He} of the $^9Be^+$ and $^4He^+$ ions, respectively. In particular, ω_{eff} is the transverse trap frequency of the $^4He^+$ ions in the superposition of the time-averaged trap potential and the space charge potential of the $^9Be^+$ ions (→ Sect. 2.3.1). Accordingly, at the start of the excitation frequency scan, ω_{eff} is only slightly shifted with respect to the nominal trap frequency $\omega_{r(\text{He})}$ [Eq. (5.3)] due to the increased temperature of the trapped ion cloud. As a result, negative feedback which more or less locks ω_{eff} to the excitation frequency ω_{exc}, as explained under case I in Sect. 2.3.2, only occurs over a small frequency range. The corresponding increase in temperatures T_{Be} and T_{He} therefore is also small. This explains the first small gradual drop in fluorescence in Fig. 5.8. However, as the excitation frequency ω_{exc} reaches the nominal trap frequency $\omega_{r(\text{He})}$ [Eq. (5.3)] (dotted vertical line in Fig. 5.9), the difference in temperature between T_{He} and T_{Be} has become sufficiently large in order to decouple the $^4He^+$ from the $^9Be^+$ ions. As a result, the $^9Be^+$ ions are quickly cooled down, giving rise to a strong step-like increase in fluorescence in Fig. 5.8. On the other hand, the $^4He^+$ ions are exposed to strong, almost undamped kinetic excitation as described under case I in Sect. 2.3.2. In Fig. 5.8, a second gradual drop in fluorescence occurs right after the step-like increase. Obviously, the $^4He^+$ ions are once more sympathetically cooled by the laser-cooled $^9Be^+$ ions, resulting in a gradual increase in temperature T_{Be} of the $^9Be^+$ ions. The new equilibrium is reached at a lower temperature as compared to the start of the excitation frequency scan. This can be seen from the increase in fluorescence signal in Fig. 5.8 by almost 75% after the excitation frequency ω_{exc} has been scanned across the resonance. A certain fraction of $^4He^+$ ions must have been lost from the trap, which significantly reduces rf heating. In Fig. 5.9, this is indicated by the labels N_{He} and N'_{He} on the lower horizontal axis, denoting the total numbers of $^4He^+$ ions at the start and end of the excitation frequency scan.

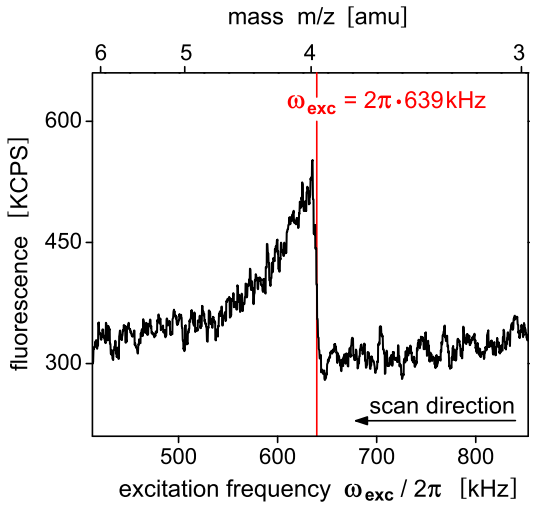

Figure 5.10: *LCF-MS mass spectrum of sympathetically cooled $^4He^+$ ions, similar to Fig. 5.8, however with the scan direction reversed.*

In order to test this explanation, a further LCF-MS mass spectrum was obtained in an experiment similar to that described above, however with the scan direction reversed. This is shown in Fig. 5.10. The complete scan ranging from $\omega_{\rm exc}/2\pi = 1.2\,$MHz down to 400 kHz was performed within 100 s and with an excitation amplitude of $U_{\rm exc} = 0.5\,$V. Again, a step-like increase in fluorescence at mass $m/z = 4\,$u is followed by a gradual drop, however this time reversed with respect to the frequency axis. The gradual drop being attributed to the sympathetic cooling of the $^4He^+$ ions, after their strong excitation at the nominal trap frequency $\omega_{r(\rm SC)}$ [Eq. (5.2)], occurs on the same time scale ($\approx 10\,$s) as in Fig. 5.8. However, in contrast to Fig. 5.8, the fluorescence finally drops to its initial level, indicating that no significant amount of $^4He^+$ ions was lost from the trap.

In summary, both LCF-MS mass spectra shown in Figs. 5.8 and 5.10 mainly reflect a *temporary decoupling* of the sympathetically cooled $^4He^+$ ions from the laser-cooled $^9Be^+$ ions. However, while in the upward excitation frequency scan (Fig. 5.8), a significant loss of $^4He^+$ ions was observed, no such loss was observed in the downward excitation frequency scan (Fig. 5.10). This proves consistent with the predictions of the simplified model of LCF-MS (→ Sect. 2.3.2).

5.3.3 Experimental Results: III. HD^+ & D^+

Fig. 5.11 shows a LCF-MS mass spectrum of sympathetically cooled HD^+ ions, obtained from an upward excitation frequency scan. The complete scan ranging from $\omega_{\rm exc}/2\pi = 600\,$kHz to 1.2 MHz was performed within 100 s and with an excitation amplitude of $U_{\rm exc} = 10\,$V. The linear rf trap was operated at $U_{\rm RF} = 380\,$V and $U_{\rm EC} = 3\,$V. Preparation of the trapped ion cloud included the following steps. First, the trap was loaded with HD^+ ions by introducing neutral HD gas through

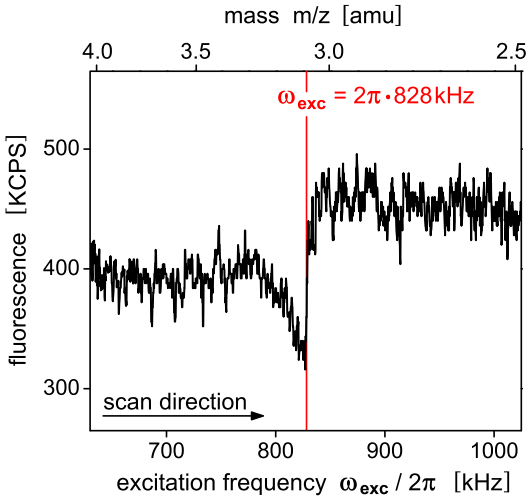

Figure 5.11: *LCF-MS mass spectrum, showing the presence of sympathetically cooled HD^+ ions.*

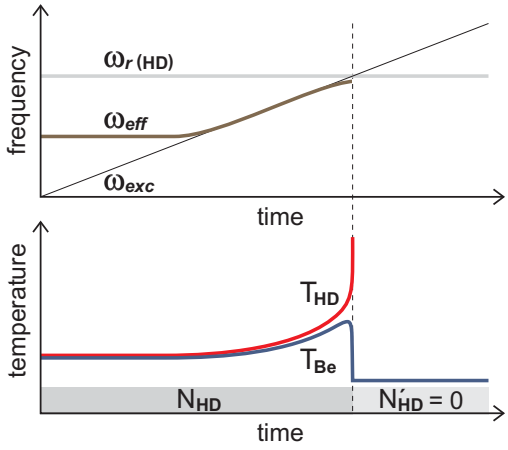

Figure 5.12: *Supposed change in time of ω_{eff}, T_{LC}, and T_{SC}, drawn in a qualitative fashion in the style of Ref. [54].*

a leak valve into the vacuum chamber up to a pressure of $P = 1 \cdot 10^{-9}$ mbar, and switching on the electron gun (→ Sect. 3.1). Then, the leak valve was closed and the Be oven switched on, thus loading the trap with $^9Be^+$ ions as well. This two-step loading process was employed in order to reduce the losses of $^9Be^+$ ions by the chemical reactions $Be^+ + HD \rightarrow BeH^+ + D$ and $Be^+ + HD \rightarrow BeD^+ + H$ with the neutral HD gas [109]. Finally, the cooling laser was locked to an I_2 hyperfine transition (→ Sect. 4.3.1) and fine-adjusted a few 10 MHz below the cooling transition frequency by maximizing the fluorescence of the $^9Be^+$ ions. No further cooling of the trapped ion cloud nor any reduction of the total number of trapped ions was performed. Thus, a large ion cloud with a temperature of $T \gg 10$ K (→ Sect. 6.2) was expected to be confined in the trap. This agrees well with the measured fluorescence signal in Fig. 5.11 which is rather low, indicating an increased temperature of the $^9Be^+$ ions and a large fraction of additionally trapped impurity ions. Before obtaining the LCF-MS mass spectrum, the transverse trap frequency of the $^9Be^+$ ions was determined as $\omega_{r(Be)}/2\pi = 280$ kHz (→ Sect. 5.2). From this, a mass scale was established by use of Eq. (5.3) which is shown on the upper horizontal axis in Fig. 5.11.

In Fig. 5.11, the fluorescence signal shows the same qualitative features as the numerical solution in Fig. 2.4 of Sect. 2.3.2. In particular, a gradual decrease in fluorescence signal is followed by a step-like increase in the upward excitation frequency scan. According to Fig. 2.4, the step-like increase is expected to occur at the nominal trap frequency (5.3) of the sympathetically cooled ions. This agrees well with Fig. 5.11 where the step-like increase occurs at $\omega_{exc}/2\pi = 828$ kHz, corresponding to mass $m/z = 3$ u of the HD^+ ion. Furthermore, in both Fig. 2.4 and Fig. 5.11, the fluorescence finally settles at a higher level as compared to the start of the excitation frequency scan. Finally, it should be noted that the excitation amplitude $U_{exc} = 10$ V had to be strongly increased as compared to the scans of the

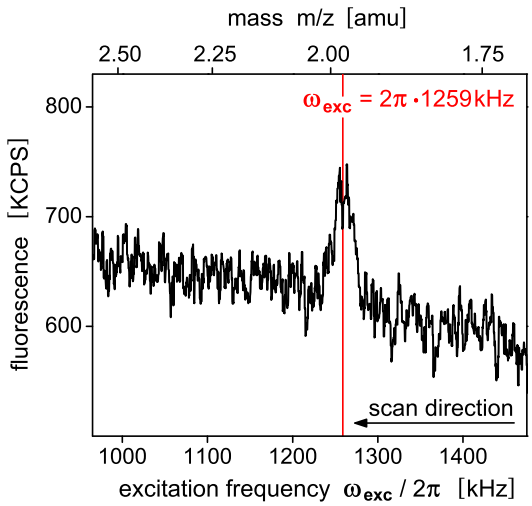

Figure 5.13: *LCF-MS mass spectrum, showing the presence of sympathetically cooled D^+ ions, obtained from a downward excitation frequency scan. The fluorescence signal shape mainly reflects a temporary decoupling of the D^+ ions from the laser-cooled $^9Be^+$ ions.*

previous sections in order to see any response in fluorescence at all. This may be explained by the small number of HD^+ ions which are well shielded[a] by the $^9Be^+$, BeH^+, and BeD^+ ions.

Fig. 5.12 shows a qualitative explanation of the fluorescence signal shape in terms of the *effective* trap frequency ω_{eff} and the temperatures T_{Be} and T_{HD} of the $^9Be^+$ and HD^+ ions, respectively. In particular, ω_{eff} is the transverse trap frequency of the HD^+ ions in the superposition of the time-averaged trap potential and the space charge potential of the Be^+, BeH^+, and BeD^+ ions (→ Sect. 2.3.1). Due to the large ion number, ω_{eff} is expected to be shifted well below the nominal trap frequency $\omega_{r(\text{HD})}$ [Eq. (5.3)], despite the increased temperature of the trapped ion cloud. As a rough estimate, a shift of $(\omega_{r(\text{HD})}-\omega_{\text{eff}})/2\pi \approx 20\,\text{kHz}$ is calculated from Eq. (2.12) for a total number of 10000 ions with an average mass of $m/z=10$ (Be^+, BeH^+, and BeD^+) and a temperature of 100 K. As the excitation frequency ω_{exc} approaches the *effective* trap frequency ω_{eff}, the latter becomes locked to the first by the negative feedback mechanism described under case I in Sect. 2.3.2. This results in a gradual increase in both temperatures T_{Be} and T_{HD} of the $^9Be^+$ and HD^+ ions, respectively. Next, as the excitation frequency ω_{exc} approaches the nominal trap frequency $\omega_{r(\text{HD})}$ [Eq. (5.3)] (dotted vertical line in Fig. 5.12), the difference in temperature between T_{Be} and T_{HD} has become sufficiently large in order to decouple the HD^+ from the $^9Be^+$ ions. As a result, the $^9Be^+$ ions are quickly cooled down while the HD^+ ions are exposed to strong, almost undamped kinetic excitation as described under case I in Sect. 2.3.2. In Fig. 5.12, complete loss of the HD^+ ions from the trap is assumed as indicated by the abrupt ending of the theoretical curves for

[a] Radial confinement by the time-averaged trap potential (2.3) increases with decreasing mass-to-charge ratio m/z. Thus, the HD^+ plus ions are pushed towards the trap axis much stronger than the $^9Be^+$, BeH^+, and BeD^+ ions.

ω_{eff} and T_{HD}. Finally, reduced rf heating due to the loss of the HD^+ ions decreases the temperature T_{Be} of the $^9Be^+$ ions as compared to the start of the excitation frequency scan. This can be inferred from the fluorescence signal in Fig. 5.11 which at the the end of the excitation frequency scan noticeably increases above its initial level.

In order to complete the investigations, a downward excitation frequency scan was performed on a trapped ion cloud, prepared similar to that in Fig. 5.11. This is shown in Fig. 5.13. The complete scan ranging from $\omega_{\text{exc}}/2\pi = 1.5\,\text{MHz}$ down to 700 kHz was performed within 100 s and with an excitation amplitude of $U_{\text{exc}} = 1\,\text{V}$. The trap was operated at $U_{\text{RF}} = 380\,\text{V}$ and $U_{\text{EC}} = 3\,\text{V}$. The mass scale on the upper horizontal axis was established by use of Eq. (5.3) after the transverse trap frequency of the $^9Be^+$ ions had been determined as $\omega_{r(\text{Be})}/2\pi = 273\,\text{kHz}$ ($\rightarrow$ Sect. 5.2). A small but distinct peak appears in the fluorescence signal at $\omega_{\text{exc}}/2\pi = 1259\,\text{kHz}$, corresponding to mass $m/z = 2$ on the upper mass scale. This is attributed to the D^+ atomic ion, produced by electron-impact dissociation of the trapped HD^+ ions. The fluorescence signal shape indicates a temporary decoupling of the sympathetically cooled D^+ ions from the laser-cooled $^9Be^+$ ions, similar to that in Fig. 5.10. However, the asymmetric feature seems to be "washed out" due to the small relative peak height.

Chapter 6

$^9Be^+$ Ion Crystals

The $^9Be^+$ ion crystals which will be presented in this chapter are examples of ion Coulomb crystals, prepared by laser-cooling of a single-species of trapped atomic ions (→ Sect. 1.2). Typical ion densities are $10^7 - 10^9/cm^3$, depending on the strength of the particular confining potential. Typical temperatures are in the milli-Kelvin range. Coulomb crystals of laser-cooled atomic ions for the first time were observed in hyperbolic rf (Paul) traps [32,33], followed by quadrupole rf storage rings [34,35] and Penning traps [36,37]. The first observation of a Coulomb crystal in a linear rf (Paul) trap was reported in Ref. [113]. Among various applications of single-species ion Coulomb crystals, frequency standards [38] shall be noted here, as well as possible implementations of quantum gates and memories for quantum computing [39]. Furthermore, implementation of a quantum computer by a string of trapped ions has been suggested in Refs. [40,41].

The present chapter is organized as follows. In **Sect. 6.1**, a general description will be given of the thermal equilibrium states of a single-species plasma of *finite* size. This will also include a description of the continuous transition to the crystalline state which contrasts with the abrupt phase transition, predicted for the *infinite* OCP (→ Sect. 2.2.1). In **Sect. 6.2**, the temperature T, plasma coupling parameter Γ (2.5), and the Debye length λ_D (2.4) of laser-cooled $^9Be^+$ ions in the cloud-like and the crystalline state will be estimated by fits of Voigt profiles to the measured fluorescence signal. Finally, in **Sect. 6.3**, the outer shape of different-sized $^9Be^+$ ion crystals in a fully anisotropic confining potential will be compared with the predictions of the charged fluid model (→ Sect. 2.2.2).

6.1 Transition to the Crystallized State

The $^9Be^+$ ion crystals presented in this chapter are, besides from a few exceptions, of comparable size corresponding to a total number of $^9Be^+$ ions in the range between $500 \lesssim N \lesssim 2000$. Thus, the $^9Be^+$ ion crystals are large enough in

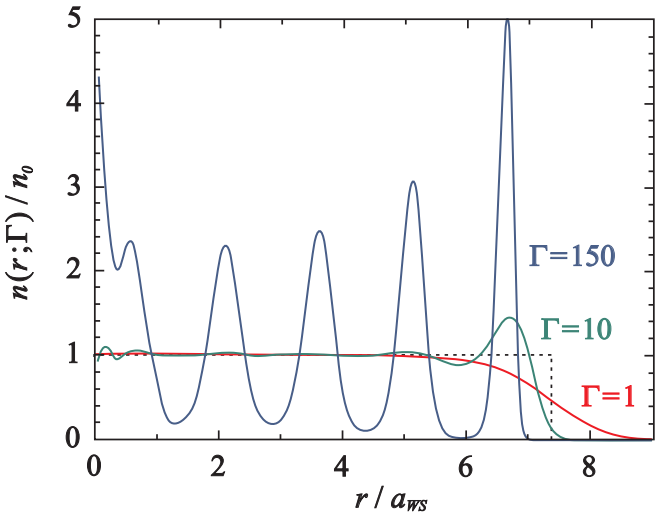

Figure 6.1: *Thermal equilibrium ion densities $n(r;\Gamma)$, plotted as a function of the spherical radius r for three different values of the plasma coupling parameter Γ [Eq. (2.5)]. Based on a Monte Carlo simulation, the densities $n(r;\Gamma)$ were obtained from averages over the Gibb's distribution (canonical ensemble) of a single-species plasma of $N = 400$ ions, confined in a spherically symmetric 3-D harmonic potential. The ion densities are normalized with respect to the constant density n_0 [Eq. (2.6)], expected in the limit $\Gamma \to \infty$. A dotted line indicates the theoretical shape of the ion density in this limit: the confining potential is filled with a charged fluid of constant density n_0 up to a spherical radius of $r/a_{WS} = N^{1/3}$, where r is measured in units of the Wigner Seitz radius $a_{WS} = (3/4\pi n_0)^{1/3}$. Note: the graphical representation has been slightly changed with respect to Ref. [114] from which this plot was taken.*

order to meaningfully assign a continuous, average ion density $n(\boldsymbol{r})$ as well as a gross outer shape to them, which then can be compared with the charged fluid model (→ Sect. 2.2.2). On the other hand, the crystals are sufficiently small so that the lattice structure within the crystal still strongly depends on the size and outer crystal shape, i.e. the total number of ions N and the applied trap potential $\phi_{\text{trap}}(\boldsymbol{r})$. In Ref. [60], plasmas with a total number of ions $10^2 \lesssim N \lesssim 10^4$ and the above characteristics are referred to as *mesoscopic* plasmas, in distinction from *large* plasmas whose interiors exhibit a bcc lattice structure as predicted by the OCP model (→ Sect. 2.2.1), and *Coulomb clusters* with $N \lesssim 10$. This terminology will be adopted in the remainder of this chapter. Thus, the first two of the "purified" $^9Be^+$ ion crystals which will be shown in Sect. 6.3 are, besides from a few additionally trapped impurity ions, examples of *mesoscopic single-species plasmas*. Furthermore, since the confinement provided by the linear rf trap is adequately described in terms of a time-averaged 3-D harmonic potential (→ Sect. 2.1), the $^9Be^+$ crystals may also be regarded as laboratory realizations of *finite* OCPs (→ Sect. 2.2.1).

In contrast to the *infinite* OCP, the nature of the thermal equilibrium state of a mesoscopic single-species plasma is not solely determined by the plasma coupling parameter Γ [Eq. (2.5)], but also depends on the plasma size and shape. With the smallest of the spatial dimensions of the plasma denoted by R_p, and the Debye length λ_D defined by Eq. (2.4), three limiting cases can be distinguished concerning

the spatial distribution of ions in the thermal equilibrium state. In the following, these limiting cases are described in the order of a decreasing temperature T, where a 3-D harmonic trap potential $\phi_{\text{trap}}(\boldsymbol{r})$ with trap frequencies ω_x, ω_y, and ω_z is assumed. The descriptions may be compared with Fig. 6.1, taken from Ref. [114], which shows the calculated ion densities $n(r;\Gamma)$ of a cloud of $N=400$ ions, confined in a spherically symmetric 3-D harmonic potential. The ion densities are plotted as a function of the spherical radius r for different values of Γ.

I. $\Gamma \ll 1$ and $\lambda_D \gg R_p$ (Cloud of noninteracting ions)

In the high-temperature limit, the Debye length λ_D is large compared to the smallest plasma dimension R_p. Accordingly, no Debye shielding of the trap potential $\phi_{\text{trap}}(\boldsymbol{r})$ takes place ($\rightarrow$ Sect. 2.2.1), i.e. the modification of $\phi_{\text{trap}}(\boldsymbol{r})$ by the space charge of the trapped ions is negligibly small. In consequence, the average ion density is given by the thermal equilibrium distribution $n(\boldsymbol{r}) \propto \exp[-Q\phi_{\text{trap}}(\boldsymbol{r})/k_B T]$ of an ensemble of noninteracting particles with charge Q in the presence of an externally applied electrostatic trap potential $\phi_{\text{trap}}(\boldsymbol{r})$ [a] [115]. Since $\phi_{\text{trap}}(\boldsymbol{r})$ is assumed to be 3-D harmonic, $n(\boldsymbol{r})$ has a Gaussian dependence on the spatial coordinates x, y, and z, with spatial extensions in the x, y, and z-direction which are inversely proportional to the respective trap frequencies ω_x, ω_y, and ω_z. This was confirmed experimentally by measurements of the density profiles of hot ($T \approx 10^4$ K) ion clouds, confined in hyperbolic rf (Paul) traps [116,117]. According to the criterion that a plasma has to be large in all its dimensions compared to the Debye length λ_D, in order to be designated as a *plasma* ($\rightarrow$ Sect. 2.2.1), the Gaussian density distribution $n(\boldsymbol{r})$ does not represent a plasma but rather a cloud of noninteracting ions.

II. $\Gamma \ll 1$ and $\lambda_D \ll R_p$ (Constant density plasma)

If the Debye length λ_D decreases below the smallest dimension R_p of the still weakly correlated plasma, Debye shielding of the trap potential $\phi_{\text{trap}}(\boldsymbol{r})$ takes place. In other words, $\phi_{\text{trap}}(\boldsymbol{r})$ is substantially modified by the space charge of the trapped ions. Since the plasma is weakly correlated, correlations between individual ions can be neglected and the interaction between the ions is adequately described as a collective interaction by the space charge potential. Thus, the charged fluid model applies ($\rightarrow$ Sect. 2.2.2), according to which the ion density $n(\boldsymbol{r})$ is nearly constant up to the outer plasma boundary and there drops to zero on the scale of the Debye length λ_D. In the limit $\lambda_D \ll R_p$, the ion density $n(\boldsymbol{r})$ therefore is constant all over the plasma and equal to the density of the neutralizing background charge $n_0 = (\epsilon_0/Q)\Delta\phi_{\text{trap}}(\boldsymbol{r})$, provided by the 3-D harmonic potential $\phi_{\text{trap}}(\boldsymbol{r})$, besides from a surface sheath of negligible thickness λ_D. In contrast to case I where $n(\boldsymbol{r})$ has a Gaussian dependence on the spatial coordinates x, y, and z, the outer plasma boundary

[a] $\phi_{\text{trap}}(\boldsymbol{r})$ designates an electrostatic potential in the sense that the force acting on a particle with charge Q is given by $\boldsymbol{F} = -Q\nabla\phi_{\text{trap}}(\boldsymbol{r})$. Of course, $\phi_{\text{trap}}(\boldsymbol{r})$ is not an electrostatic potentials in a true sense since it does not obey Laplace's equation $\Delta\phi(\boldsymbol{r}) = 0$.

is well defined, with spatial extensions in the x, y, and z-direction which exhibit a non-trivial dependence on the respective trap frequencies ω_x, ω_y, and ω_z ($\rightarrow$ Sect. 2.2.2).

III. $\Gamma \gg 1$ and $\lambda_D \ll R_p$ (Coulomb crystal)

When the plasma enters the strong correlation regime, correlations between the individual ions can not be neglected anymore. Thus, the charged fluid description has to be replaced in favor of an appropriate N-particle description, which turns out to be given by the canonical ensemble [60]. Accordingly, the average ion density $n(\boldsymbol{r})$ and the outer plasma shape are still correctly predicted by the charged fluid model in the limit $\lambda_D \ll R_p$. However, the correlations establish order within the region of constant density $n(\boldsymbol{r}) = n_0$. As was shown by molecular dynamics (MD) simulations [118] as well as experimental observations [42], the transition to the crystalline state in a mesoscopic single-species plasma is a continuous transition which proceeds as follows. First, at $\Gamma \gtrsim 1$, a shell structure develops where ions still randomly move within the shells, then a lattice structure on the shells forms. Finally, in the limit $\Gamma \rightarrow \infty$, the plasma completely crystallizes, i.e. every ion settles into a fixed position. In this limit, the Debye length λ_D decreases to a value even below the interparticle spacing and therefore looses its meaning as an effective measure of the distance within which Debye shielding takes place.

The occurrence of a weakly correlated plasma with a constant density, as described under case II, implies a Debye length λ_D which is much smaller than the smallest plasma dimension R_p. This in turn requires a total number of ions which is sufficiently large. In case of the $^9Be^+$ ion crystals presented in Sect. 6.3, which contain not more than $N \lesssim 2000$ $^9Be^+$ ions, the plasma already has entered the strong correlation regime when λ_D finally decreases to a value much smaller than R_p. Accordingly, in the weak correlation regime which precedes the crystalline state, Debye shielding of the trap potential only takes place to a certain extent. The density distribution of the $^9Be^+$ ions in the weak correlation regime therefore can be expected to already depart from a Gaussian distribution but still be far from a constant density distribution.

According to the description of the formation process of a crystal structure in a strongly correlated plasma, as given under case III, a fundamental difference exists between a *finite*, mesoscopic single-species plasma and the *infinite* OCP ($\rightarrow$ Sect. 2.2.1). In the infinite OCP, the nature of the thermal equilibrium state is solely determined by the plasma coupling parameter Γ [Eq. (2.5)]. In particular, a phase transition to a crystalline state with a bcc lattice structure takes place at $\Gamma \approx 170$. In contrast to this, in a mesoscopic single-species plasma, no abrupt phase transition to a crystalline state takes place, but instead, with increasing $\Gamma \gtrsim 1$, a continuous transition to a crystalline state occurs. The transition covers a wide variety of intermediate states with different degree of crystallization whose structures (as well as that of the final, completely crystallized state reached in the limit $\Gamma \rightarrow \infty$) strongly depends on the plasma size and shape. This was already noted at the beginning of this section where the term *mesoscopic* was introduced.

In Ref. [118], results are shown from MD simulations of spherical clouds of $N = 100$ and 256 ions, confined in a Penning trap. Accordingly, for $\Gamma = 2-100$, the ion density as a function of the spherical radius is observed to exhibit oscillations, indicating the partition of the ion cloud into concentric shells. At $\Gamma \approx 140$ ($N = 100$) the shells are completely separated. With further increasing the value of Γ, correlations between the ions on a given shell show up and further increase, thus indicating the formation of a (2-D hexagonal) lattice structure on the shells. However, no abrupt transition to long-range order on the shells, i.e. to a completely crystalline state is observed, but instead, diffusion of ions within the shells is shown to still occur at $\Gamma = 300-400$. This description of the continuous formation process of a crystal structure in a mesoscopic single-species plasma agrees well with the observations made in this work, concerning the order in which the crystal structure develops. A detailed investigation of the formation process of a crystal structure in mesoscopic $^{24}Mg^+$ ion plasmas confined in a linear rf (Paul) trap is found in Ref. [42].

MD simulations are also ideally suited for a systematic study of the lattice structure of completely crystallized single-species as well as multi-species plasmas, obtained in the limit $\Gamma \to \infty$ [31,48,118–122]. In Ref. [31], results are shown from MD simulations of infinitely long ion crystals, confined in a cylindrically symmetric 2-D harmonic potential, intended as a first approximation to ion storage rings. Depending on a dimensionless linear number density λ, defined as the number of ions per unit length and used as a parameter in the MD simulations, the ions arranged as: 1-D strings, zigzag-structures, helices, and finally, for sufficiently large values of λ, multishell structures. In each case, the completely crystalline state, i.e. all ions settled at a fixed position, was typically reached at $\Gamma = 2000-20\,000$. A comparison of the crystal structures, as predicted for a certain range of λ, with the observed crystal structures of highly prolate, spheroidal shaped $^{24}Mg^+$ ion crystals in a linear rf trap is found in Ref. [69]. An excellent agreement is reported.

Finally, it should be noted that for *real* single-species plasmas, like the $^9Be^+$ ion crystals which will be presented in Sect. 6.3, the degree of crystallization and the spatial arrangement of ions also depends on the amount of additionally trapped impurity ions as well as other imperfections, e.g., static electric stray potentials.

6.2 Temperature Determination from the Fluorescence Signal of the $^9Be^+$ Ions

For the measurements described in this section, the trap parameters were $\Omega/2\pi = 14.2\,\text{MHz}$, $U_{\text{RF}} = 380\,\text{V}$, and $U_{\text{EC}} = 3\,\text{V}$, which according to Eqs. (2.3b–d) result in a transverse trap frequency of $\omega_r/2\pi = 271\,\text{kHz}$ ($\omega_r \stackrel{\text{def}}{=} \omega_x = \omega_y$) and an axial trap frequency of $\omega_z/2\pi = 69.7\,\text{kHz}$. The trap was loaded with $^9Be^+$ ions by evaporating Be atoms from a small oven and ionizing them in the trap center by electron impact (→ Sect. 3.2). Without any cooling, the temperature of a trapped ion cloud

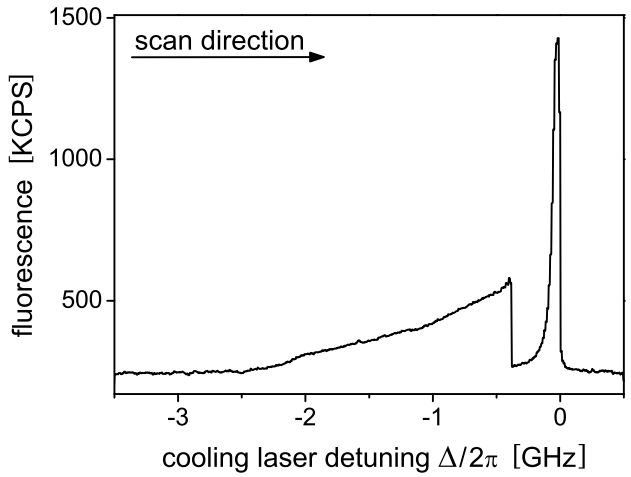

Figure 6.2: *Fluorescence signal of a total number of $N \approx 3000$ $^9Be^+$ ions, measured in units of 10^3 Counts/s (KCPS) and plotted as a function of the cooling laser detuning. At $\Delta_{dip}/2\pi \approx -0.4$ GHz, a sudden drop of the fluorescence signal occurs, indicating a corresponding temperature drop of the $^9Be^+$ ions. The laser frequency was scanned over a total range of 5 GHz within a time of 50 s.*

in a rf (Paul) trap is mainly determined by rf heating and after a few minutes adjusts at a typical value in the range between 10^3 and 10^4 K [116,123]. Accordingly, in order to effectively cool the $^9Be^+$ ions, the 313 nm cooling laser had to be scanned over a large frequency range with a starting frequency red-detuned by several GHz from the center frequency of the $^2S_{1/2} \leftrightarrow {}^2P_{3/2}$ cooling transition. Care was taken to achieve a maximum degree of σ^+ polarization which together with a weak magnetic field parallel to the trap axis (→ Sect. 3.1) ensured the $^9Be^+$ ions to exclusively cycle between the $^2S_{1/2}(F=2, m_F=2)$ ground and the $^2P_{3/2}(F=3, m_F=3)$ excited state (natural linewidth $\gamma/2\pi = 19.4$ MHz and saturation intensity $I_{\rm sat} = 0.83\,{\rm mW/mm^2}$ [88]). The fluorescence of the $^9Be^+$ ions was measured with a photomultiplier tube (PMT), mounted transverse to the trap axis (→ Sect. 3.4).

Fig. 6.2 shows the fluorescence signal of a total number of $N \approx 3000$ $^9Be^+$ ions as a function of the cooling laser detuning $\Delta \stackrel{\rm def}{=} \omega_L - \omega_A$, where ω_L denotes the laser frequency and $\omega_A = 2\pi c/\lambda_A$ the frequency of the $^2S_{1/2} \leftrightarrow {}^2P_{3/2}$ cooling transition. The laser frequency was scanned with a rate of 0.1 GHz/s, starting from an initial red-detuning of $\Delta/2\pi = -5$ GHz. The laser beam was collimated to a beam radius of $w \approx 0.7$ mm with a power of $P = 8$ mW, corresponding to an average intensity of $P/\pi w^2 = 6.3\, I_{\rm sat}$ and a maximum intensity of $2P/\pi w^2 = 12.5\, I_{\rm sat}$ in the center of the Gaussian beam profile. In order to prevent 313 nm stray light from reaching the PMT, careful spatial filtering was performed, using blackened stainless steel baffles (→ Sect. 3.1). However, still some stray light reached the PMT, showing up in Fig. 6.2 as a background signal of approximately 250 KCPS.

As the cooling laser detuning reduces to $\Delta/2\pi \approx -2.5$ GHz, the fluorescence signal in Fig. 6.2 starts to continuously rise above the background level, until at $\Delta_{\rm dip}/2\pi \approx -0.4$ GHz, a sudden drop of the fluorescence signal occurs. This usually

is referred to as the *fluorescence dip*. The fluorescence dip is followed by a steep rise of the fluorescence signal up to a maximum value of approximately 1430 KCPS at zero cooling laser detuning $\Delta = 0$. Finally, for positive cooling laser detuning $\Delta > 0$, the fluorescence signal almost instantly drops back to the background level. This characteristic behavior may be explained in terms of a competition between laser cooling and rf heating which causes the temperature of the laser-cooled ions to permanently change during the laser frequency scan [54,124]. Accordingly, for $\Delta < \Delta_{\rm dip} < 0$ the temperature of the laser-cooled ions is determined by a balance between laser cooling and rf heating, whereas for $\Delta_{\rm dip} < \Delta < 0$, laser cooling overcomes rf heating, resulting in a sudden temperature drop at $\Delta = \Delta_{\rm dip}$. Since this temperature drop is connected with a reduction of Doppler broadening, the fluorescence signal line profile at $\Delta = \Delta_{\rm dip}$ abruptly changes from a Doppler broadened to a very narrow one, with a width in the order of the natural linewidth. Finally, for positive detuning $\Delta > 0$, laser cooling turns into heating which (together with rf heating) results in a rapid rise of the temperature of the laser-cooled ions, causing an almost instant drop of the fluorescence signal.

In support of this explanation, the main features of the measured fluorescence signal shown in Fig. 6.2, i.e. the fluorescence dip and the narrowing of the fluorescence signal line profile, can be reproduced by means of the rate equation (2.13) ($\rightarrow$ Sect. 2.3.2). To this end, $N_{\rm SC}$ in Eq. (2.13) has to be set to zero in order to adapt to the case of no sympathetically cooled ions. In this case, Eq. (2.13) simply equates the change in time of the mean kinetic energy $W_{\rm LC}$ of the laser-cooled ions with the sum of the laser-cooling rate $[\Delta W_{\rm LC}/\Delta t]_{\rm LC}$ and the rf-heating rate $[\Delta W_{\rm LC}/\Delta t]_{\rm rfh}$. From the numerical solution $W_{\rm LC}(t)$, obtained for a given set of parameters concerning the linear rf trap, cooling laser, and laser-cooled ions, the mean photon scattering rate $\bar{\Gamma}_{\rm ph}[\Delta; W_{\rm LC}(\Delta), I]$ (see below) can be calculated and plotted as a function of the cooling laser detuning $\Delta = R_{\rm scan} \cdot t$. This was done in Ref. [54] for two different values of the rf amplitude $U_{\rm RF}$, i.e. two different rf heating rates: while in a first plot, a fluorescence dip connected with a narrowing of the fluorescence signal line profile occurred, no such dip occurred in a second plot in which $U_{\rm RF}$ was slightly increased.

In order to estimate the temperature T of the laser-cooled $^9Be^+$ ions from the measured fluorescence signal, the following expression is used for the mean photon scattering rate $\bar{\Gamma}_{\rm ph}$ (per laser-cooled ion) which will be derived in appendix B:

$$\bar{\Gamma}_{\rm ph}(\Delta; T, I) \;=\; \frac{(I/I_{\rm sat})\gamma^3}{8} \sqrt{\frac{m}{2\pi k_B T}} \int_{-\infty}^{+\infty} dv \, \frac{\exp[-mv^2/2k_B T]}{(\Delta - k_A v)^2 + (1 + I/I_{\rm sat})\gamma^2/4} \qquad (6.1)$$

Thus, when viewed as a function of the cooling laser detuning Δ, the mean photon scattering rate $\bar{\Gamma}_{\rm ph}$ is a Voigt profile, accounting for Doppler as well as power and natural broadening. Additional parameters in $\bar{\Gamma}_{\rm ph}(\Delta; T, I)$ are the temperature T and the laser intensity I. For the laser-cooled $^9Be^+$ ions, $I_{\rm sat} = 0.83\,{\rm mW/mm^2}$, $\gamma/2\pi = 19.4\,{\rm MHz}$, $m = 9\,{\rm u}$, and $k_A = 2\pi/\lambda_A = 2\pi/313\,{\rm nm}$. The fluorescence signal,

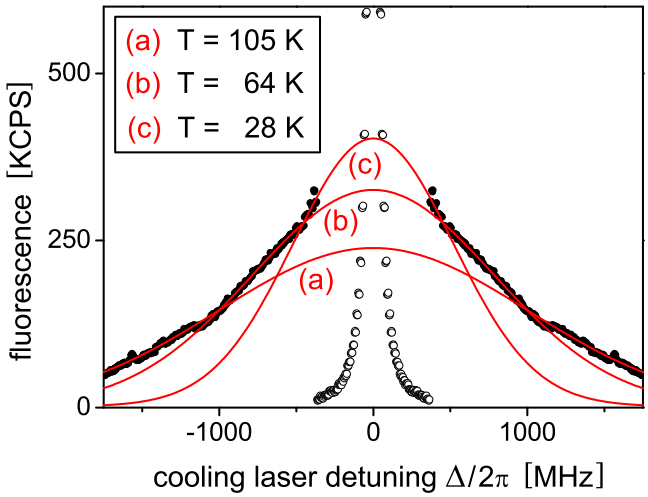

Figure 6.3: *Series of three Voigt profiles* $\epsilon N \cdot \bar{\Gamma}_{ph}(\Delta; I = 8.1\, I_{sat}, T = T_i)$*, with* $T_1 = 105\,K$ *(a),* $T_2 = 64\,K$ *(b), and* $T_3 = 28\,K$ *(c), fitted to the measured fluorescence signal from Fig. 6.2. The Voigt profiles are fitted to consecutive groups of data points* ● *, obtained right before the occurrence of the fluorescence dip. Data points* ○ *, obtained after the occurrence of the fluorescence dip, are also included in the plot. All data points are mirrored at the vertical axis through* $\Delta = 0$ *and corrected for the background signal of* 255 *KCPS.*

as measured by the PMT, may thus be written as $\epsilon N \cdot \bar{\Gamma}_{\mathrm{ph}}(\Delta; T, I)$. Here, N is the total number of laser-cooled ions and ϵ is the overall efficiency of the detection system, including the UHV objective, interference filter, and PMT (→ Sect. 3.4).

Fig. 6.3 shows a series of three Voigt profiles $\epsilon N \cdot \bar{\Gamma}_{\mathrm{ph}}(\Delta; I = 8.1\, I_{\mathrm{sat}}, T = T_i)$, with $T_1 = 105\,\mathrm{K}$ (a), $T_2 = 64\,\mathrm{K}$ (b), and $T_3 = 28\,\mathrm{K}$ (c), fitted to the measured fluorescence signal from Fig. 6.2. The Voigt profiles are fitted to consecutive groups of data points, obtained right before the occurrence of the fluorescence dip at $\Delta_{\mathrm{dip}} \approx -0.4\,\mathrm{GHz}$. The Voigt profiles are dominated by Doppler broadening, in which case not both quantities ϵN and I can be determined independently from the Voigt profile fits, in addition to the temperature T. Nevertheless, with I set equal to $8.1\, I_{\mathrm{sat}}$ as will be discussed below, a value of $\epsilon N = 0.10$ is obtained from the three fits in Fig. 6.3. For a typical number of $N \approx 1000$ $^9Be^+$ ions, this corresponds to an overall detection efficiency of $\epsilon \approx 10^{-4}$ in rather good agreement with the estimate in Sect. 3.4.

With the ion density $n_0 = 3.08 \cdot 10^4\,\mathrm{mm}^{-3}$ [Eq. (2.6)] and the Wigner-Seitz radius $a_{\mathrm{WS}} \stackrel{\mathrm{def}}{=} (3/4\pi n_0)^{1/3} = 19.8\,\mu\mathrm{m}$, the Debye length λ_D [Eq. (2.4)] and plasma coupling parameter Γ [Eq. (2.5)] can be calculated as well[a]. For the temperatures $T_1 = 105\,\mathrm{K}$, $T_2 = 64\,\mathrm{K}$, and $T_3 = 28\,\mathrm{K}$, obtained from the three fits in Fig. 6.3, Debye lengths and plasma coupling parameters are calculated as $\lambda_{D,1} = 127\,\mu\mathrm{m}$, $\lambda_{D,2} = 99\,\mu\mathrm{m}$, $\lambda_{D,3} = 65\,\mu\mathrm{m}$, and $\Gamma_1 = 0.008$, $\Gamma_2 = 0.013$, $\Gamma_3 = 0.031$. Accordingly, as the laser frequency ω_L is scanned towards the cooling transition frequency ω_A,

[a] In calculating the Debye length λ_D [Eq. (2.4)], the zero-temperature ion density n_0 is used as an estimate for the finite-temperature ion density n.

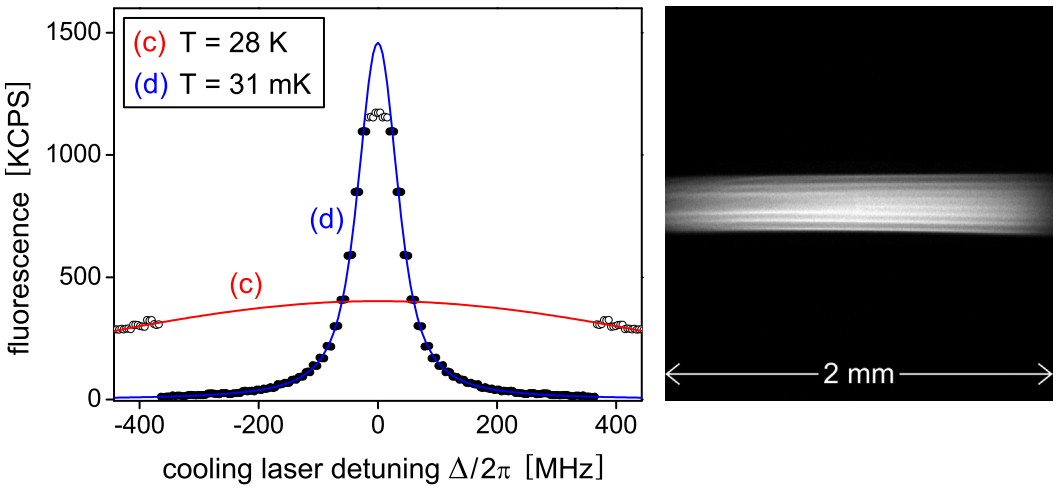

Figure 6.4: Left: *Voigt profile* $\epsilon N \cdot \bar{\Gamma}_{ph}(\Delta; I = 8.1\, I_{sat}, T = 31\, mK)$ *(d), fitted to those data points ● of the measured fluorescence signal from Fig. 6.2 which were obtained after the occurrence of the fluorescence dip. The nine innermost data points ○ are omitted from the fit since they only indicate the clipping of the photon-counting unit (→ Sect. 3.4). For comparison, the Voigt profile (c) from Fig. 6.3 is also included. All data points are mirrored at the vertical axis through* $\Delta = 0$ *and corrected for the background signal of 255 KCPS.* ***Right:*** *CCD image of the partially crystallized* $^9Be^+$ *ion plasma, obtained at nearly zero cooling laser detuning in the maximum of curve (d). In axial direction, the plasma extends well beyond the region which is imaged by the CCD camera.*

the temperature T of the laser-cooled $^9Be^+$ ions decreases and thus the plasma coupling parameter Γ increases. However, the plasma still remains only weakly correlated ($\Gamma \ll 1$). Moreover, the Debye length λ_D stays within a range which is still of the same order of magnitude as the smallest plasma dimension [b]. From the description of the thermal equilibrium states of a mesoscopic single-species plasma, given in Sect. 6.1, a cloud-like spatial distribution of the $^9Be^+$ ions is expected, which already deviates from a Gaussian distribution but still is far from a constant density distribution. Indeed, in the CCD images that were taken while obtaining the fluorescence signal shown in Fig. 6.3, a cloud-like spatial distribution of the $^9Be^+$ ions could be observed. However, the comparatively small fluorescence signal of about 100 – 500 KCPS, distributed over a large number of CCD pixels, resulted in a poor signal-to-noise ratio. This made impossible any accurate characterization of the spatial distribution of the $^9Be^+$ ions.

Fig. 6.4 (left) shows the Voigt profile $\epsilon N \cdot \bar{\Gamma}_{\rm ph}(\Delta; I = 8.1\, I_{\rm sat}, T = 31\,{\rm mK})$, fitted to those data points of the measured fluorescence signal from Fig. 6.2 which were obtained after the occurrence of the fluorescence dip at $\Delta_{\rm dip} \approx -0.4\,{\rm GHz}$. The corresponding linewidth is only a few times the natural linewidth $\gamma/2\pi = 19.4\,{\rm MHz}$ and therefore allows to independently determine the parameters ϵN, I, and T from

[b] As an estimate of the smallest plasma dimension, the transverse extension $\delta_r = (2k_B T/m\omega_r^2)^{1/2}$ of the Gaussian distribution $n(\boldsymbol{r}) \propto \exp[-Q\phi_{\rm trap}(\boldsymbol{r})/k_B T]$ may be taken (→ Sect. 6.1). In particular, $\delta_r = 134\,\mu{\rm m}$ for $T = 28\,{\rm K}$, $m = 9\,{\rm u}$, and $\omega_r/2\pi = 271\,{\rm kHz}$.

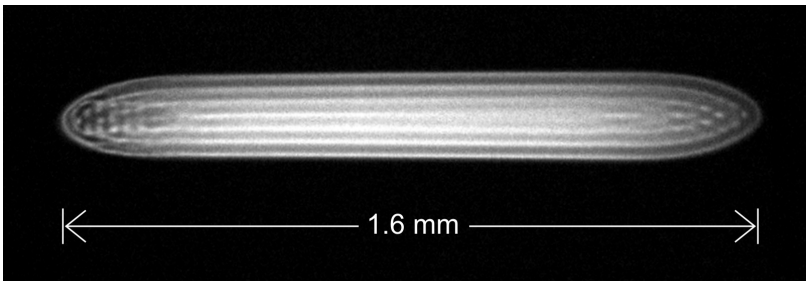

Figure 6.5: *Ion crystal, containing $N \approx 1200$ $^9Be^+$ ions and an unknown number of non-fluorescent high-mass impurity ions from the background gas. The cylindrical crystal shape results from the high-mass impurity ions which fill up the trap potential from a given cylindrical shell on. The length scale was determined from the lateral magnification = 3.1 of the CCD camera setup (→ Sect. 3.4).*

the Voigt profile fit. In particular, a value of $I = 8.1\, I_{\mathrm{sat}}$ is determined which is well within the expected range between $6.3\, I_{\mathrm{sat}}$ and $12.5\, I_{\mathrm{sat}}$ (the typical transverse dimensions of a $^9Be^+$ ion crystal are much smaller than the beam radius $w \approx 0.7\,\mathrm{mm}$). However, the corresponding value of the overall detection efficiency multiplied with the total number of ions is $\epsilon N = 0.028$, thus decreased to approximately 30% of the value which was obtained from the three Voigt profile fits in Fig. 6.3. This points out the limit of the assumption made, that the whole fluorescence signal in Fig. 6.2 can be adequately described by a series of Voigt profiles $\epsilon N \cdot \bar{\Gamma}_{\mathrm{ph}}(\Delta; I, T_i)$, where $i = 1, 2, 3, \ldots$ and ϵN as well as I are held constant. Nevertheless, except for the discontinuous change of ϵN at the fluorescence dip, the Voigt profiles shown in Fig. 6.3 and Fig. 6.4 (left) fit well to the measured fluorescence signal. This indicates that they can be still expected to give reasonable estimates of the $^9Be^+$ ion temperatures at different cooling laser detunings.

For the temperature of $T = 31\,\mathrm{mK}$, obtained from the Voigt profile fit (d) in Fig. 6.4 (left), a Debye length of $\lambda_D = 2\,\mu\mathrm{m}$ and a plasma coupling parameter of $\Gamma = 28$ is calculated. Thus, according to the description of the thermal equilibrium state of a strongly correlated single-species plasma, given in Sect. 6.1, a partially crystallized plasma is expected with a clearly developed shell structure in the outer plasma regions. This agrees well with the CCD image of the large $^9Be^+$ ion plasma shown in Fig. 6.4 (right), which was obtained at nearly zero cooling laser detuning in the maximum of curve (d). The cylindrical outer shape of the crystal, instead of a spheroidal shape, results from non-fluorescent high-mass impurity ions from the background gas. Since the radial confinement provided by the time-averaged trap potential (2.3) becomes weaker with increasing mass-to-charge ratio m/Q, the high-mass impurity ions surround the $^9Be^+$ ions, filling up the trap potential from a given cylindrical shell on. A further $^9Be^+$ ion crystal with a completely developed shell structure is shown in Fig. 6.5. Due to the reduced ion number as compared to the partially crystallized $^9Be^+$ ion plasma in Fig. 6.4 (right), a plasma coupling parameter $\Gamma > 28$ can be expected. Again, the observed cylindrical crystal shape indicates a large amount of additionally trapped, high-mass impurity ions from the background gas.

6.3 Ellipsoidal Shaped $^9Be^+$ Ion Crystals

In this section, different-sized $^9Be^+$ ion crystals will be studied for the most general case of a fully anisotropic confining potential, i.e. the time-averaged trap potential (2.3) with non-degenerate trap frequencies $\omega_x > \omega_y > \omega_z$. According to Sect. 2.2.2, an adequate description of the gross outer shape and average number density within the $^9Be^+$ ion crystals is expected to be given by the charged fluid model. In particular, a tri-axial ellipsoid with a constant number density is predicted for the case of a fully anisotropic 3-D harmonic confining potential. In this section, the charged fluid model will be tested by a comparison with the outer shape of the $^9Be^+$ ion crystals. In addition, in case of additionally trapped low-mass impurity ions, a complete spatial separation of the sympathetically cooled impurity ions from the laser-cooled $^9Be^+$ ions will be demonstrated by "squeezing" of the ion crystals. Up to the present time, comparisons of the gross outer shape of a single species ion crystal with the charged fluid model have been carried out in Penning traps [125] and linear rf (Paul) traps [42,75] for the special case of a 3-D harmonic confining potential with cylindrical symmetry. For the linear rf trap, this corresponds to the case of the time-averaged trap potential (2.3) with degenerate transverse trap frequencies $\omega_x = \omega_y$. The corresponding prediction of the charged fluid model is a spheroid with constant number density (→ Fig. 2.2 in Sect. 2.2.2). Good agreement is reported in all references cited. For the most general case of a fully anisotropic confining potential, a test of the charged fluid model so far has been carried out only in Penning traps [126].

The work described in this section is also described in Ref. [7]. However, in contrast to Ref. [7], the present section is based on a more well-founded theoretical description of the crystalline state of a mesoscopic single species plasma, as was given in Sect. 6.1. Furthermore, an improved evaluation and representation of the measured aspect ratio data is included as well.

In the experiments, the linear rf trap (→ Sect. 3.2) was operated at a rf frequency of $\Omega/2\pi = 14.2\,\mathrm{MHz}$ and an amplitude of $U_{\mathrm{RF}} = 380\,\mathrm{V}$. This corresponds to a stability parameter of $q = 0.055$ [Eq. (2.1)] which implies that the time-averaged potential description is valid. For axial confinement, a static voltage of $U_{\mathrm{EC}} = 4.5\,\mathrm{V}$ was applied to the endcap electrodes. Thus, in case of no additional static voltage U_{DC} (→ Sect. 2.1) applied to the trap electrodes, degenerate transverse trap frequencies $\omega_x/2\pi = \omega_y/2\pi = 269\,\mathrm{kHz}$ [Eqs. (2.3b) and (2.3c)] and an axial trap frequency of $\omega_z/2\pi = 85.6\,\mathrm{kHz}$ [Eq. (2.3d)] are calculated. For the latter, a geometric constant of $\kappa \cdot 3.0{\cdot}10^{-3}/\mathrm{mm}^2$ was assumed (→ Sect. 3.2). The main sources of error in calculating the trap frequencies are the uncertainties in rf amplitude U_{RF} and geometric constant κ as will be discussed below. Preparation of the $^9Be^+$ ion crystals included the following steps. First, the linear rf trap was loaded with $^9Be^+$ ions at a background pressure of $P < 1 \cdot 10^{-10}\,\mathrm{mbar}$ by electron impact ionization of Be atoms in the trap center. The Be atoms were evaporated from a small Be oven (→ Sect. 3.2). After several 3 – 5 GHz scans of the 313 nm cooling laser (→ chapter 4) and a reduction of the total number of trapped ions by lower-

ing the rf amplitude U_{RF} for a few seconds, the $^9Be^+$ plasma crystallized. Finally, the cooling laser frequency was locked to an I_2 hyperfine line (→ Sect. 4.3.1) and fine-adjusted a few 10 MHz below the cooling transition frequency by maximizing the fluorescence of the $^9Be^+$ ions. Images of the $^9Be^+$ ion crystals were obtained with a CCD camera which was mounted transverse to the trap axis (→ Sect. 3.4). A two second exposure time was chosen.

Fig. 6.6 (a) shows a $^9Be^+$ ion crystal, containing $N \approx 2000$ $^9Be^+$ ions as well as a small number of additionally trapped, low-mass impurity ions. The latter are located on the trap axis [a] and do not fluoresce in the 313 nm cooling laser light. For the $^9Be^+$ ions, a temperature T in the order of 30 mK is expected from Fig. 6.4 of the previous section, showing the fit of a Voigt profile to the fluorescence signal of a partially crystallized $^9Be^+$ plasma of somewhat larger size. From this, a plasma coupling parameter of $\Gamma \approx 30$ [Eq. (2.5)] is calculated for the given trap settings. In the terminology of Sect. 6.1, the $^9Be^+$ ion crystal in Fig. 6.6 (a) is a *strongly correlated mesoscopic* single species plasma, if neglecting the small number of additionally trapped, low-mass impurity ions. In good agreement with the theoretical predictions given under case III in Sect. 6.1, and the calculated ion number densities shown in Fig. 6.1, only partial crystallization of the $^9Be^+$ ion plasma is observed. In particular, development of a shell structure progressing from the outer to the inner plasma regions is clearly visible, where diffusion of the $^9Be^+$ ions still takes place even within the completely developed 2 – 3 outermost shells. According to Sect. 2.2.2, an adequate description of the gross outer shape and average ion number density within the $^9Be^+$ ion crystal is expected to be given by the charged fluid model. In particular, a spheroid (ellipse of revolution) with aspect ratio $R_x/L = R_y/L = 0.175$ [Eqs. (2.8a) and (2.8b)] and constant number density of $n_0 = 3.1 \cdot 10^4/\text{mm}^3$ [Eq. (2.6)] is predicted for the given trap settings, as will be further discussed below. The total number of $N \approx 2000$ $^9Be^+$ ions was estimated from molecular dynamics (MD) simulations in which the observed crystal structure (especially the number of shells) was reproduced [127]. The MD simulation proved consistent with the length scale shown in Fig. 6.6 (a) which was determined from the measured lateral magnification = 3.14 of the CCD camera setup (→ Sect. 3.4). Alternatively, the total number of $^9Be^+$ ions may be determined by multiplying the theoretical number density n_0 with the measured spheroid volume $V = (4\pi/3) R_{45}^2 L$, yielding $N \approx 2200$ $^9Be^+$ ions. This is in reasonable agreement with the MD simulation value. Finally, it should be noted that radiation pressure acting solely on the laser-cooled $^9Be^+$ ions, causes the asymmetric distribution of the non-fluorescent low-mass impurity ions along the trap axis, i.e. the dark central region on the left side of the $^9Be^+$ ion crystal.

After obtaining the CCD image shown in Fig. 6.6 (a), a static voltage $0 < U_{DC} < 4.2\,\text{V}$ (→ Sect. 2.1) was applied to the trap electrodes, thus adding a static quadrupole component to the time-averaged trap potential (2.3). A corre-

[a] Radial confinement by the time-averaged trap potential (2.3) increases with a decreasing mass-to-charge ratio m/Q. Thus, impurity ions with $m/Q < 9\,\text{u/e}$ will be pushed to the trap axis while impurity ions with $m/Q > 9\,\text{u/e}$ will gather in the outer crystal regions. The first shall be referred to as *low-mass* impurity ions while the latter shall be referred to as *high-mass* impurity ions.

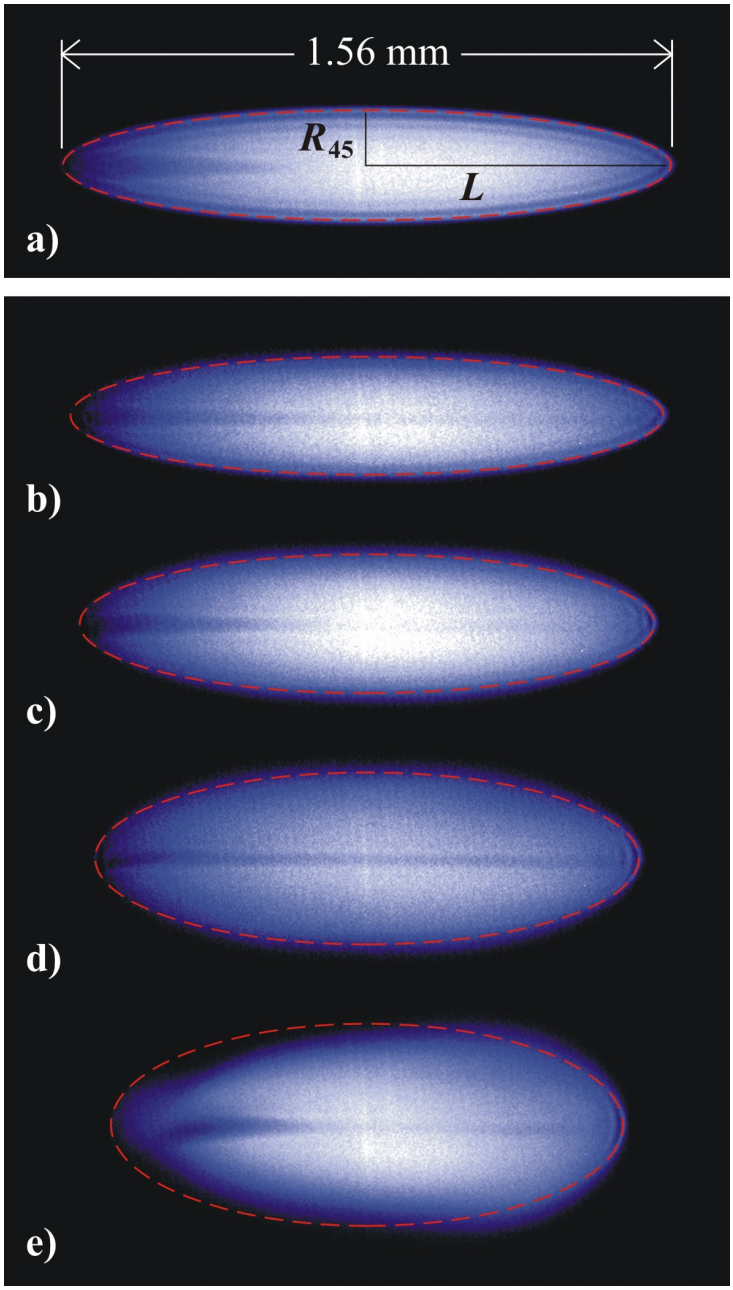

Figure 6.6: *Sequence of CCD images, showing the ellipsoidal deformation of a $^9Be^+$ ion crystal, containing approximately $N = 2000$ $^9Be^+$ ions. At $U_{DC} = 0$ (a), the time-averaged trap potential possesses cylindrical symmetry around the trap axis, and the predicted crystal shape is a prolate spheroid with radius $R_x = R_y$ and half length L. By applying $U_{DC} = 1.8$ (b), 2.8 (c), 3.6 (d), and 4.2 V (e), the cylindrical symmetry is broken and the predicted crystal shape is an ellipsoid with principal axes $R_x < R_y < L$. With increasing value of U_{DC}, the $^9Be^+$ ion crystal expands in transverse y-direction (R_y) while contracts in transverse x-direction (R_x) and axial z-direction (L). Dashed red lines indicate fits of ellipses with principal axes R_{45} and L to the outermost crystal shell, where $R_{45} \stackrel{def}{=} [(R_x^2 + R_y^2)/2]^{1/2}$. In particular, $(R_{45}/\,\mu m, L/\,\mu m) = (139, 780)$ (a), $(148, 770)$ (b), $(175, 740)$ (c), $(216, 699)$ (d), and $(271, 657)$ (e). The length scale was determined from the measured lateral magnification = 3.14 of the CCD camera setup (→ Sect. 3.4).*

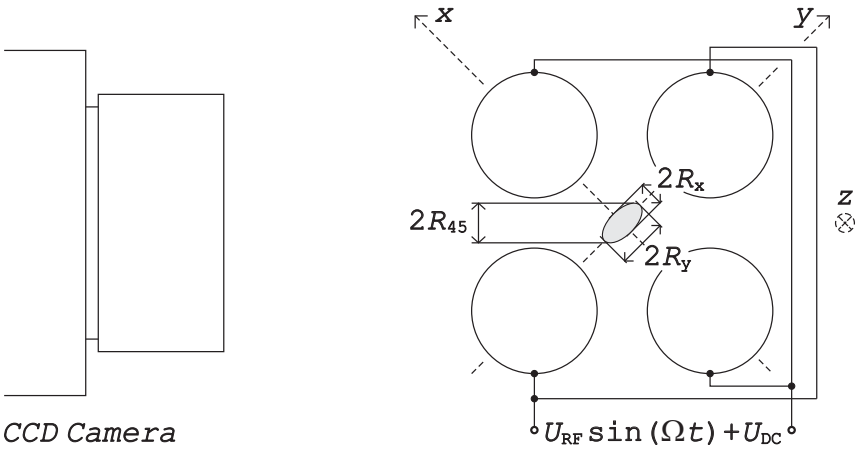

Figure 6.7: *Definition of the principal axis length R_{45} in the CCD images. The principal axes R_x, R_y, and L of the ellipsoidal shaped plasma as well as the time-averaged trap potential (2.3) are defined with respect to the trap coordinate system (dashed lines), introduced in Sect. 2.1.*

sponding increase in transverse trap frequency $\omega_x/2\pi$ [Eq. (2.3b)] from 269 kHz to a maximum value of 359 kHz and a corresponding decrease in transverse trap frequency $\omega_y/2\pi$ [Eq. (2.3c)] from 269 kHz to a minimum value of 125 kHz is calculated. This gives rise to a fully anisotropic time-averaged trap potential (2.3) with non-degenerate trap frequencies $\omega_x > \omega_y > \omega_z$. Although the theoretical stability limit ($\omega_y = 0$) should not be reached until application of a static voltage $U_{\rm DC} = 4.96\,{\rm V}$, partial loss of the $^9Be^+$ ions already was observed at $U_{\rm DC} > 4.2\,{\rm V}$. For this reason, $U_{\rm DC}$ was limited to a maximum value of 4.2 V.

Fig. 6.6 (b–e) shows the change in outer shape of the $^9Be^+$ ion crystal, resulting from the application of the static voltages $U_{\rm DC} = 1.8$ (b), 2.8 (c), 3.6 (d), and 4.2 V (e), respectively. With increasing value of $U_{\rm DC}$, the $^9Be^+$ ion crystal expands in transverse y-direction while contracts in transverse x-direction and axial z-direction. The corresponding charged fluid prediction is a tri-axial ellipsoid with principal axes ratios R_x/L [Eq. (2.8a)] and R_y/L [Eq. (2.8b)], and a constant number density $n_0 = 3.1 \cdot 10^4/{\rm mm}^3$ [Eq. (2.6)]. This will be further discussed below. In Fig. 6.6 (b–e), the size of the inner $^9Be^+$ plasma region in which no shell structure seems to develop, appears to increases with increasing value of the static voltage $U_{\rm DC}$. This was confirmed by MD simulations [127], showing a change in local order of the $^9Be^+$ ions and a reduction of the number of shells as the static voltage $U_{\rm DC}$ increases. In particular, although the value of the plasma coupling parameter Γ was kept constant in the MD simulations, an increase in random move of the $^9Be^+$ ions in the inner plasma regions was observed with increasing static voltage $U_{\rm DC}$. Moreover, in Fig. 6.6 (e), at a maximum static voltage of $U_{\rm DC} = 4.2\,{\rm V}$, the $^9Be^+$ ion crystal does not exhibit a closed outer boundary anymore. This may be explained by the presence of non-fluorescent high-mass impurity ions, located at larger distances from the trap axis as compared to the $^9Be^+$ ions, and partially replacing the $^9Be^+$ ions in the outermost shell (see also Fig. 6.5). According to the stability condition $\omega_y(m/Q) > 0$ [Eq. (2.3c)], no stable trapping is possible at $U_{\rm DC} = 4.2\,{\rm V}$ for

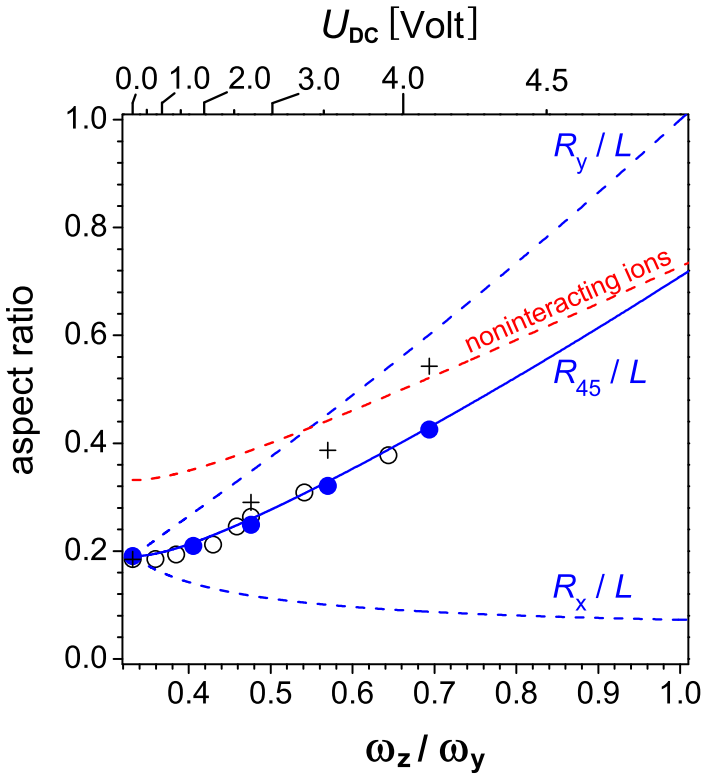

Figure 6.8: *Comparison of the measured aspect ratio data with the charged fluid model. Aspect ratios R_{45}/L obtained from elliptical fits to the CCD images are plotted versus the frequency ratio ω_z/ω_y of the axial and the smallest transverse trap frequency: large $^9Be^+$ ion crystal from Fig. 6.6 (●), medium-sized $^9Be^+$ ion crystal from Fig. 6.9 (left) (○), and small $^9Be^+$ ion crystal from Fig. 6.9 (right) (+). An average over three sequences of CCD images, only the first one of which is shown in Fig. 6.6, was performed in case of the large $^9Be^+$ ion crystal. Moreover, additional data points were added in case of the medium-sized $^9Be^+$ ion crystal. The theoretical curves R_x/L (- - -), R_y/L (- - -), and $R_{45}=[(R_x^2+R_y^2)/2]^{1/2}$ (——) were obtained by numerical solution of Eqs. (2.8a) and (2.8b), assuming $U_{DC}=399$ V and $\omega_z/2\pi=93.3$ kHz (see text). A dashed red line shows the aspect ratio R_{45}/L, expected in case of negligible interaction between the $^9Be^+$ ions.*

ions with a mass-to-charge ratio $m/Q \geq 11$ u/e. Thus, the high-mass impurity ions are presumably BeH^+ ($m/Q=10$ u/e) molecular ions, formed by chemical reactions between the $^9Be^+$ ions and neutral H_2 molecules from the background gas [10]. As in case of the low-mass impurity ions, radiation pressure which solely acts on the laser-cooled $^9Be^+$ ions causes an asymmetric distribution of the high-mass impurity ions along the trap axis. Finally, it should be noted that the ellipsoidal deformation in Fig. 6.6 (b–e) is a reversible process if the static voltage U_{DC} is kept within the range $0<U_{DC}<4.2$ V: after turning the static voltage U_{DC} off, the $^9Be^+$ ion crystal returned to its initial spheroidal shape shown in Fig. 6.6 (a).

In order to allow for a comparison of the $^9Be^+$ ion crystal gross outer shape with the charged fluid predictions, the orientation of the CCD camera with respect to the linear rf trap has to be considered. This is illustrated in Fig. 6.7. Accordingly, a two-dimensional projection of the $^9Be^+$ ion crystal is seen by the CCD camera which

is rotated by 45° with respect to the x and y-axis of the trap coordinate system (→ Sect. 2.1). Thus, a $^9Be^+$ ion crystal having the gross outer shape of an ellipsoid with principal axes R_x, R_y, and L along the x, y, and z-axis, respectively, will be imaged as a two-dimensional ellipse with principal axes $R_{45} \stackrel{\text{def}}{=} [(R_x^2+R_y^2)/2]^{1/2}$ and L. In Fig. 6.6, ellipses (red dashed lines) with principal axes R_{45} and L have been fitted to the outermost shell of the $^9Be^+$ ion crystal in the CCD images. Accordingly, in case of the spheroidal shaped crystal ($U_{\text{DC}}=0$) shown in Fig. 6.6 (a) as well as in case of a modest ellipsoidal deformation ($U_{\text{DC}}=1.8$ and $2.8\,\text{V}$) shown in Fig. 6.6 (b) and (c), almost perfect fits are possible. In contrast to this, a clear deviation of the outer boundary in the CCD image from an ellipse can be seen in case of a maximum ellipsoidal deformation ($U_{\text{DC}}=4.2\,\text{V}$), shown in Fig. 6.6 (e). In this case, the fit has been chosen to match the fragments of the outermost shell which still exist at the left and right ends of the $^9Be^+$ ion crystal. From the elliptical fits, the aspect ratios R_{45}/L were calculated. In particular, half a typical shell spacing of $1.48\,a_{\text{WS}}=29\,\mu\text{m}$ (→ Sect. 2.2) was added to the principal axes lengths from Fig. 6.6 before calculating R_{45}/L, in order to emulate the continuous spatial distribution of the charged fluid. Additionally, a further increase in accuracy of the measured aspect ratio data was achieved by taking an average over three sequences of CCD images, only the first one of which is shown in Fig. 6.6. Fig. 6.8 shows the aspect ratios R_{45}/L (blue full circles) together with the corresponding charged fluid predictions. The latter is given by a numerical solution of the two coupled equations (2.8a) and (2.8b), yielding R_x/L and R_y/L (blue dashed lines), and thus $R_{45}/L=[(R_x^2+R_y^2)/2]^{1/2}/L$ (blue solid line). Since the rf amplitude U_{RF} and the axial trap frequency ω_z can not be determined with an accuracy better than ±10%, the theoretical curve was fitted to the measured data by choosing U_{RF} and ω_z as two independent fit parameters. By this, values of $U_{\text{RF}}=399\,\text{V}$ and $\omega_z/2\pi=93.3\,\text{kHz}$ [b] were obtained, thus differing by +5% and +9% from the nominal values $U_{\text{RF}}=380\,\text{V}$ and $\omega_z/2\pi=85.6\,\text{kHz}$, respectively, the latter being used in Ref. [7]. With these slight changes, excellent agreement is obtained between the measured aspect ratios R_{45}/L and the charged fluid predictions, which is true even in case of the strong ellipsoidal deformation at $U_{\text{DC}}=4.2\,\text{V}$, shown in Fig. 6.6 (e). In Fig. 6.8, the aspect ratio R_{45}/L (red dashed line) which is expected in case of negligible interaction between the $^9Be^+$ ions, is indicated as well. In this case, $R_x/L=\omega_z/\omega_x$ and $R_y/L=\omega_z/\omega_y$ (→ Sect. 6.1). Accordingly, due to the collective interaction by space charge, as described by the charged fluid model, the ellipsoidal deformation becomes more pronounced as compared to the case of negligible interaction.

In order to complete the investigation of $^9Be^+$ ion crystals in a fully anisotropic time-averaged trap potential (2.3), two more crystals were prepared with a reduced number of $^9Be^+$ ions as compared to that in Fig. 6.6. In particular, a $^9Be^+$ ion crystal, containing $N\approx 500$ $^9Be^+$ ions and a few low-mass impurity ions located on the trap axis, is shown in Fig. 6.9 (a–d). The static voltage U_{DC} was increased from 0 (a)

[b] From the above value of the axial trap frequency ω_z and the endcap voltage $U_{\text{EC}}=4.5\,\text{V}$, a geometric constant of $\kappa=3.57\cdot10^{-3}/\text{mm}^2$ is calculated. Thus, an alternative way is established to estimate κ for the linear rf trap, besides from the SIMION simulation ($\kappa=3.37\cdot10^{-3}/\text{mm}^2$) and the LCF-MS measurement ($\kappa=2.98\cdot10^{-3}/\text{mm}^2$), both described in Sect. 3.2.

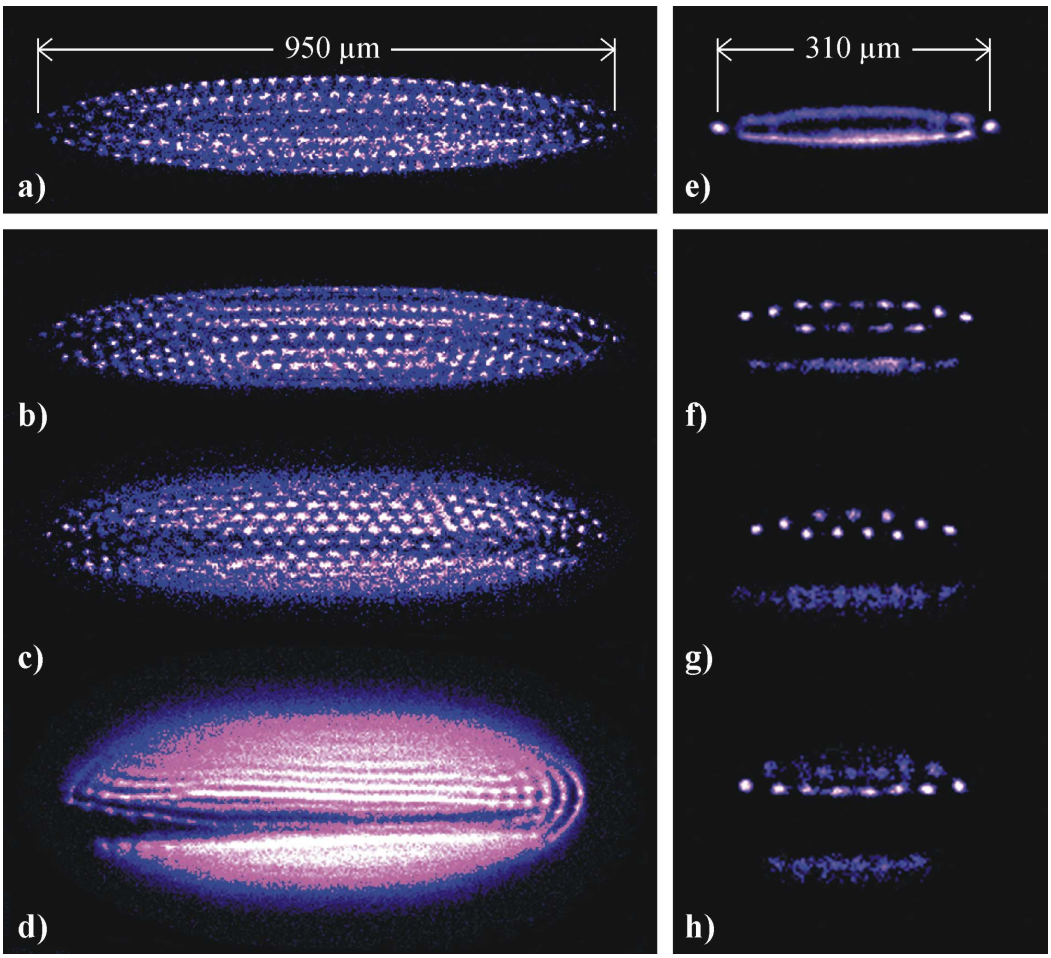

Figure 6.9: Left: *Sequence of CCD images showing the ellipsoidal deformation of a $^9Be^+$ ion crystal, containing approximately $N = 500$ $^9Be^+$ ions and a few low-mass impurity ions: $U_{DC} = 0$ (a), 1.4 (b), 2.8 (c), and 4.0 V (d).* ***Right:*** *Ellipsoidal deformation of a $^9Be^+$ ion crystal, containing approximately $N = 20$ $^9Be^+$ ions and an increased fraction of low-mass impurity ions: $U_{DC} = 0$ (e), 2.8 (f), 3.6 (g), and 4.2 V (h). At sufficiently high static voltages U_{DC}, a complete separation is possible of the $^9Be^+$ ions from the non-fluorescent low-mass impurity ions located on the trap axis and sympathetically cooled by the $^9Be^+$ ions (g&h). The asymmetric distribution of $^9Be^+$ ions above and below the trap axis at $U_{DC} > 0$ is attributed to stray electric fields.*

to 1.4 (b), 2.8 (c), and 4.0 V (d). In contrast to the large $^9Be^+$ ion crystal shown in Fig. 6.6, complete crystallization of the $^9Be^+$ ion plasma seems to occur, which is true at least for $U_{DC} = 0$ (a) and 1.4 V (b). This proofs consistent with the MD simulations of a strongly correlated single species plasma in Ref. [121], showing that the "washing out" of inner shells (as observed in Fig. 6.6) is expected to increase with the total number of ions. Yet another $^9Be^+$ ion crystal of even smaller size is shown in Fig. 6.9 (e–h), containing $N \approx 20$ $^9Be^+$ ions and an increased fraction of low-mass impurity ions, presumably H_2^+ and H_3^+ (from the reaction $H_2^+ + H_2 \rightarrow H_3^+ + H$). The static voltage U_{DC} was increased from 0 (e) to 2.8 (f), 3.6 (g), and 4.2 V (h). In the terminology of Sect. 6.1, this $^9Be^+$ ion crystal is a *Coulomb cluster* rather than

a *mesoscopic* plasma. At $U_{DC}=0$ (e), giving rise to a time-averaged trap potential (2.3) with cylindrical symmetry around the trap axis, diffusion of $^9Be^+$ ions within a single shell occurs. Two $^9Be^+$ ions are at fixed positions at the left and right end of the crystal. By applying $U_{DC}>0$ (f–h), the cylindrical symmetry is broken and the $^9Be^+$ ion crystal expands in transverse y-direction while contracts in transverse x-direction and axial z-direction. This causes a rearrangement of the $^9Be^+$ ions into a two-dimensional structure, where almost all $^9Be^+$ ions are located at a fixed position. By comparison of the $^9Be^+$ ion spot size in the CCD images with MD simulations [127], an upper limit of $T=10\,\mathrm{mK}$ is deduced for the temperature of the $^9Be^+$ ions. The most apparent property arising when applying the static voltage $U_{DC}>0$, is the completely dark central region, containing the sympathetically cooled low-mass impurity ions. In particular, no fluorescent $^9Be^+$ ions are located in the front or back of the dark region at $U_{DC}=3.6$ (g) and 4.2 V (h). Finally, the pronounced asymmetric distribution of $^9Be^+$ ions above and below the dark central region should be noted, occurring at $U_{DC}>0$ in both $^9Be^+$ ion crystals shown in Fig. 6.9 (b–d) and Fig. 6.9 (f–h). Since this neither conforms with the symmetry of the time-averaged trap potential (2.3) nor can be explained by radiation pressure, residual stray fields are the most probable reason (→ Sect. 3.2). While it was not possible to compensate for possible stray fields by application of additional static voltages to the trap electrodes, it was always possible to reverse the asymmetric distribution of $^9Be^+$ ions by means of these voltages.

While a continuous charged fluid description still seems reasonable for the *mesoscopic* plasma shown in Fig. 6.9 (left), it seems inappropriate for the *Coulomb cluster* shown in Fig. 6.9 (right). Nevertheless, ellipses were fitted to the CCD images in Fig. 6.9 (left) as well as to those in Fig. 6.9 (right), even though the $^9Be^+$ ion crystal in Fig. 6.9 (f–h) does not exhibit a closed boundary. The corresponding aspect ratio data is indicated by open circles (mesoscopic plasma) and crosses (Coulomb cluster) in Fig. 6.8, where half a typical shell spacing of $1.48\,a_{WS}=29\,\mu\mathrm{m}$ was again added to the principal axes lengths. Additional aspect ratio data is included for the mesoscopic plasma, obtained at static voltages $U_{DC}=0.8$, 2.2, 2.6, and 3.4 V. As expected, a rather good agreement with the charged fluid description is obtained for the mesoscopic plasma, while a strong deviation with increasing static voltage U_{DC} is obtained for the Coulomb cluster.

Further studies of ion Coulomb crystals in a fully anisotropic 3-D harmonic confining potential could include the oscillation modes of multi-species ion crystals, which possibly would allow to identify the non-fluorescent species. From a theoretical point of view, detailed studies of strongly squeezed ellipsoidal plasmas are of fundamental interest. In particular, ion rings which represent a novel low-dimensional structure already have been observed in first MD simulations [127].

Chapter 7

Sympathetic Crystallization of $^4He^+$ Ions

In this chapter, sympathetic crystallization of $^4He^+$ ions and their identification by laser-cooled fluorescence mass spectrometry (LCF-MS) will be described. Both LCF-MS and sympathetic crystallization were already described in chapters 5 and 6, respectively. In particular, LCF-MS mass spectra showing the presence of sympathetically cooled $^4He^+$ ions (→ Figs. 5.8 and 5.10) and a small-sized $^9Be^+$ ion crystal containing sympathetically crystallized low-mass impurity ions (→ Fig. 6.9) have already been presented. Nevertheless, because of the significant interest in ultracold $^4He^+$ for high-precision laser spectroscopy, this chapter was added. Main part of the text is adopted from Ref. [8].

7.1 The Two-Body Coulomb System

The two-body Coulomb system is one of the most fundamental in physics, and has been central in the development of quantum mechanics, relativistic quantum mechanics, and QED. In nuclear physics, the study of these systems can provide an alternative method for precise determination of nuclear sizes [128,129]. Hydrogenlike systems studied include the hydrogen atom and its isotopes, muonic hydrogen, the helium ions, muonium, and positronium. More recently, heavy (high-Z) hydrogenlike ions have become available [130] and are being used, e.g., for exploring strong-field QED [131] and for measuring the electron mass [18]. Among the low-Z atomic systems, hydrogen has been the most extensively studied, in particular, by laser spectroscopy. This has resulted, among others, in the most precise measurement of a fundamental constant, the Rydberg constant [132]. While the helium ions $^3He^+$ and $^4He^+$ are important systems because they are complementary to the hydrogen atom, they have been much less studied. Precision measurements of transition frequencies in He^+ ions could provide (i) an independent (metrologically

significant) determination of the Rydberg constant, (ii) an independent determination of the nuclear charge radii and the isotope shift, assuming QED (Lamb shift) calculations are correct, or (iii) a test of QED, using independent radius data (from scattering measurements) as input.

Precise values of the He nuclear radii can test theoretical nuclear methods and force models which accurately describe these special nuclei (^{3}He is the only stable three particle nucleus, ^{4}He is the lightest close shell nucleus). The possibility of QED tests with He^+ ions is attractive because the QED corrections scale with high powers of Z (some of the theoretically unknown contributions scale as Z^6), and thus their relative contribution to transition frequencies is larger than in hydrogen. Also, the available independent He nuclear radius measurements agree, in contrast to the situation in hydrogen.

On the experimental side, the hyperfine structure of $^3He^+$ has been measured in both the electronic $1S$ ground state and the $2S$ excited state [133,134] (for the theory, see Ref. [135]). The Lamb shift of the $2S$ state in $^4He^+$ has been determined from the spontaneous emission anisotropy with 170 kHz uncertainty and compared to theoretical calculations [136,137]. The ^{3}He/^{4}He squared nuclear radius difference has been determined at the 0.4% level from the isotope shift in neutral helium using laser spectroscopy [138].

A significant extension of these studies would be accessible via high-resolution laser spectroscopy of helium ions, which has not been performed so far. Measurements of the $1S$-$2S$ and $2S$-$3S$ two-photon transition frequencies (at 61 and 328 nm, with linewidths of 167 Hz and 16 MHz, respectively) have been proposed [139,140]. For example, a $1S$-$2S$ measurement with reasonable experimental uncertainty < 30 kHz would test the nuclear and the recently improved theoretical QED contributions at their current accuracy level [141]. A measurement of the isotope shift with a similar accuracy would improve the value of the squared nuclear charge radius difference by one order of magnitude.

One important aspect in these future precision experiments will be the availability of trapped ultracold helium ions in order to minimize the influence of Doppler broadening or shifts, and to allow a precise study of systematic effects. The success of this approach has been shown by the experience with trapped ions for atomic clocks [142]. Unfortunately, direct laser cooling of helium ions appears impractical at present, since the generation of the required continuous wave deep-UV 30 nm radiation is a challenging problem in itself. On the other hand, sympathetic cooling of helium ions by directly laser-cooled atomic ions offers itself as a promising experimental technique. However, at this point, the transfer of energy from the micromotion of the laser-cooled (LC) ions to the secular motion of the sympathetically cooled (SC) ions has to be considered since it is expected to become dominant in the limit of a small mass ratio $m_{\mathrm{SC}}/m_{\mathrm{LC}}$ [29]. Thus, a laser-cooled ion with a sufficiently small mass is needed. The $^9Be^+$ ion which is the lightest atomic ion suitable for practical laser cooling, appears to be the most appropriate coolant ion for sympathetic cooling of $^4He^+$ and $^3He^+$. In the next section, sympathetic cooling of $^4He^+$ ions down to the milli-Kelvin range will be described.

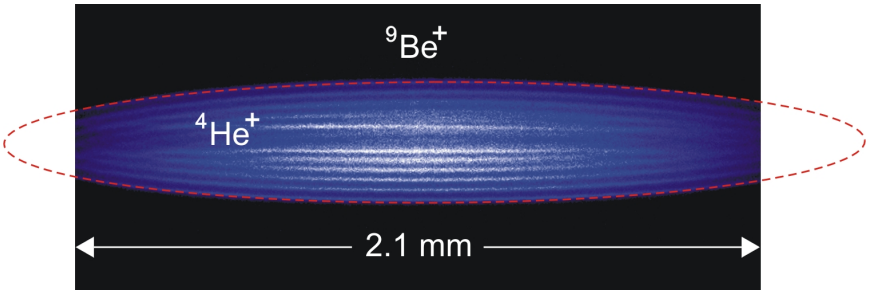

Figure 7.1: *CCD image of a prolate two-species $^9Be^+$-$^4He^+$ ion crystal (exposure time: 2 s). $N_{SC} \approx 150$ $^4He^+$ ions, contained in the inner dark core, are sympathetically crystallized by $N_{LC} \approx 6200$ laser-cooled $^9Be^+$ ions (see text). In horizontal direction, i.e. along the trap axis, the crystal extends well beyond the CCD image. A dashed red line indicates the fit of an ellipse to the outer crystal boundary, yielding an aspect ratio of $R/L = 0.15$.*

7.2 Two-Species $^9Be^+$-$^4He^+$ Ion Crystals

In the experiments, the linear rf trap (→ Sect. 3.2) was operated at a rf frequency of $\Omega/2\pi = 14.2\,\text{MHz}$ and an rf amplitude of $U_{\text{RF}} = 380\,\text{V}$. A static voltage $U_{\text{EC}} = 3\,\text{V}$ was applied to the endcap electrodes for axial confinement along the trap axis. The corresponding Mathieu stability parameters are $q(^9\text{Be}^+) = 0.055$ and $q(^4\text{He}^+) = 0.12$ [Eq. (2.1)], indicating that stable trapping of the two ion species is possible and that the time-averaged potential description is valid (→ Sect. 2.1). Accordingly, the transverse trap frequencies are $\omega_r(^9\text{Be}^+)/2\pi = 271\,\text{kHz}$ and $\omega_r(^4\text{He}^+)/2\pi = 615\,\text{kHz}$ [Eqs. (2.3b) and (2.3c) with $U_{\text{DC}} = 0$]. The axial trap frequencies are $\omega_z(^9\text{Be}^+)/2\pi = 69.9\,\text{kHz}$ and $\omega_z(^4\text{He}^+)/2\pi = 104.9\,\text{kHz}$ [Eq. (2.3d)]. Here, a geometric constant of $\kappa \approx 3.0 \cdot 10^{-3}/\text{mm}^2$ was assumed (→ Sect. 3.2). The corresponding charged fluid prediction in case of a pure $^9Be^+$ ion plasma is a constant density spheroid with aspect ratio $R/L = 0.14$ (→ Fig. 2.2 in Sect. 2.2.2). Finally, it should be noted that operation of the linear rf trap at small values of q is favorable since rf-heating is less pronounced.

Preparation of the two-species $^9Be^+$-$^4He^+$ ion crystals included the following steps. First, the linear rf trap trap was loaded with $^4He^+$ ions by leaking in neutral He gas into the vacuum chamber up to a pressure of 10^{-8} mbar and ionizing it *in situ* with a 750 eV electron beam (→ Sect. 3.1). The loading rate was controlled by the partial pressure of the neutral He gas and the electron beam intensity. Subsequently, $^9Be^+$ ions were loaded into the trap by ionizing Be atoms which were evaporated from a small oven (→ Sect. 3.2), using the same electron beam. During $^9Be^+$ loading, the 313 nm cooling laser was repeatedly scanned towards the cooling transition frequency, each time starting with a red-detuning of −5 GHz. Once the $^9Be^+$-$^4He^+$ plasma crystallized, the cooling laser was stopped from scanning and locked to an I_2 hyperfine line (→ Sect. 4.3.1). Finally, the cooling laser frequency was fine-adjusted a few 10 MHz below the cooling transition frequency by maximizing the fluorescence of the $^9Be^+$ ions.

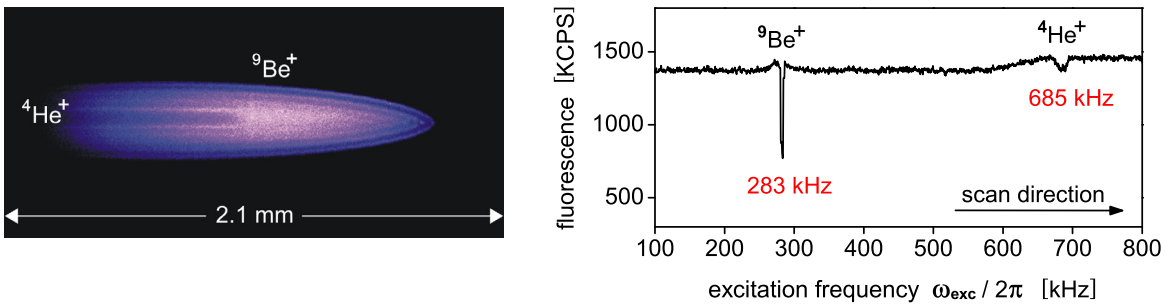

Figure 7.2: Left: *CCD image of a two-species $^9Be^+$-$^4He^+$ ion crystal, similar to those shown in Fig. 7.1.* ***Right:*** *Corresponding LCF-MS mass spectrum, showing the presence of sympathetically crystallized $^4He^+$ ions. The center frequencies of the secular resonances are indicated in red.*

Fig. 7.1 shows a prolate two-species ion crystal, containing $^9Be^+$ and $^4He^+$ ions. The crystal displays a shell structure and encloses an inner dark core, originating from the incorporated sympathetically cooled $^4He^+$ ions having a lower mass-to-charge ratio than the $^9Be^+$ ions. Their location on axis is due to the stronger radial confinement by the time-averaged trap potential experienced by them as compared to the $^9Be^+$ ions. The shape of this large ion crystal, containing only a small relative amount of He^+ ions, agrees well with the charged fluid predictions. In particular, the measured aspect ratio of $R/L = 0.15$ is close to the theoretical value of 0.14.

The number of crystallized ions is estimated by performing molecular dynamics (MD) simulations and varying the total numbers of both ion species, until the observed CCD image is reproduced. While for a single-species $^9Be^+$ ion crystal, one may obtain the ion number from the calculated ion density of $n_0 = 3.1 \cdot 10^4/\mathrm{mm}^3$ [Eq. (2.6)] together with the measured crystal dimensions R and L, here the MD approach is better suited. It is applicable to multi-species structures, produces detailed structural information, and reduces uncertainties related to the calibration of the lateral magnification in the CCD camera setup (→ Sect. 3.4). For example, MD simulations of the crystal in Fig. 7.1 show that it contains $N_{\mathrm{LC}} \approx 6200$ $^9Be^+$ ions and $N_{\mathrm{SC}} \approx 150$ $^4He^+$ ions. Furthermore, the radial intershell distance is obtained as $29\,\mu$m. This agrees well with the theoretical value of $1.48\,a_{\mathrm{WS}} = 29.2\,\mu$m [31], predicted in case of a infinitely long crystal. Here, $a_{\mathrm{WS}} = [3/4\pi n_0]^{1/3}$ is the Wigner-Seitz radius (→ Sect. 2.2). According to the MD simulations, the $^4He^+$ ions are arranged in a zigzag configuration along the trap axis for two-thirds of the crystal, with a pitch spacing of approximately $40\,\mu$m. In the remaining third (left end), the $^4He^+$ ions form a linear string, as evidenced by the smaller radial extension of the inner dark core. The asymmetric distribution is caused by light pressure forces, acting solely on the laser-cooled $^9Be^+$ ions. Embedded strings were also observed in a mixed crystal of $^{40}Ca^+$ and $^{24}Mg^+$ ions, where both ions were laser cooled [75].

In order to identify the sympathetically crystallized ions, laser-cooled fluorescence mass spectrometry (LCF-MS) was employed (→ chapter 5). Fig. 7.2 (left) and Fig. 7.3 (left) each shows a CCD image of a large two-species $^9Be^+$-$^4He^+$ ion crystal, before (Fig. 7.2) and after (Fig. 7.3) performing LCF-MS, i.e. re-

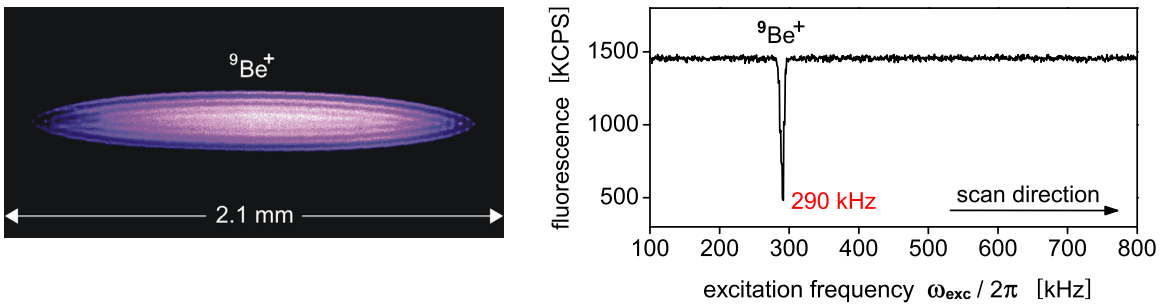

Figure 7.3: Left: *Ion crystal from Fig. 7.2 (left) after removal of the $^{4}He^{+}$ ions by repeated secular excitation.* ***Right:*** *Corresponding LCF-MS mass spectrum. The center frequency of the secular resonance is indicated in red. The time between obtaining Figs. 7.3 and 7.2 was 5 min.*

peatedly scanning the excitation frequency ω_{exc} across the $^{9}Be^{+}$ and $^{4}He^{+}$ secular resonances. Initially, the LCF-MS mass spectrum shows the presence of both $^{9}Be^{+}$ (283 kHz) and $^{4}He^{+}$ (685 kHz). The former value is close to the calculated value of $\omega_r(^{9}Be^{+})/2\pi = 271$ kHz. Regarding the $^{4}He^{+}$ secular resonance, both an increase in fluorescence before resonance and a substantial upward shift of the resonance dip from the calculated value of $\omega_r(^{4}He^{+})/2\pi = 615$ kHz is observed. While the first was already discussed in Sect. 5.3.2, the reason for the latter is not clear. In particular, Coulomb interactions between the crystallized $^{4}He^{+}$ and $^{9}Be^{+}$ ions are expected to cause a downward shift of the $^{4}He^{+}$ secular resonance [13], i.e. in contradiction to Fig. 7.2 (right). Finally, it should be noted that the permanent increase in fluorescence signal after scanning across the $^{4}He^{+}$ secular resonance in Fig. 7.2 (right) is due to the partial removal of the $^{4}He^{+}$ ions from the crystal.

After repeatedly scanning the excitation frequency ω_{exc}, the $^{4}He^{+}$ ions were nearly completely removed from the trap, leaving behind an almost pure $^{9}Be^{+}$ ion crystal as shown in Fig. 7.3 (left). This is evidenced by the absence of the $^{4}He^{+}$ secular resonance in the corresponding LCF-MS mass spectrum shown in Fig. 7.3 (right). The small number of impurity ions remaining in the left end of the crystal did not lead to a fluorescence dip in the LCF-MS mass spectrum. Note that the visible crystal size has decreased substantially because of $^{9}Be^{+}$ ion loss. Nevertheless, the average fluorescence level in Fig. 7.3 (right) is essentially the same as in Fig. 7.2 (right). This may be explained by a lower temperature of the $^{9}Be^{+}$ ions and/or reduced micromotion. The apparent horizontal shift of the crystal in Fig. 7.3 (left) compared to Fig. 7.2 (left) is due to a readjustment of the CCD camera.

A central question concerning sympathetically cooled ions is their translational temperature; several observations can shed light on the answer. A direct measurement on $^{24}Mg^{+}$ embedded in a laser-cooled $^{40}Ca^{+}$ crystal yielded an upper limit of 45 mK, deduced from the $^{24}Mg^{+}$ laser excitation linewidth [45]. In a two-ion crystal, sympathetic cooling to the Doppler-limit (<1 mK) has been demonstrated [26]. MD simulations for small ion numbers have shown that sympathetically cooled ions caged by laser-cooled ions are essentially in thermal equilibrium with the latter at the Doppler temperature [48]. Thus, an estimate of the temperature of the

$^4He^+$ may be obtained from the temperature of the laser-cooled $^9Be^+$ ions. A direct upper limit for the translational temperature of the $^9Be^+$ ions was deduced from the spectral line shape of the $^9Be^+$ fluorescence signal as the cooling laser was tuned towards the atomic transition frequency. To this end, a Voigt profile was fitted to the measured fluorescence signal (→ Sect. 6.2). For small crystals (<1000 ions), an upper limit of 42 mK was obtained at optimum laser cooling. Alternatively, an indirect upper temperature limit is obtained by comparing the spot size of the $^9Be^+$ ions in the CCD images with MD simulations; here a tighter limit of $T(^9Be^+) < 20\,\mathrm{mK}$ is found for the $^9Be^+$ temperature. Therefore, assuming thermal equilibrium, a $^4He^+$ temperature of $T(^4He^+) < 20\,\mathrm{mK}$ can be deduced.

The translationally cold and immobilized $^4He^+$ ions in the two-species ion crystals shown in Figs. 7.1 and 7.2 (left) are the first production of an ultracold sample of $^4He^+$ ions reported so far. They are a promising system for high precision spectroscopy and might lead to more precise atomic and nuclear constants. In particular, the weak $1S$-$2S$ transition in $^4He^+$ (and $^3He^+$) could be detected with a high signal to noise ratio using a single adjacent $^9Be^+$ ion as a "quantum sensor", rather than by direct detection of its fluorescence [143]. Significant progress in this direction has been achieved [26,144]. Moreover, sympathetically cooled helium ions open up perspectives for studies of cold collisions and cold chemistry, e.g., generation of $^3HeH^+$ whose hyperfine structure is of interest in fundamental physics.

Chapter 8

Summary and Outlook

In this work, the setup of an experiment aimed at high-precision laser spectroscopy of ultracold molecular hydrogen ions, started at the University of Konstanz in 1999 [1–3], was continued and first results were obtained. In particular, a new linear rf trap and a new trap supply electronics were built, the latter being capable of driving the linear rf trap with a maximum amplitude of $U_{\mathrm{RF}} > 1000\,\mathrm{V}$ at a frequency of $\Omega/2\pi = 14.2\,\mathrm{MHz}$. This made possible the simultaneous trapping of a large mass range ($2\,\mathrm{u} \leq m/z \leq 15\,\mathrm{u}$) with a trap potential depth of several eV over the whole mass range. Furthermore, a fluorescence detection system was added to the experimental setup, including a photomultiplier tube (PMT) and a CCD camera. For laser cooling of the $^9Be^+$ ions, doubly resonant sum-frequency generation (DR-SFG) of 313 nm laser light was performed between a resonantly frequency-doubled monolithic Nd:Yag laser and a Ti:sapphire laser, emitting at 532 and 760 nm wavelength, respectively. An output power of $P_{\mathrm{uv}} > 100\,\mathrm{mW}$ was achieved at 313 nm wavelength, with a high spectral purity (rms short-term frequency fluctuations $< 160\,\mathrm{kHz}$) and a wide continuous tuning range of more than 15 GHz. The DR-SFG setup was added by an absolute frequency stabilization and an optical frequency shifter for the 532 nm master laser, thus obtaining absolutely frequency stabilized 313 nm laser light (frequency drift $< 1\,\mathrm{MHz/h}$) tunable by up to 340 MHz. With this experimental setup, sympathetic cooling of N^+, BeD^+, BeH^+, $^4He^+$, HD^+, and D^+ ions by laser-cooled $^9Be^+$ ions was demonstrated, using laser-cooled fluorescence mass spectrometry (LCF-MS) to detect the sympathetically cooled species. Accordingly, sympathetic cooling at a minimum mass ratio of $m(H_2^+)/m(Be^+) = 0.22$ was shown to be possible with both the sympathetically and laser-cooled ions in a cloud-like state. This points out the incorrectness of the theoretical lower limit $m_{\mathrm{SC}}/m_{\mathrm{LC}} = 0.53$ which was predicted in Ref. [29]. Here, the subscripts *SC* and *LC* denote the sympathetically and the laser-cooled species, respectively. In a further experiment, almost pure $^9Be^+$ ion plasmas were laser-cooled down to temperatures in the milli-Kelvin range where $^9Be^+$ ion crystals formed. The outer shapes of different-sized $^9Be^+$ ion crystals in a fully anisotropic trap potential were compared with the charged fluid predictions, showing good agreement at sufficiently large numbers of $^9Be^+$ ions. By fitting Voigt profiles to the measured

fluorescence signal, a typical temperature of $T(\mathrm{Be}^+) \approx 30\,\mathrm{mK}$ was estimated for the $^9\mathrm{Be}^+$ ions. Finally, an ultracold sample of $^4\mathrm{He}^+$ ions [$T(\mathrm{He}^+) \approx 40\,\mathrm{mK}$] was produced for the first time by sympathetic crystallization of the $^4\mathrm{He}^+$ ions. This may open up perspectives for the high-precision laser spectroscopy of $^4\mathrm{He}^+$ (and $^3\mathrm{He}^+$).

The writing of this thesis was finished more than three years after completing experimental work. Since then, great progress has been made by the group of Prof. S. Schiller at the University of Düsseldorf, culminating in the first laser spectroscopic measurement of ro-vibrational transitions in ultracold HD^+. Thus, rather than giving an outlook from the perspective of the end of experimental work which is described in this thesis, a brief summary of the new experimental results shall be given here.

Subsequent to the sympathetic crystallization of $^4\mathrm{He}^+$ ions, described in chapter 7, sympathetic crystallization of H_2^+, HD^+, D_2^+, and H_3^+ was demonstrated as well. This is described in Ref. [9]. In particular, a two-step loading process was employed, consisting of (i) the preparation of a $^9\mathrm{Be}^+$ ion crystal in the usual way (see chapter 6) and (ii) the addition of molecular hydrogen ions by leaking in the neutral gases H_2, HD, and D_2 into the vacuum chamber. The neutral gases were ionized in the trap center by electron impact, where the H_3^+ ions were formed by chemical reactions between the H_2^+ ions and the neutral H_2 gas. Accordingly, sympathetic cooling at a minimum mass ratio of $m(\mathrm{H}_2^+)/m(\mathrm{Be}^+) = 0.22$ was demonstrated for the crystalline state. Studies of various chemical reactions are presented in Ref. [10], including the reactions $\mathrm{Be}^{+\,*} + \mathrm{HD} \rightarrow \mathrm{BeH}^+ + \mathrm{D}$ and $\mathrm{Be}^{+\,*} + \mathrm{HD} \rightarrow \mathrm{BeD}^+ + \mathrm{H}$, where $\mathrm{Be}^{+\,*}$ denotes the Be^+ ions in the excited state (see introduction of chapter 4), as well as $\mathrm{H}_3^+ + \mathrm{O}_2 \rightarrow \mathrm{HO}_2^+ + \mathrm{H}_2$. For the latter reaction, sympathetic crystallization of H_2^+ ions, as described in Ref. [9], was followed by the chemical reaction $\mathrm{H}_2^+ + \mathrm{H}_2 \rightarrow \mathrm{H}_3^+ + \mathrm{H}$ and a subsequent exposure of the H_3^+ ions to neutral O_2 gas, leaked into the vacuum chamber. In each case, the reaction rates R and coefficients k were measured and compared to the Langevin theory of ion-neutral reactions. An alternative method for the production of ultracold diatomic and triatomic molecular hydrogen ions was demonstrated in Ref. [11]. For example, production of ultracold H_3^+ was shown to be possible by sympathetic crystallization of $^{40}\mathrm{Ar}^+$ ions and a leak in of neutral H_2 gas into the vacuum chamber, resulting in the two-step chemical reactions $\mathrm{Ar}^+ + \mathrm{H}_2 \rightarrow \mathrm{Ar} + \mathrm{H}_2^+ \Rightarrow \mathrm{H}_2^+ + \mathrm{H}_2 \rightarrow \mathrm{H}_3^+ + \mathrm{H}$ and $\mathrm{Ar}^+ + \mathrm{H}_2 \rightarrow \mathrm{ArH}^+ + \mathrm{H} \Rightarrow \mathrm{ArH}^+ + \mathrm{H}_2 \rightarrow \mathrm{H}_3^+ + \mathrm{Ar}$. Compared to the more direct production of ultracold H_3^+, as described in Ref. [9], this method proved more efficient and showed a reduced formation of unwanted ions such as BeH^+. While laser-cooled fluorescence mass spectrometry (LCF-MS) usually is performed with both the sympathetically and the laser-cooled ions in a cloud-like state, a detailed study of LCF-MS in the crystalline state is presented in Ref. [13]. In particular, by performing LCF-MS on multi-species ion crystals such as $^9\mathrm{Be}^+$-$^4\mathrm{He}^+$ and $^9\mathrm{Be}^+$-H_3^+-H_2^+, large frequency shifts with respect to the calculated single particle frequencies and peak coalescence were observed. In addition, rather complex LCF-MS spectra were obtained in case of a slightly asymmetric trap potential. At this point, the important contribution of molecular dynamics (MD) simulations to Refs. [9–11, 13] shall be pointed out. In particular, by reproducing the observed

crystal structures, reliable information could be obtained regarding the masses and total numbers of crystallized ions, as well as an estimate of the translational temperatures. In addition to this, MD simulations were used to reproduce even complex LCF-MS mass spectra. To this end, a Fourier analysis of the simulated time evolution of a multi-species ion crystal was performed, the MD simulation being started with a small transverse displacement of the ions from their respective equilibrium positions [47]. Finally, laser spectroscopy of ro-vibrational transitions in ultracold HD^+ was demonstrated for the first time and is described in Ref. [12]. In particular, ro-vibrational excitation of a small sample of sympathetically crystallized HD^+ ions was achieved by use of a widely tunable, single-frequency infrared diode laser. The excitation was detected by selective photodissociation using 266 nm laser light. Altogether 12 transitions $(\nu = 0, L) \rightarrow (\nu' = 4, L')$ with orbital momenta $0 \leq L \leq 6$ were observed in the 1391 – 1471 nm wavelength range, partly resolving the hyperfine structure. Typical linewidths of 40 MHz were attributed to the first order Doppler broadening associated with the micromotion of the HD^+ ions.

Appendix A

Electrostatic Potential within a Constant Density Ellipsoid

In order to determine the electrostatic potential ϕ_f within a tri-axial ellipsoid of constant charge density ρ_0, Poisson's equation $\Delta\phi_f = -\rho_0/\epsilon_0$ has to be solved together with additional boundary conditions. In Ref. [74], a solution to this problem of Electrostatics is given analogously to those in Ref. [145]. In the latter reference, the problem of the gravitational potential within a tri-axial ellipsoid of constant mass density is considered. Accordingly (as already noted in Sect. 2.2.2), the electrostatic potential ϕ_f within the ellipsoid may be written as

$$\phi_f \;=\; \frac{\rho_0}{4\epsilon_0}\,\left[A_x(R_x^2 - x^2) + A_y(R_y^2 - y^2) + A_z(L^2 - z^2)\right] \;, \tag{A.1}$$

where R_x, R_y, and L are the principal axes of the ellipsoid in x, y, and z-direction, respectively. The dimensionless coefficients A_x, A_y, and A_z solely depend on the relative lengths of the principal axes R_x, R_y, and L. Eq. (A.1) matches onto an exterior solution which obeys Laplace's equation and vanishes at infinity.

If $R_x < R_y < L$, which is the case relevant to the outer shape of the $^9Be^+$ ion crystals presented in chapter 6, the coefficients A_x, A_y, and A_z are favorably expressed in terms of the the principal axes ratios $\bar{R}_x \stackrel{\text{def}}{=} R_x/L$ and $\bar{R}_y \stackrel{\text{def}}{=} R_y/L$:

$$A_x(\bar{R}_x, \bar{R}_y) \;=\; 2\,\bar{R}_x\bar{R}_y\,\frac{(\bar{R}_y/\bar{R}_x)\sin(\theta) - E(\theta,k^2)}{(1-k^2)\sin^3(\theta)} \tag{A.2a}$$

$$A_y(\bar{R}_x, \bar{R}_y) \;=\; 2\,\bar{R}_x\bar{R}_y\,\frac{E(\theta,k^2) - (1-k^2)F(\theta,k^2) - (\bar{R}_x/\bar{R}_y)k^2\sin(\theta)}{k^2(1-k^2)\sin^3(\theta)} \tag{A.2b}$$

$$A_z(\bar{R}_x, \bar{R}_y) \;=\; 2\,\bar{R}_x\bar{R}_y\,\frac{F(\theta,k^2) - E(\theta,k^2)}{k^2\sin^3(\theta)} \;, \tag{A.2c}$$

where θ and k are given by

$$\theta(\bar{R}_x) \;\stackrel{\text{def}}{=}\; \arccos(\bar{R}_x) \tag{A.3}$$

and

$$k(\bar{R}_x, \bar{R}_y) \;\stackrel{\text{def}}{=}\; \sqrt{(1-\bar{R}_y^2)\,/\,(1-\bar{R}_x^2)} \;. \tag{A.4}$$

In Eqs. (A.2), the symbols F and E denote the elliptic integrals

$$F(\phi, m) \stackrel{\text{def}}{=} \int_0^{\phi} \frac{dx}{\sqrt{1 - m \sin^2(x)}} \tag{A.5a}$$

$$E(\phi, m) \stackrel{\text{def}}{=} \int_0^{\phi} \sqrt{1 - m \sin^2(x)}\ dx\ , \tag{A.5b}$$

where the definitions have been slightly changed with respect to Ref. [74] in order to adapt them to the built-in functions `EllipticF`$[\phi, m]$ and `EllipticE`$[\phi, m]$ of the *Mathematica 5.0* software.

If $R_x < L < R_y$, i.e. in case where the principal axis length R_y increases above the principal axis length L, the coefficients A_x, A_y, and A_z are obtained from Eqs. (A.2), (A.3) and (A.4) as follows. First, the indices y and z have to be mutually exchanged in the A coefficients on the left side of Eqs. (A.2). Then, the principal axes ratios $\bar{R}_x$ and $\bar{R}_y$ have to be replaced by R_x/R_y and L/R_y, respectively, in Eqs. (A.2), (A.3) and (A.4).

Appendix B

Mean Photon Scattering Rate

In this appendix, the mean photon scattering rate $\bar{\Gamma}_{\mathrm{ph}}$ [Eq. (6.1)] will be derived which was used in Sect. 6.2. To this end, definitions and notations shall be chosen equal to those in Ref. [146].

As a starting point, the population rate equations of a two-level atomic system shall be considered, which is excited by the radiation field of a laser:

$$\dot{N}_1 \;=\; A_{21}\,N_2 \;+\; \sigma(\Delta)\,\Phi\cdot(N_2 - N_1) \tag{B.1a}$$

$$\dot{N}_2 \;=\; -A_{21}\,N_2 \;-\; \sigma(\Delta)\,\Phi\cdot(N_2 - N_1) \tag{B.1b}$$

Here, N_1 and N_2 are the numbers of atoms in the ground and excited state, respectively. A_{21} is the spontaneous emission rate, $\sigma(\Delta)$ is the absorption cross section, and Φ is the photon flux (unit: $\mathrm{cm}^{-2}\,\mathrm{s}^{-1}$) of the radiation field. The absorption cross section at a given laser detuning $\Delta \stackrel{\mathrm{def}}{=} \omega_L - \omega_{21}$ is given by

$$\sigma(\Delta) \;=\; \frac{\omega_{21}\,|\mu|^2}{\epsilon_0 \hbar\, c}\cdot\frac{\beta}{\Delta^2+\beta^2}\;, \tag{B.2}$$

where $\mu = e\,\boldsymbol{\epsilon}\,\boldsymbol{r}_{21}$ is the complex dipole moment which is determined from the (complex) polarization vector $\boldsymbol{\epsilon}$ of the radiation field and the matrix element $\boldsymbol{r}_{21}$. More specific, $\boldsymbol{r}_{21} = \langle 2\,|\,\hat{\boldsymbol{r}}\,|1\rangle$ is the matrix element of the position operator $\hat{\boldsymbol{r}}$ between the excited and the ground state of the two-level atomic system [146]. Homogeneous line-broadening is described by the second term on the right side of Eq. (B.2). In particular, $\beta = 1/\tau + A_{21}/2$, where $1/\tau$ is the elastic collision rate and A_{21} is the spontaneous emission rate. Eqs. (B.1a) and (B.1b) have the steady-state solution

$$N_2(\infty) \;=\; \frac{\sigma(\Delta)\,\Phi\,N}{A_{21} + 2\,\sigma(\Delta)\,\Phi}\;, \tag{B.3}$$

obtained in the limit $t\to\infty$, where $N = N_1 + N_2$ is the total number of atoms. Finally, it should be noted that Eq. (B.3) suggests a definition of the saturation flux (at resonance $\Delta = 0$) according to $\Phi_{\mathrm{sat}} \stackrel{\mathrm{def}}{=} A_{21}/2\,\sigma(\Delta = 0)$.

In a gas of atoms with mass m which is in thermal equilibrium at temperature T, equation (B.3) only applies to a given subset of atoms all having the same velocity in the direction of propagation of the radiation field. In particular, for the subset of atoms having velocities in the range between v and $v+dv$,

$$dN_2(\infty) \;=\; \frac{\sigma_v(\Delta)\,\Phi\,N\,df(v)}{A_{21}+2\,\sigma_v(\Delta)\,\Phi}, \quad \text{where} \quad df(v) \;=\; \frac{\sqrt{m}\,\exp[-mv^2/2k_BT]\,dv}{\sqrt{2\pi k_BT}} \tag{B.4}$$

is the (one-dimensional) Maxwell-Boltzmann distribution. In order to account for the Doppler effect, $\sigma(\Delta)$ has been replaced by the velocity-dependent absorption cross section $\sigma_v(\Delta) \stackrel{\text{def}}{=} \sigma(\Delta-(v/c)\omega_{21})$ [Eq. (B.2)]. Integration of Eq. (B.4) yields

$$N_2(\infty) \;=\; \frac{A_{21}N}{8}\cdot\frac{\Phi}{\Phi_{\text{sat}}}\sqrt{\frac{m}{2\pi k_BT}}\int_{-\infty}^{+\infty}\!\!dv\,\frac{\exp[-mv^2/2k_BT]}{[\Delta-(v/c)\,\omega_{21}]^2+(1+\Phi/\Phi_{\text{sat}})\,A_{21}^2/4}, \tag{B.5}$$

where Eq. (B.2) was used together with $\Phi_{\text{sat}} = A_{21}/2\,\sigma(\Delta=0)$ and $\beta = A_{21}/2$, the latter implying negligible collision-broadening ($\tau\to\infty$). Finally, the mean photon scattering rate $\bar{\Gamma}_{\text{ph}}$ as given by Eq. (6.1) is obtained from Eq. (B.5) by setting $\bar{\Gamma}_{\text{ph}} = A_{21}\,N_2(\infty)/N$ and exchanging expressions as follows: $A_{21}\leftrightarrow\gamma$, $\omega_{21}/c\leftrightarrow k_A$, and $\Phi/\Phi_{\text{sat}}\leftrightarrow I/I_{\text{sat}}$.

Appendix C

Alternative RF Trap Setup and Miniature Electron Gun

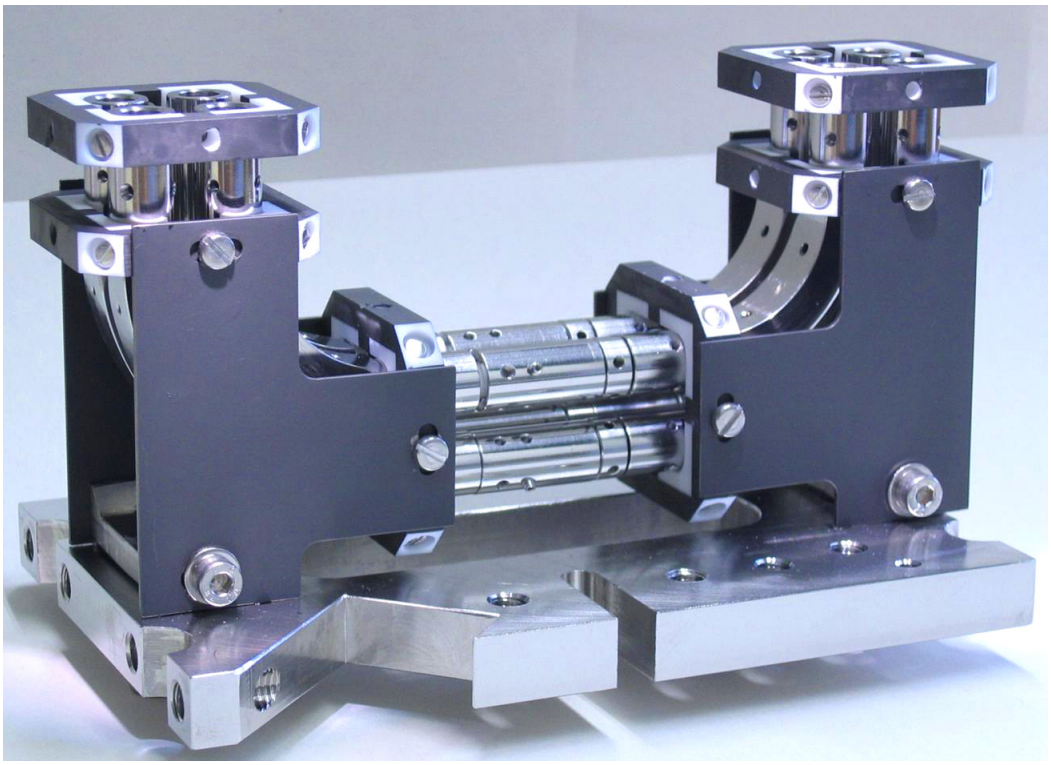

Figure C.1: *Alternative rf trap setup, consisting of a horizontally oriented linear rf trap, two 90°-bent quadrupoles, and two small vertical quadrupoles. Ions produced in one of the two small vertical quadrupoles can be transferred to the linear rf trap through the inbetween 90°-bent quadrupole.*

In addition to the linear rf trap described in Sect. 3.2, an alternative rf trap setup was built with the main goal to separate the loading from the trapping region. In particular, atomic as well as molecular ions shall be produced in the loading region by crossing a stream of neutral gas from a small capillary which is brought close to the loading region with an electron beam. By this, exposure of the laser-cooled $^9Be^+$ ions to the leaked-in neutral gases should be strongly reduced. In a subsequent step, the ions shall be transferred from the loading to the trapping region. Thus, continuous adding of atomic and molecular ions to the laser-cooled $^9Be^+$ ions should be possible with a reduction of unwanted reactions between the neutral gases and the $^9Be^+$ ions, e.g., the formation of BeH^+ and BeD^+ [109]. For the existing vacuum chamber, a spatial separation of the loading from the trapping region also requires a sufficiently small electron gun. In particular, a placement of the electron gun must be possible outside the four DN40CF flanges in the vacuum chamber operating plane (see Sect. 2.3 in Ref. [4]).

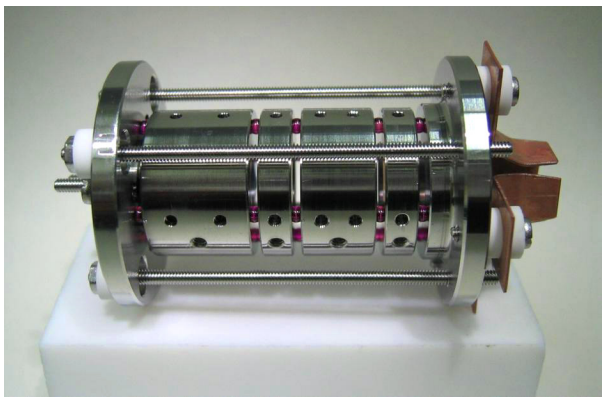

E-Gun Operating Parameters	
Cathode Current	2.75 A
Cathode Voltage	−750 V
Wehnelt Cylinder	−760 V
Einzel Lens	4220 V
	0 V
	4220 V
Final Segment	0 V

Figure C.2: Left: *Miniature Electron gun, consisting of six stacked cylindrical elements made from non-magnetic stainless steel. The overall length is* 48 *mm (without deflection electrodes).* ***Right:*** *Electron gun operating parameters used to generate a* 750 *eV electron beam with a diameter of less than* 1 *mm.*

Fig. C.1 shows the alternative rf trap setup, consisting of a horizontally oriented linear rf trap, two 90°-bent quadrupoles, and two small vertical quadrupoles. The 90°-bent quadrupoles are side-wise attached to the linear rf trap while the small vertical quadrupoles are put at the ends of the 90°-bent quadrupoles. Along the whole (∪-shaped) trap axis, the minimum distance between the trap axis and the electrode surfaces is $r_0 = 4.32\,\text{mm}$. Thus, the transverse dimensions are unchanged with respect to the linear rf trap described in Sect. 3.2. The loading region is provided by one of the two small vertical quadrupoles. Thus, a small capillary and an electron gun shall be brought close to that quadrupole, with the neutral gas stream and the electron beam crossing in the quadrupole center. Transfer of ions to the trapping region, i.e the horizontally oriented linear rf trap, is through the inbetween 90°-bent quadrupole. The second 90°-bent quadrupole may be used to guide ions from the linear rf trap into a channeltron for ion counting. The complete rf trap setup as shown in Fig. C.1, fits well into the existing vacuum chamber and can be driven with the trap supply electronics described in Sect. 3.3.

In order to allow for a placement of the electron gun next to one of the two small vertical quadrupoles, a miniature electron gun was built which is shown in Fig. C.2 (left). The basic design was adopted from Ref. [147]. The electron gun consists of six stacked cylindrical elements made from non-magnetic stainless steel (type 1.3952) and held in compression by four threaded rods. To ensure electrical isolation together with a minimum of mechanical tolerance, 2 mm ruby balls are placed between the cylindrical elements and are located in spherical depressions on each side of the elements. The cathode is a 0.15 mm diameter thoriated tungsten wire, spot-welded to two stainless steel rods used to supply the cathode current. The six cylindrical elements constituting the electron gun are described as follows (from left to right in Fig. C.2): a first element which is held at ground potential merely acts as a cathode mount. This is followed by a Wehnelt cylinder and a three-element Einzel lens, used to focus the electron beam. Finally, the electrons are decelerated and collimated in the last segment with a 5 mm exit aperture. All axial dimensions are optimized with respect to the 10 mm central bore diameter [147]. The resulting

electron gun overall length is 48 mm. Additionally, in order to allow for a position fine-adjustment of the electron beam, four deflection electrodes are grouped around the exit aperture, each cut from a 1 mm copper sheet. With the operating parameters given in Fig. C.2 (right), a 750 eV electron beam with a diameter of less than 1 mm was generated. The diameter was estimated from the electron beam spot size on a phosphor screen, located in a distance of 5 cm from the electron gun. Thus, in addition to its miniature size, the electron gun delivers an electron beam which is strongly focused as compared to those of the flood gun type described in Sect. 3.1. This is favorable since it prevents charging of the trap electrodes. The electron beam current is expected to be in the range between 100 μA and 1 mA [147]. Finally, the beam deflection was measured as 3.7°/100 V, where the voltage was applied symmetrically to a pair of opposing deflection electrodes.

Bibliography

[1] H. Schnitzler, *Development of an Experiment for Trapping, Cooling, and Spectroscopy of Molecular Hydrogen Ions*, Dissertation, Universität Konstanz (2001).

[2] T. K. W. Boley, *Konzeption und Aufbau eines Experiments zur Speicherung, Kühlung und Spektroskopie von Wasserstoffmolekülionen*, Diplomarbeit, Universität Konstanz (1999).

[3] A. Schmidt, *Aufbau eines Experiments zur sympathetischen Kühlung von Molekülionen in einer Paulfalle*, Diplomarbeit, Universität Konstanz (2000).

[4] H. Schnitzler, U. Fröhlich, T. K. W. Boley, A. E. M. Clemen, J. Mlynek, A. Peters, and S. Schiller, *All-Solid-State Tunable Continuous Wave Ultraviolet Laser Source with High Spectral Purity and Frequency Stability*, Appl. Optics **41**, 7000–7005 (2002).

[5] U. Fröhlich, *Ultra-Cold Molecules in Coulomb Crystals*, Workshop and Training School on Theoretical Concepts and Recent Experiments on Ultracold Molecules, Volterra, Italy (2003).

[6] U. Fröhlich, B. Roth, P. Antonini, C. Lämmerzahl, A. Wicht, and S. Schiller, *Ultracold Trapped Molecules: Novel Systems for Tests of the Time-Independence of the Electron-to-Proton Mass Ratio*, in: *Astrophysics, Clocks and Fundamental Constants*, S. G. Karshenboim and E. Peik (Ed.), Lecture Notes in Physics **648**, Springer, Berlin (2004).

[7] U. Fröhlich, B. Roth, and S. Schiller, *Ellipsoidal Coulomb Crystals in a Linear Radio-Frequency Trap*, Phys. Plasmas **12**, 073506 (2005).

[8] B. Roth, U. Fröhlich, and S. Schiller, *Sympathetic Cooling of $^4He^+$ Ions in a Radio-Frequency Trap*, Phys. Rev. Lett. **94**, 053001 (2005).

[9] P. Blythe, B. Roth, U. Fröhlich, H. Wenz, and S. Schiller, *Production of Ultracold Trapped Molecular Hydrogen Ions*, Phys. Rev. Lett. **95**, 183002 (2005).

[10] B. Roth, P. Blythe, H. Wenz, H. Daerr, and S. Schiller, *Ion-Neutral Chemical Reactions between Ultracold Localized Ions and Neutral Molecules with Single-Particle Resolution*, Phys. Rev. A **73**, 042712 (2006).

[11] B. Roth, P. Blythe, H. Daerr, L. Patacchini, and S. Schiller, *Production of Ultracold Diatomic and Triatomic Molecular Ions of Spectroscopic and Astrophysical Interest*, J. Phys. B: At. Mol. Opt. Phys. **39**, S1241–S1258 (2006).

[12] B. Roth, J. C. J. Koelemeij, H. Daerr, and S. Schiller, *Rovibrational Spectroscopy of Trapped Molecular Hydrogen Ions at Millikelvin Temperatures*, Phys. Rev. A **74**, 040501 (2006).

[13] B. Roth, P. Blythe, and S. Schiller, *Motional Resonance Coupling in Cold Multispecies Coulomb Crystals*, Phys. Rev. A **75**, 023402 (2007).

[14] B. Roth, J. Koelemeij, S. Schiller, L. Hilico, J. Karr, V. Korobov, and D. Bakalov, *Precision Spectroscopy of Molecular Hydrogen Ions: Towards Frequency Metrology of Particle Masses*, in: *Precision Physics of Simple Atoms and Molecules*, S. G. Karshenboim (Ed.), Lecture Notes in Physics **745**, Springer, Berlin (2008).

[15] J. C. J. Koelemeij, B. Roth, A. Wicht, I. Ernsting, and S. Schiller, *Vibrational Spectroscopy of HD^+ with 2-ppb Accuracy*, Phys. Rev. Lett. **98**, 173002 (2007).

[16] S. Schiller and V. Korobov, *Test of Time Independence of the Electron and Nuclear Masses with Ultracold Molecules*, Phys. Rev. A **71**, 032505 (2005).

[17] P. J. Mohr and B. N. Taylor, *CODATA Recommended Values of the Fundamental Physical Constants: 2002*, Rev. Mod. Phys. **77**, 1–107 (2005), see also: http://www.physics.nist.gov/constants.

[18] J. Verdú, S. Djekić, S. Stahl, T. Valenzuela, M. Vogel, and G. Werth, *Electronic g Factor of Hydrogenlike Oxygen $^{16}O^{7+}$*, Phys. Rev. Lett. **92**, 093002 (2004).

[19] J. P. Karr, S. Kilic, and L. Hilico, *Energy Levels and Two-Photon Transition Probabilities in the HD^+ Ion*, J. Phys. B: At. Mol. Opt. Phys. **38**, 853–866 (2005).

[20] V. I. Korobov, *Leading Order Relativistic and Radiative Corrections to the Rovibrational Spectrum of H_2^+ and HD^+ Molecular Ions*, Phys. Rev. A **74**, 052506 (2006).

[21] V. I. Korobov, *Bethe Logarithm for the Hydrogen Molecular Ion HD^+*, Phys. Rev. A **70**, 012505 (2004).

[22] D. Bakalov, V. I. Korobov, and S. Schiller, *High-Precision Calculation of the Hyperfine Structure of the HD^+ Ion*, Phys. Rev. Lett. **97**, 243001 (2006).

[23] W. H. Wing, G. A. Ruff, W. E. Lamb, and J. J. Spezeski, *Observation of the Infrared Spectrum of the Hydrogen Molecular Ion HD^+*, Phys. Rev. Lett. **36**, 1488–1491 (1976).

[24] A. Carrington, I. R. McNab, and C. A. Montgomerie, *Spectroscopy of the Hydrogen Molecular Ion*, J. Phys. B: At. Mol. Opt. Phys. **22**, 3551–3586 (1989).

[25] R. E. Drullinger, D. J. Wineland, and J. C. Bergquist, *High-Resolution Optical Spectra of Laser Cooled Ions*, Appl. Phys. A **22**, 365–368 (1980).

[26] M. D. Barrett, B. DeMarco, T. Schaetz, D. Leibfried, J. Britton, J. Chiaverini, W. M. Itano, B. Jelenkovic, J. D. Jost, C. Langer, T. Rosenband, and D. J. Wineland, *Sympathetic Cooling of* $^{9}Be^{+}$ *and* $^{24}Mg^{+}$ *for Quantum Logic*, Phys. Rev. A **68**, 042302 (2003).

[27] A. Ostendorf, C. B. Zhang, M. A. Wilson, D. Offenberg, B. Roth, and S. Schiller, *Sympathetic Cooling of Complex Molecular Ions to Millikelvin Temperatures*, Phys. Rev. Lett. **97**, 243005 (2006).

[28] V. L. Ryjkov, X.-Z. Zhao, and H. A. Schuessler, *Sympathetic Cooling of Fullerene Ions by Laser-Cooled* Mg^{+} *Ions in a Linear RF Trap*, Phys. Rev. A **74**, 023401 (2006).

[29] T. Baba and I. Waki, *Sympathetic Cooling Rate of Gas-Phase Ions in a Radio-Frequency-Quadrupole Ion Trap*, Appl. Phys. B **74**, 375–382 (2002).

[30] H. M. van Horn, *Cooling of White Dwarfs*, in: *White Dwarfs, Proceedings of IAU Symposium 42*, W. J. Luyten (Ed.), International Astronomical Union Symposia, Springer-Verlag, Dordrecht (1971).

[31] R. W. Hasse and J. P. Schiffer, *The Structure of the Cylindrically Confined Coulomb Lattice*, Ann. Phys. **203**, 419–448 (1990).

[32] F. Diedrich, E. Peik, J. M. Chen, W. Quint, and H. Walther, *Observation of a Phase Transition of Stored Laser-Cooled Ions*, Phys. Rev. Lett. **59**, 2931–2934 (1987).

[33] D. J. Wineland, J. C. Bergquist, W. M. Itano, J. J. Bollinger, and C. H. Manney, *Atomic-Ion Coulomb Clusters in an Ion Trap*, Phys. Rev. Lett. **59**, 2935–2938 (1987).

[34] G. Birkl, S. Kassner, and H. Walther, *Multi-Shell Structures of Laser-Cooled* $^{24}Mg^{+}$ *Ions in a Quadrupole Storage Ring*, Nature **357**, 310–313 (1992).

[35] I. Waki, S. Kassner, G. Birkl, and H. Walther, *Observation of Ordered Structures of Laser-Cooled Ions in a Quadrupole Storage Ring*, Phys. Rev. Lett. **68**, 2007–2010 (1992).

[36] W. M. Itano, J. J. Bollinger, J. N. Tan, B. Jelenkovic, X.-P. Huang, and D. J. Wineland, *Bragg Diffraction from Crystallized Ion Plasmas*, Science **279**, 686–689 (1998).

[37] T. B. Mitchell, J. J. Bollinger, D. H. E. Dubin, X.-P. Huang, W. M. Itano, and R. H. Baughman, *Direct Observations of Structural Phase Transitions in Planar Crystallized Ion Plasmas*, Science **282**, 1290–1293 (1998).

[38] D. J. Berkeland, J. D. Miller, J. C. Bergquist, W. M. Itano, and D. J. Wineland, *Laser-Cooled Mercury Ion Frequency Standard*, Phys. Rev. Lett. **80**, 2089–2092 (1998).

[39] M. D. Lukin, S. F. Yelin, and M. Fleischhauer, *Entanglement of Atomic Ensembles by Trapping Correlated Photon States*, Phys. Rev. Lett. **84**, 4232–4235 (2000).

[40] J. I. Cirac and P. Zoller, *Quantum Computations with Cold Trapped Ions*, Phys. Rev. Lett. **74**, 4091–4094 (1995).

[41] A. Sørensen and K. Mølmer, *Quantum Computation with Ions in Thermal Motion*, Phys. Rev. Lett. **82**, 1971–1974 (1999).

[42] L. Hornekær and M. Drewsen, *Formation Process of Large Ion Coulomb Crystals in Linear Paul Traps*, Phys. Rev. A **66**, 013412 (2002).

[43] K. Mølhave and M. Drewsen, *Formation of Translationally Cold MgH^+ and MgD^+ Molecules in an Ion Trap*, Phys. Rev. A **62**, 011401 (2000).

[44] M. A. van Eijkelenborg, M. E. M. Storkey, D. M. Segal, and R. C. Thompson, *Sympathetic Cooling and Detection of Molecular Ions in a Penning Trap*, Phys. Rev. A. **60**, 3903–3910 (1999).

[45] L. Hornekær, *Single- and Multi-Species Coulomb Ion Crystals: Structure, Dynamics and Sympathetic Cooling*, PhD Thesis, University of Aarhus, Denmark (2000).

[46] P. Bowe, L. Hornekær, C. Brodersen, M. Drewsen, J. S. Hangst, and J. P. Schiffer, *Sympathetic Crystallization of Trapped Ions*, Phys. Rev. Lett. **82**, 2071–2074 (1999).

[47] B. Roth, A. Ostendorf, H. Wenz, and S. Schiller, *Production of Large Molecular Ion Crystals via Sympathetic Cooling by Laser-Cooled Ba^+*, J. Phys. B: At. Mol. Opt. Phys. **38**, 3673–3685 (2005).

[48] S. Schiller and C. Lämmerzahl, *Molecular Dynamics Simulation of Sympathetic Crystallization of Molecular Ions*, Phys. Rev. A **68**, 053406 (2003).

[49] D. Kielpinski, B. E. King, C. J. Myatt, C. A. Sackett, Q. A. Turchette, W. M. Itano, C. Monroe, and D. J. Wineland, *Sympathetic Cooling of Trapped Ions for Quantum Logic*, Phys. Rev. A **61**, 032310 (2000).

[50] T. Baba and I. Waki, *Cooling and Mass-Analysis of Molecules Using Laser-Cooled Atoms*, Jpn. J. Appl. Phys. **35**, Part 2, L1134–L1137 (1996).

[51] M. A. Armitage, J. E. Fulford, D. N. Hoa, R. J. Hughes, and R. E. March, *The Application of Resonant Ion Ejection to Quadrupole Ion Storage Mass Spectrometry: A Study of Ion/Molecule Reactions in the QUISTOR*, Can. J. Chem. **57**, 2108–2113 (1979).

[52] R. W. W. Alheit, *Speicherung und laserinduzierte Photodissoziation von H_2^+ in einer Paulfalle*, Dissertation, Johannes-Gutenberg-Universität Mainz (1997).

[53] J. C. Schwartz, M. W. Senko, and J. E. P. Syka, *A Two-Dimensional Quadrupole Ion Trap Mass Spectrometer*, J. Am. Soc. Mass Spectrom. **13**, 659–669 (2002).

[54] T. Baba and I. Waki, *Spectral Shape of In Situ Mass Spectra of Sympathetically Cooled Molecular Ions*, J. Appl. Phys. **92**, 4109–4116 (2002).

[55] D. R. Denison, *Operating Parameters of a Quadrupole in a Grounded Cylindrical Housing*, J. Vac. Sci. Technol. **8**, 266–269 (1971).

[56] W. Paul, *Elektromagnetische Käfige für geladene und neutrale Teilchen*, Phys. Bl. **46**, 227–237 (1990).

[57] Note: Mathieu functions are available as built-in functions `MathieuC`$[a, q, z]$ and `MathieuS`$[a, q, z]$ in the Mathematica 5.0 software.

[58] H. G. Dehmelt, *Radiofrequency Spectroscopy of Stored Ions, Part I: Storage*, Adv. At. Mol. Phys. **3**, 53–72 (1967).

[59] T. M. O'Neil and D. H. E. Dubin, *Thermal Equilibria and Thermodynamics of Trapped Plasmas with a Single Sign of Charge*, Phys. Plasmas **5**, 2163–2193 (1998).

[60] D. H. E. Dubin and T. M. O'Neil, *Trapped Nonneutral Plasmas, Liquids, and Crystals (The Thermal Equilibrium States)*, Rev. Mod. Phys. **71**, 87–172 (1999).

[61] R. C. Davidson, *Physics of Nonneutral Plasmas*, Imperial College Press, London (2001).

[62] A. Sitenko and V. Malnev, *Plasma Physics Theory*, Chapman & Hall / CRC, London (1995).

[63] S. G. Brush, H. L. Sahlin, and E. Teller, *Monte Carlo Study of a One-Component Plasma. I*, J. Chem. Phys. **45**, 2102–2118 (1966).

[64] J. P. Hansen, *Statistical Mechanics of Dense Ionized Matter. I. Equilibrium Properties of the Classical One-Component Plasma*, Phys. Rev. A **8**, 3096–3109 (1973).

[65] E. L. Pollock and J. P. Hansen, *Statistical Mechanics of Dense Ionized Matter. II. Equilibrium Properties and Melting Transitions of the Crystallized One-Component Plasma*, Phys. Rev. A **8**, 3110–3122 (1973).

[66] W.L. Slattery, G.D. Doolen, and H.E. DeWitt, *Improved Equation of State for the Classical One-Component Plasma*, Phys. Rev. A **21**, 2087–2095 (1980).

[67] S. Ichimaru, *Strongly Coupled Plasmas: High Density Classical Plasmas and Degenerate Electron Liquids*, Rev. Mod. Phys. **54**, 1017–1059 (1982).

[68] J. N. Tan, J. J. Bollinger, B. Jelenkovic, and D. J. Wineland, *Long-Range Order in Laser-Cooled, Atomic-Ion Wigner Crystals Observed by Bragg Scattering*, Phys. Rev. Lett. **75**, 4198–4201 (1995).

[69] M. Drewsen, C. Brodersen, L. Hornekær, J. S. Hangst, and J. P. Schiffer, *Large Ion Crystals in a Linear Paul Trap*, Phys. Rev. Lett. **81**, 2878–2881 (1998).

[70] L. Turner, *Collective Effects on Equilibria of Trapped Charged Plasmas*, Phys. Fluids **30**, 3196–3203 (1987).

[71] S. A. Prasad and T. M. O'Neil, *Finite Length Thermal Equilibria of a Pure Electron Plasma Column*, Phys. Fluids **22**, 278–281 (1979).

[72] C. F. Driscoll, J. H. Malmberg, and K. S. Fine, *Observation of Transport to Thermal Equilibrium in Pure Electron Plasmas*, Phys. Rev. Lett. **60**, 1290–1293 (1988).

[73] X. P. Huang, F. Anderegg, E. M. Hollmann, C. F. Driscoll, and T. M. O'Neil, *Steady-State Confinement of Non-Neutral Plasmas by Rotating Electric Fields*, Phys. Rev. Lett. **78**, 875–878 (1997).

[74] D. H. E. Dubin, *Equilibrium and Dynamics of Uniform Density Ellipsoidal Non-Neutral Plasmas*, Phys. Fluids B **5**, 295–324 (1993).

[75] L. Hornekær, N. Kjærgaard, A. M. Thommesen, and M. Drewsen, *Structural Properties of Two-Component Coulomb Crystals in Linear Paul Traps*, Phys. Rev. Lett. **86**, 1994–1997 (2001).

[76] T. Baba and I. Waki, *Laser-Cooled Fluorescence Mass Spectrometry Using Laser-Cooled Barium Ions in a Tandem Linear Ion Trap*, J. Appl. Phys. **89**, 4592–4598 (2001).

[77] T. Baba and I. Waki, *Chemical Reaction of Sympathetically Laser-Cooled Molecular Ions*, J. Chem. Phys. **116**, 1858–1861 (2002).

[78] R. Blümel, C. Kappler, W. Quint, and H. Walther, *Chaos and Order of Laser-Cooled Ions in a Paul Trap*, Phys. Rev. A **40**, 808–823 (1989).

[79] J. D. Prestage, A. Williams, L. Maleki, M. J. Djomehri, and E. Harabetian, *Dynamics of Charged Particles in a Paul Radio-Frequency Quadrupole Trap*, Phys. Rev. Lett. **66**, 2964–2967 (1991).

[80] D. J. Wineland and W. M. Itano, *Laser Cooling of Atoms*, Phys. Rev. A **20**, 1521–1540 (1979).

[81] Y. Moriwaki, M. Tachikawa, Y. Maeno, and T. Shimizu, *Collision Cooling of Ions Stored in Quadrupole Radio-Frequency Trap*, Jpn. J. Appl. Phys. **31**, Part 2, L1640–L1643 (1992).

[82] R. G. Brewer, J. Hoffnagle, R. G. Devoe, L. Reyna, and W. Henshaw, *Collision Induced Two-Ion Chaos*, Nature **344**, 305–309 (1990).

[83] Extorr Inc., *Application Note Number 3: What are Typical Stainless Steel Vacuum System Mass Spectra like?*, available: http://www.extorr.com (December 2007).

[84] Ashcroft and Mermin, *Solid State Physics*, Saunders College Publishing, Philadelphia (1976).

[85] S. Robertson and Z. Sternovsky, *Reduction of Asymmetry Transport in the Annular Penning Trap*, Phys. Plasmas **11**, 1753–1756 (2004).

[86] CWS ByteMark, *Magnetic Properties of Ferrite Materials*, available: http://www.cwsbytemark.com (December 2007).

[87] Hamamatsu, *R1527P Specifications*, available: http://sales.hamamatsu.com (December 2007).

[88] C. Monroe, D. M. Meekhof, B. E. King, S. R. Jefferts, W. M. Itano, D. J. Wineland, and P. Gould, *Resolved-Sideband Raman Cooling of a Bound Atom to the 3D Zero-Point Energy*, Phys. Rev. Lett. **75**, 4011–4014 (1995).

[89] C. E. Wagstaff and M. H. Dunn, *A Second-Harmonic, Ring Dye Laser for the Generation of Continuous-Wave, Single-Frequency UV Radiation*, J. Phys. D **12**, 355–368 (1979).

[90] J. J. Bollinger, J. S. Wells, D. J. Wineland, and W. M. Itano, *Hyperfine Structure of the* $2p\ ^2P_{1/2}$ *State in* $^9Be^+$, Phys. Rev. A **31**, 2711–2714 (1985).

[91] H. Imajo, K. Hayasaka, R. Ohmukai, M. Watanabe, and S. Urabe, *Observation of Laser Cooled* Be^+*-Ion Clouds in a Penning Trap*, Appl. Phys. B **61**, 285–289 (1995).

[92] Y. Kaneda and S. Kubota, *Theoretical Treatment, Simulations, and Experiments of Doubly Resonant Sum-Frequency Mixing in an External Resonator*, Appl. Opt. **36**, 7766–7775 (1997).

[93] G. D. Boyd and D. A. Kleinman, *Parametric Interaction of Focused Gaussian Light Beams*, J. Appl. Phys. **39**, 3597–3639 (1968).

[94] K. Schneider, S. Schiller, J. Mlynek, M. Bode, and I. Freitag, *1.1-W Single-Frequency 532-nm Radiation from a Miniature Nd:YAG Ring Laser*, Opt. Lett. **21**, 1999–2001 (1996).

[95] M. Bode, I. Freitag, A. Tünnermann, and H. Welling, *Frequency-Tunable 500-mW Continuous-Wave All-Solid-State Single-Frequency Source in the Blue Spectral Region*, Opt. Lett. **22**, 1220–1222 (1997).

[96] R. W. P. Drever, J. L. Hall, F. V. Kowalski, J. Hough, G. M. Ford, A. J. Munley, and H. Ward, *Laser Phase and Frequency Stabilization using an Optical Resonator*, Appl. Phys. B **31**, 97–105 (1983).

[97] R. Wynands and A. Nagel, *Precision Spectroscopy with Coherent Dark States*, Appl. Phys. B: Lasers Opt. **68**, 1–25 (1999).

[98] A. Arie and R. L. Byer, *Laser Heterodyne Spectroscopy of* $^{127}I_2$ *Hyperfine Structure near 532 nm*, J. Opt. Soc. Am. B **10**, 1990–1997 (1993).

[99] C. Braxmaier, *Frequenzstabilisierung eines Nd:YAG-Lasers auf Hyperfeinübergänge von molekularen Jod*, Diplomarbeit, Universität Konstanz (1997).

[100] W. Demtröder, *Laser Spectroscopy - 3rd Edition*, Springer, Berlin (2003).

[101] J. E. Thomas, P. R. Hemmer, S. Ezekiel, C. C. Leiby Jr., R. H. Picard, and C. R. Willis, *Observation of Ramsey Fringes Using a Stimulated, Resonance Raman Transition in a Sodium Atomic Beam*, Phys. Rev. Lett. **48**, 867–870 (1982).

[102] F. B. J. Buchkremer, R. Dumke, Ch. Buggle, G. Birkl, and W. Ertmer, *Low-Cost Setup for Generation of 3 GHz Frequency Difference Phase-Locked Laser Light*, Rev. Sci. Instrum. **71**, 3306–3308 (2000).

[103] D. J. Wineland, J. J. Bollinger, and W. M. Itano, *Laser-Fluorescence Mass Spectroscopy*, Phys. Rev. Lett. **50**, 628–631 (1983).

[104] K. Okada, M. Wada, L. Boesten, T. Nakamura, I. Katayama, and S. Ohtani, *Acceleration of the Chemical Reaction of Trapped Ca^+ Ions with H_2O Molecules by Laser Excitation*, J. Phys. B: At. Mol. Opt. Phys. **36**, 33–46 (2003).

[105] T. Nakamura, S. Ohtani, M. Wada, K. Okada, I. Katayama, and H. A. Schuessler, *Ion Dynamics and Oscillation Frequencies in a Linear Combined Trap*, J. Appl. Phys. **89**, 2922–2931 (2001).

[106] M. Welling, H. A. Schuessler, R. I. Thompson, and H. Walther, *Ion/Molecule Reactions, Mass Spectrometry and Optical Spectroscopy in a Linear Ion Trap*, Int. J. Mass Spectrom. Ion Processes **172**, 95–114 (1998).

[107] Y. Hashimoto, H. Hasegawa, T. Baba, and I. Waki, *Mass Selective Ejection by Axial Resonant Excitation from a Linear Ion Trap*, J. Am. Soc. Mass Spectrom. **17**, 685–690 (2006).

[108] A. Drakoudis, M. Söllner and G. Werth, *Instabilities of Ion Motion in a Linear Paul Trap*, Int. J. Mass. Spectrom. **252**, 61–68 (2006).

[109] Note: In this work, formation of BeH^+ and BeD^+ molecular ions by the chemical reactions $Be^+ + H_2 \rightarrow BeH^+ + H$, $Be^+ + HD \rightarrow BeH^+ + D$, and $Be^+ + HD \rightarrow BeD^+ + H$ was detected using LCF-MS. To this end, neutral H_2 as well as HD gas was introduced into the vacuum chamber while laser-cooled Be^+ ions were confined in the trap. See also Ref. [10].

[110] T. Hasegawa and T. Shimizu, *Resonant Oscillation Modes of Sympathetically Cooled Ions in a Radio-Frequency Trap*, Phys. Rev. A **66**, 063404 (2002).

[111] A. J. Peurrung, R. T. Kouzes, and S. E. Barlow, *The Non-Neutral Plasma: An Introduction to Physics with Relevance to Cyclotron Resonance Mass Spectrometry*, Int. J. Mass Spectrom. Ion Processes **157/158**, 39–83 (1996).

[112] L. K. Randeniya and M. A. Smith, *Gase Phase Reaction Rates of N_2^+ with CH_4, O_2, and n-H_2 at Very Low Temperatures*, J. Chem. Phys. **94**, 351–356 (1991).

[113] M. G. Raizen, J. M. Gilligan, J. C. Bergquist, W. M. Itano, and D. J. Wineland, *Linear Trap for High-Accuracy Spectroscopy of Stored Ions*, J. Mod. Opt. **39**, 233–242 (1992).

[114] D. H. E. Dubin, *Effect of Correlations on the Thermal Equilibrium and Normal Modes of a Non-Neutral Plasma*, Phys. Rev. E **53**, 5268–5290 (1996).

[115] K. Huang, *Statistical Mechanics, Chapter 4: The Equilibrium State of a Dilute Gas - 2nd Edition*, John Wiley & Sons, New York (1987).

[116] R. D. Knight and M. H. Prior, *Laser Scanning Measurement of the Density Distribution of Confined $^6Li^+$ Ions*, J. Appl. Phys. **50**, 3044–3049 (1979).

[117] H. Schaaf, U. Schmeling, and G. Werth, *Trapped Ion Density Distribution in the Presence of He-Buffer Gas*, Appl. Phys. **25**, 249–251 (1981).

[118] D. H. E. Dubin and T. M. O'Neil, *Computer Simulation of Ion Clouds in a Penning Trap*, Phys. Rev. Lett. **60**, 511–514 (1988).

[119] A. Rahman and J. P. Schiffer, *Structure of a One-Component Plasma in an External Field: A Molecular-Dynamics Study of Particle Arrangement in a Heavy-Ion Storage Ring*, Phys. Rev. Lett. **57**, 1133–1136 (1986).

[120] J. P. Schiffer, *Order in Cold Ionic Systems: Dynamic Effects*, in: *Proceedings of the Workshop on Crystalline Ion Beams*, R. W. Hasse, I. Hofmann, and D. Liesen (Ed.), GSI-89-10 Report (1989).

[121] R. W. Hasse and V. V. Avilov, *Structure and Madelung Energy of Spherical Coulomb Crystals*, Phys. Rev. A **44**, 4506–4515 (1991).

[122] K. Tsuruta and S. Ichimaru, *Binding Energy, Microstructure, and Shell Model of Coulomb Clusters*, Phys. Rev. A **48**, 1339–1344 (1993).

[123] I. Siemers, R. Blatt, T. Sauter, and W. Neuhauser, *Dynamics of Ion Clouds in Paul Traps*, Phys. Rev. A **38**, 5121–5128 (1988).

[124] Y. Maeno, M. Tachikawa, Y. Moriwaki, and T. Shimizu, *Dynamics of Trapped Ions in the Presence of Laser Cooling and Radio-Frequency Heating*, Jpn. J. Appl. Phys. **34**, Part 2, L174–L176 (1995).

[125] L. R. Brewer, J. D. Prestage, J. J. Bollinger, W. M. Itano, D. J. Larson, and D. J. Wineland, *Static Properties of a Non-Neutral $^9Be^+$ -Ion Plasma*, Phys. Rev. A **38**, 859–873 (1988).

[126] X. P. Huang, J. J. Bollinger, T. B. Mitchell, W. M. Itano, *Precise Control of the Global Rotation of Strongly Coupled Ion Plasmas in a Penning Trap*, Phys. Plasmas **5**, 1656–1663 (1998).

[127] H. Wenz, private communication.

[128] S. G. Karshenboim and V. B. Smirnov (Ed.), *Precision Physics of Simple Atomic Systems*, Lecture Notes in Physics **627**, Springer, Berlin (2003).

[129] M. I. Eides, H. Grotch, and V. A. Shelyuto, *Theory of Light Hydrogenlike Atoms*, Phys. Rep. **342**, 63–261 (2001).

[130] J. D. Gillaspy, *Highly Charged Ions*, J. Phys. B: At. Mol. Opt. Phys. **34**, R93–R130 (2001).

[131] V. M. Shabaev, A. N. Artemyev, V. A. Yerokhin, O. M. Zherebtsov, and G. Soff, *Towards a Test of QED in Investigations of the Hyperfine Splitting in Heavy Ions*, Phys. Rev. Lett. **86**, 3959–3962 (2001).

[132] B. de Beauvoir, C. Schwob, O. Acef, L. Jozefowski, L. Hilico, F. Nez, L. Julien, A. Clairon, and F. Biraben, *Metrology of the Hydrogen and Deuterium Atoms: Determination of the Rydberg Constant and Lamb Shifts*, Eur. Phys. J. D **12**, 61–93 (2000).

[133] H. A. Schuessler, E. N. Fortson, and H. G. Dehmelt, *Hyperfine Structure of the Ground State of $^3He^+$ by the Ion-Storage Exchange-Collision Technique*, Phys. Rev. **187**, 5–38 (1969).

[134] M. H. Prior and E. C. Wang, *Hyperfine structure of the $2s$ state of $^3He^+$*, Phys. Rev. A **16**, 6–18 (1977).

[135] S. G. Karshenboim and V. G. Ivanov, *Hyperfine Structure of the Ground and First Excited States in Light Hydrogen-Like Atoms and High-Precision Tests of QED*, Eur. Phys. J. D **19**, 13–23 (2002).

[136] A. van Wijngaarden, F. Holuj, and G. W. F. Drake, *Lamb Shift in He^+: Resolution of a Discrepancy between Theory and Experiment*, Phys. Rev. A **63**, 012505 (2000).

[137] U. D. Jentschura and G. W. F. Drake, *The $2S_{1/2} - 2P_{1/2}$ Lamb Shift in He^+*, Can. J. Phys. **82**, 103–108 (2004).

[138] D. Shiner, R. Dixson, and V. Vedantham, *Three-Nucleon Charge Radius: A Precise Laser Determination Using ^3He*, Phys. Rev. Lett. **74**, 3553–3556 (1995).

[139] J. L. Flowers, H. A. Klein, D. J. E. Knight, and H. S. Margolis, *Hydrogenic Systems for Calculable Frequency Standards: Status and Options*, NPL Report CBTLM 11 (2001).

[140] S. A. Burrows et al. in: *Laser Spectroscopy: Proceedings of the 14th International Conference, Innsbruck, Austria*, R. Blatt ,J. Eschner, D. Leibfried, and F. Schmidt-Kaler (Ed.), World Scientific Publishing (1999).

[141] Note: QED uncertainty without nuclear radius effect $\approx 6 \cdot 10^4$ Hz, nuclear radius effect uncertainty $\approx 7 \cdot 10^4$ Hz [128,137], and uncertainty due to Rydberg constant $\approx 8 \cdot 10^4$ Hz. For the $2S$-$3S$ transition, the situation is somewhat less favorable due to a large relative contribution of the R_∞ (Rydberg constant) uncertainty and the large transition linewidth.

[142] P. Gill (Ed.), *Frequency Standards and Metrology: Proceedings of the 6th Symposium, St. Andrews, Fife, Scotland*, World Scientific Publishing (2002).

[143] D. J. Wineland, J. C. Bergquist, J. J. Bollinger, R. E. Drullinger, and W. M. Itano, *Quantum Computers and Atomic Clocks*, in: *Frequency Standards and Metrology: Proceedings of the 6th Symposium, St. Andrews, Fife, Scotland*, P. Gill (Ed.), World Scientific Publishing (2002).

[144] B. B. Blinov, L. Deslauriers, P. Lee, M. J. Madsen, R. Miller, and C. Monroe, *Sympathetic Cooling of Trapped Cd^+ Isotopes*, Phys. Rev. A **65**, 040304 (2002).

[145] J. Binney and S. Tremaine, *Galactic Dynamics, Chapter 3: The Orbits of Stars*, Princeton University Press, New Jersey (1987).

[146] P. W. Milonni and J. H. Eberly, *Lasers*, John Wiley & Sons, New York (1988).

[147] P. W. Erdman and E. C. Zipf, *Low-Voltage, High-Current Electron Gun*, Rev. Sci. Instrum. **53**, 225–227 (1982).

Acknowledgment

An dieser Stelle möchte ich zunächst **Prof. Stephan Schiller** dafür danken, dieses spannende Projekt nach dem Umzug von Konstanz nach Düsseldorf, d.h. in der zweiten Phase des experimentellen Aufbaus, "übernehmen" zu dürfen. Besonders hervorheben möchte ich dabei die Kombination von konkreten, langfristigen Zielvorgaben einerseits und großen Freiheiten bei der Realisierung des experimentellen Aufbaus andererseits. Weiterhin möchte ich all denen danken, die zum Gelingen dieser Arbeit beigetragen haben: **Harald Schnitzler** für die Einführung in das Projekt. **Bernhard Roth** für seine Hilfe bei der Durchführung vieler Messungen, oft auch zu nächtlicher Stunde. **Peter Dutkiewicz** für das Design und den Aufbau diverser elektronischer Komponenten (und für viele schöne Geschichten in den Kaffeepausen). **Jens Bremer** und **Heinrich Hoffmann** für das Anfertigen mechanischer Komponenten, und **Wilhelm Röckrath** für seine Hilfe rund um den Computer. Meinen Mitdoktoranden **Luca Haiberger**, **Piergiorgio Antonini** und **Alexander Ostendorf** und meiner Bürogenossin **Rita Gusek** möchte ich für das gute Arbeitsklima am Institut danken.

Vielen Dank auch an Dich, liebe **Anne**, für die vielen geopferten Wochenenden in der letzten, dann doch noch fast drei Jahre dauernden Phase des Anfertigens dieser Dissertation.

Die hier vorgelegte Dissertation habe ich eigenhändig und ohne unerlaubte Hilfe angefertigt. Die Dissertation wurde in der vorgelegten oder in ähnlicher Form noch bei keiner anderen Institution eingereicht. Ich habe bisher keine erfolglosen Promotionsversuche unternommen.

Bremen, den 11. 04. 2008

. . . . . .
(Ulf Fröhlich)